

JULIUS-MAXIMILIANS-UNIVERSITÄT WÜRZBURG

MASTER'S THESIS

Parsec-scale Radio Jets of γ -ray-faint Quasars

Author:
Rosamunde Pare

Supervisor:
Prof. Dr. Matthias Kadler



*A thesis submitted in fulfilment of the requirements
for the degree of Master of Science*

in the group of

Prof. Dr. Matthias Kadler
Lehrstuhl für Astronomie

Zusammenfassung

Radiolaute aktive Galaxienkerne (AGN) emittieren sogenannte Jets, kollimierte Plasmaströme, die sich durch *Very Long Baseline Interferometry* (VLBI) bei sehr hoher Auflösung untersuchen lassen. Das Standardmodell beschreibt die aktive galaktische Kernregion mit einem supermassiven schwarzen Loch (SMBH) im Zentrum. Das SMBH, eine umgebende Akkretionsscheibe, ein kalter Staubtorus und Gaswolken mit unterschiedlichen Temperaturen und Dichten bilden zusammen den zentralen Apparat, welcher starke Breitbandemissionen erzeugt. Abhängig von der Beobachtungsrichtung lassen sich unterschiedliche Eigenschaften feststellen und damit AGN in verschiedene Kategorien einteilen. Das TANAMI-Programm (*Tracking Active galactic Nuclei with Austral Milliarcsecond Interferometry*) beobachtet helle kompakte Radioquellen am südlichen Himmel. Viele TANAMI Quellen wurden ebenfalls im hoch-energetischen γ -Bereich mit dem γ -Strahlen-Observatorium *Fermi*/LAT beobachtet. Die Breitbandspektren radiolauter AGN, die ein flaches Emissionsspektrum aufweisen (*flat-spectrum radio quasar*, FSRQ), können durch ein spezifisches Emissionsmodell beschrieben werden. Aktuelle Theorien der Strahlungsprozesse, die für die Emissionen verantwortlich sind, prognostizieren, dass die spektrale Energieverteilung (SED) einer Quelle charakteristisch durch zwei Buckel dargestellt wird. Je ein Maximum der Verteilung befindet sich im Radiobereich und im γ -Bereich. Manche FSRQs sind allerdings noch undetektiert und bleiben deswegen ausgeschlossen aus dem *Fermi*/LAT Katalog. Die radiolaute Quellen PKS 0438–436, PKS 1257–326, PKS 1915–458 und PKS 2106–413 gehören zu dieser Gruppe.

Um die geringe Detektionsstatistik der obengenannten FSRQs im γ -Bereich besser verstehen zu können, wurden durch AIPS kalibrierte TANAMI Daten für jede Quelle untersucht, die bei 8.4 GHz aufgenommen worden sind. Durch Verarbeitung mit DIFMAP wurde für jede Epoche jeder der Quellen eine entfaltete Karte (clean map) hergestellt, wofür anschließend ein selbst-konsistentes Modell für jede Quelle entwickelt wurde. Die Auswertung der sich ergebenden Daten wurde anhand des wissenschaftlichen Hintergrundes diskutiert und mit aktuellen Veröffentlichungen anderer Autoren verglichen, um die Rarität von γ -Detektionen der FSRQs einzuordnen.

Die vier Hauptgründe, die dazu beitragen könnten, dass die FSRQs bisher nicht detektiert worden sind, lassen sich folgendermaßen zusammenfassen: Absorption durch das extragalaktische Hintergrundlicht aufgrund hoher Rotverschiebung, Verschiebung des Maximums der spektralen Energieverteilung aus dem γ -Beobachtungsfenster aufgrund hoher Leuchtkraft der Quelle, γ - γ Wechselwirkungen und Paarbildung innerhalb der Broad Line Region der AGN, oder die Möglichkeit einer zu schwachen γ -Emission für eine signifikante Detektion. Die nicht vorhandenen oder seltenen γ -Detektionen der un-

tersuchten FSRQs lassen sich entweder durch eine oder mehrere der genannten Gründe erklären, mit einigen außergewöhnlichen Fällen bezüglich Morphologie und gemessener Jetgeschwindigkeit.

Abstract

Radio-loud active galactic nuclei (AGN) emit collimated relativistic jets which can be studied at astoundingly high resolutions through the technique of Very Long Baseline Interferometry (VLBI). The standard model of such objects comprises a supermassive black hole (SMBH) at the centre of the galaxy, surrounded by an accretion disc, a torus of cold dust, and clouds of gas with different temperatures and densities. Together, these components make up the central engine, which provides the energy for the strong emissions from AGN which are detected across the electromagnetic spectrum. Based on their angle relative to our line of sight, AGN are categorised according to their observable characteristics.

The multiwavelength monitoring TANAMI collaboration (Tracking Active galactic Nuclei with Austral Milliarcsecond Interferometry) observes bright, compact radio sources in the southern sky. After the launch of *Fermi*/LAT, many of the AGN in the TANAMI sample were observed at γ -ray energies. Based on the current models for radiation processes of AGN, the spectral energy distributions of flat-spectrum radio quasars (FSRQs) are expected to show two peaks, one at radio energies and the other at γ -ray energies. However, some FSRQs do not behave according to this expectation and remain excluded from the *Fermi*/LAT catalogue. PKS 0438–436, PKS 1257–326, PKS 1915–458 and PKS 2106–413 are radio loud AGN which fall into this category.

In order to understand the rarity of γ -ray detections of the sources in this sample, AIPS calibrated TANAMI data observed at 8.4 GHz for each source are analysed. By processing the VLBI data with DIFMAP, deconvolved images (clean maps) are produced and a self-consistent multi-epoch model is developed for each of the four FSRQs in the sample. With careful consideration of the relevant scientific background presented in the first half of this thesis and building on previously published findings, the morphology and physical parameters are discussed with the aim of explaining the lack of detections at γ -ray energies from the sources in this sample.

The four main explanations for the γ -ray quiescence of these sources can be briefly summarised as follows: absorption in the extragalactic background light due to a high redshift, high luminosity of a source causing the high-energy peak to be redshifted outside the window of γ -ray observations, γ - γ interactions and pair production within the broad line region of the source, and the possibility that the emissions are overall too weak to reach the detection threshold levels. The absence or rarity of γ -ray detections of each FSRQ in the sample can be explained by one or a combination of these possibilities, with a few exceptional cases regarding unusual morphology and superluminal motion.

Contents

Abstract	iii
1. Introduction	3
2. Scientific Background	5
2.1. Active Galactic Nuclei (AGN)	5
2.1.1. Characteristics of AGN	5
2.1.2. Classification and Unification of AGN	7
2.1.3. Radio Jets	11
2.1.4. Broadband Emission Characteristics	17
2.2. Radiation Processes	19
2.2.1. Synchrotron Radiation	19
2.2.2. Inverse Compton Scattering	23
2.2.3. Hadronic Processes	25
2.2.4. γ - γ Pair Production	26
2.3. Very Long Baseline Interferometry (VLBI)	29
2.3.1. The Two-Element Interferometer	30
2.3.2. Array Interferometry	34
3. Observations and Data Reduction	39
3.1. The TANAMI Programme	39
3.2. Data Reduction with DIFMAP	41
3.2.1. Imaging	41
3.2.2. Model Fitting	43
3.3. Further Data Analysis	44
4. Results	45
4.1. PKS 0438–436	46
4.1.1. Imaging	46
4.1.2. Model Fitting	47
4.1.3. Brightness Temperature	49
4.1.4. Flux Density	51
4.1.5. Kinematics	51
4.2. PKS 1257–326	52
4.2.1. Imaging	52

4.2.2.	Model Fitting	53
4.2.3.	Brightness Temperature	54
4.2.4.	Flux Density	57
4.2.5.	Kinematics	57
4.3.	PKS 1915–458	58
4.3.1.	Imaging	58
4.3.2.	Model Fitting	59
4.3.3.	Brightness Temperature	59
4.3.4.	Flux Density	60
4.3.5.	Kinematics	61
4.4.	PKS 2106–413	64
4.4.1.	Imaging	64
4.4.2.	Model Fitting	67
4.4.3.	Brightness Temperature	68
4.4.4.	Flux Density	68
4.4.5.	Kinematics	70
5.	Discussion	73
5.1.	Possible Reasons for γ -ray Faintness	73
5.2.	Individual Discussion of Sources	76
5.2.1.	PKS 0438–436	76
5.2.2.	PKS 1257–326	80
5.2.3.	PKS 1915–458	82
5.2.4.	PKS 2106–413	85
5.3.	Conclusions	88
6.	Summary & Outlook	89
A.	Individual Images of all sources	93
A.1.	Individual Images of PKS 0438–436	94
A.2.	Individual Images of PKS 1257–326	98
A.3.	Individual Images of PKS 1915–458	100
A.4.	Individual Images of PKS 2106–413	101
	Bibliography	103
	List of Figures	109
	List of Tables	111

1. Introduction

sic itur ad astra

Virgil

What is so interesting about PKS 0438–436, PKS 1257–326, PKS 1915–458 and PKS 2106–413? All four objects are flat-spectrum radio quasars with rare or no γ -ray detections. However, that is where the similarities stop. With a range of unusual characteristics among the sample including apparent superluminal motion on scales upwards of one hundred times the speed of light and a jet which travels along a boomerang-like bend, these four FSRQs have been studied extensively in the aim of understanding their shared quality: their γ -ray quiescence. There are four main factors which, alone or in combination with each other, could be responsible for the γ -ray behaviour seen from the sources in the sample chosen for this thesis.

The first possibility is that the γ -ray emissions from an object located at a high redshift interact with the extragalactic background light and are thus absorbed before detection. The second consideration is that due to the high luminosity of the source, the entire spectral energy distribution is redshifted, causing the γ -ray peak to be shifted to the left and the γ -ray spectrum to become steeper. This corresponds to weak emissions above a certain energy and the source remains undetected at γ -ray energies. The next plausible factor in determining γ -ray detectability is γ - γ absorption and pair production with photons in the gas clouds surrounding the central region of an active galactic nucleus. The fourth possibility is that the flux of the emissions is too weak overall and has not reached the detection threshold for *Fermi*/LAT or other γ -ray instruments. Perhaps the flux is generally too weak, or perhaps the source has not undergone a phase of high γ -ray activity since observations have started.

In order to better understand this unusual behaviour, the relevant theoretical background behind the mechanisms responsible for powering the active galactic nuclei are introduced in Sec. 2.1. Subsequently, the radiation processes which form the expected two-peaked spectral energy distribution are introduced in Sec. 2.2. Following this, the basics of radio interferometry and very long baseline interferometry are covered in Sec. 2.3. The TANAMI VLBI network is introduced in Sec. 3.1, followed by a description of the imaging and model fitting procedure applied to the data in Sec. 3.2.

The findings of each source are presented individually in Sec. 4, with time-evolution plots of the individual source's morphology, tables with all relevant model fitting parameters, and plots of the individual components' flux and brightness temperature evolution.

These results are then analysed and discussed in Sec. 5, comparing the conclusions of this thesis with published findings relevant to either the individual sources or to the question at the core of this thesis. The conclusions drawn are summarised in Sec. 6 and all supplementary images are included in Appendix A.

2. Scientific Background

2.1. Active Galactic Nuclei (AGN)

Active galaxies are fascinating objects which emit extremely strong radiation - so strong that it cannot be accounted for by stellar emissions from within the galaxy (Peterson 1997). The emissions originate from very small central regions of active galaxies - so-called Active Galactic Nuclei, or AGN. Some AGN emit radiation over the whole electromagnetic spectrum, from the radio as far as γ -ray range (Schneider 2015). AGN are also unusual with respect to cosmological evolution in that the population of the most luminous active galaxies was much larger at $z = 2.5$ than at present. The dependence of luminosity on redshift indicates that the formation of an active galactic nucleus is more likely to occur in a young galaxy (Krolik 1999). This chapter aims to explain the characteristics of AGN which are pertinent to this work. For comprehensive explanations of AGN, please refer to Schneider (2015), Beckmann and Shradler (2012) and Peterson (1997).

2.1.1. Characteristics of AGN

Active galactic nuclei are classified by their observational characteristics. Although AGN share many features, not all are observable in each individual source. The commonly accepted model comprises a supermassive black hole (SMBH) which produces energy via gravitational infall of material which is then heated in the accretion disc. A torus of dust accumulates around the "central engine" (see Sec. 2.1.2 for details). "Radio loud" AGN produce radio emissions in the form of relativistic jets perpendicular to the plane of the accretion disc. These jets can propagate with apparent velocities much larger than the speed of light c . This phenomenon will be described in further detail in Sec. 2.1.3. The most frequently shared common properties between various AGN are the astonishingly small angular size and luminosities ranging from $\sim 10^{42}$ erg/s to $\sim 10^{48}$ erg/s (Krolik 1999). Extreme luminosity variability on timescales of hours to years is also characteristic of AGN. This variability is present in both radio-quiet and radio-loud AGN (Ulrich et al. 1997). This large variability is connected with strong polarization of the emission, compact radio structure and strong emissions of high-energy γ -rays. Another aspect which is indicative of an AGN is the broadband continuum emission spectrum with radiation ranging from radio to TeV γ -ray emissions. Figure 2.1 displays the characteristic spectral behaviour of a quasi-stellar object (QSO), with

solid lines denoting the spectrum of radio-quiet QSOs and dashed lines representing the emission spectrum of radio-loud QSOs, the differences between which will be explained further in Sec. 2.1.2. At first glance, a power-law appears to be a good approximation of the spectral energy distribution (SED) of an AGN. Further inspection quickly reveals that under this approximation, many key details are excluded, including peaks and dips in the emission spectrum which are strong indicators of the emissions' origin (Peterson 1997).

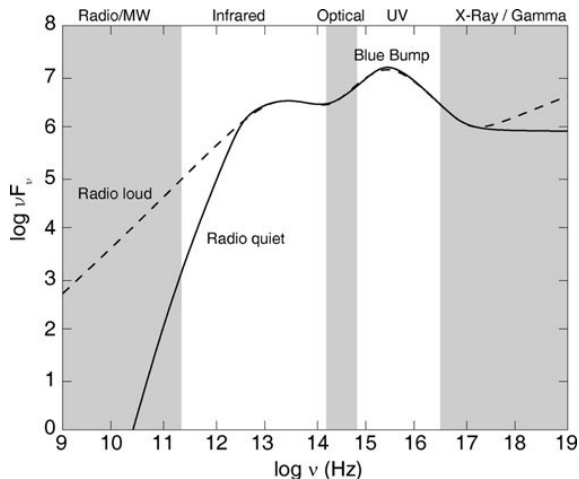


Figure 2.1.: A sketch of the characteristic spectral behaviour of a QSO. The dashed line indicates the spectrum of a radio-loud AGN, whereas the solid line illustrates the spectrum of a radio-quiet AGN. The "Big Blue Bump" is visible in the UV up to the soft X-ray region of the spectrum with a secondary maximum in the IR. Image credit: Schneider (2015).

The most notable feature in Fig. 2.1 is the so-called "Big Blue Bump", a broad peak in the continuum created by thermal emissions from the accretion disc. A secondary peak is present in the infrared range, which can be attributed to thermal emission of warm dust ($T \lesssim 2000$ K) (Schneider 2015). It is important to note that not all AGN display a peak in accordance with the big blue bump, especially radio-loud quasars in which a flat-spectrum core is prominent in the radio structure (Krolik 1999). The spectra of such sources can often be very closely approximated by power laws. Due to the variability and polarisation of the emissions from such AGN, it is believed that the radiation is produced by synchrotron radiation in the relativistic jets (Schneider 2015). The mechanism of this radiation process will be further explained in Sec. 2.2.1.

AGN characteristically display strong emission lines. The first observation of these high-excitation nuclear emission lines was made by Carl Seyfert (1943), who identified both broad and narrow emission lines and noticed that some showed strongly asymmetrical radiation with stronger emissions in the violet direction than the red. The broad emission lines with widths $\gtrsim 1000$ km/s and the narrow, nonvariable forbidden emission lines will be further explained in Sec. 2.1.2. Additionally, several categories of AGN emit strong X-ray radiation, which is understood to originate from the most central regions of the AGN due to the nature of the kilosecond timescale variation which constrains the emission region (Beckmann and Shrader 2012). Through studying these emissions, the flux of which contributes between 5 – 40% of the bolometric emissions (Ward et al. 1987), more information on the inner structure of the AGN can be gained (Schneider 2015).

2.1.2. Classification and Unification of AGN

Active galactic nuclei are classified based on the observable characteristics mentioned in the previous section. An overview of the classification scheme of AGN is presented in Table 2.1. The unification model as displayed in Fig. 2.3 presents the idea that the angle of observation defines the observables. The first classification criterion is the detection of radio emission, corresponding to the presence of a jet. It is important to note that "radio-quiet" does not imply a total lack of radio emission; all quasars display some radio emission. This distinction is made based on the value of R , the ratio of radio flux density to optical flux density. Radio-loud quasars make up only 10% of all quasars (Beckmann and Shrader 2012) and are classified as such when $R \geq 10$, whereas radio-quiet quasars are classified as such for $0.1 < R < 1$ (Kellermann et al. 1989). Radio-quiet AGN consist of quasi-stellar objects (QSOs), which are subdivided into Type 1 or Type 2 based on the manifestation of broad and narrow emission lines, and Seyfert galaxies. Seyfert galaxies, first observed by Carl Seyfert (1943), are lower luminosity AGN mostly present in spiral galaxies which are identified by their nuclear emissions. Khachikian and Weedman (1974) further divided the Seyfert galaxies into subclasses Seyfert 1 and 2 based on the relative widths of the emission lines. In Seyfert 1 galaxies, the Balmer series appears broader than the forbidden lines, whereas in Seyfert 2 galaxies, both the Balmer and the forbidden lines appear with the same narrow width. The initial conjecture that QSOs are the more distant analogues to Seyfert galaxies was confirmed by space-based UV observations in the 1970s and 1980s (Beckmann and Shrader 2012).

Table 2.1.: Classification Characteristics of Active Galactic Nuclei

Type	Radio Loudness	Emission Lines	Luminosity	Jet?	Radio Morphology
Seyfert 1	radio quiet	broad, narrow	low	no	none
Seyfert 2	radio quiet	narrow	low	no	none
QSO (1)	radio quiet	broad, narrow	high	no	none
QSO (2)	radio quiet	narrow	high	no	none
BLRG	radio loud	broad, narrow	low	yes	FR1
	radio loud	broad, narrow	high	yes	FR2
NLRG	radio loud	narrow	low	yes	FR1
	radio loud	narrow	high	yes	FR2
BL Lac	radio loud	none	low	yes	compact
FSRQ	radio loud	broad, narrow	high	yes	compact

Note: Table adapted from original by Matthias Kadler.

The radio-loud AGN, or quasi-stellar radio sources (quasars), are the brightest AGN and are subdivided based on the angle of observation. Sources that are orientated such that the angle of the line of sight is acute with respect to the plane of the accretion

disc are either broad line radio galaxies (BLRG) or narrow line radio galaxies (NLRG), corresponding to the presence or absence of broad emission lines respectively (Schneider 2015). Although the inner region of the quasar is not directly observable, the presence of an AGN core is inferred from the radio emissions of radio galaxies (Beckmann and Shrader 2012). Sources to which the line of sight is along or close to alignment with the radio axis of the relativistic jet are classified as blazars (Peterson 1997). Blazars are further subdivided into BL Lac objects and flat-spectrum radio quasars (FSRQs) (Beckmann and Shrader 2012). Radio-loud sources are further classified based on the morphology of their radio emissions, which can be either compact or extended. Within the class of objects which display extended radio emissions is the further subdivision between Fanaroff-Riley Class 1 (FR-1) and Class 2 (FR-2) radio galaxies. FR-1 objects are weaker than FR-2 objects and are brightest near the centre, whereas FR-2 are brightest towards the edges or within the structure of the radio emissions (Peterson 1997). Since all four objects studied in the scope of this thesis are FSRQs, more attention will be paid to these objects. For a comprehensive overview of AGN classifications, please refer to Antonucci (1993), Urry & Padovani (1995) and Lawrence (1987).

FSRQs are the brighter class of blazars and can be identified by broad Balmer lines on a nonthermal continuum. An initial criterion for distinguishing between BL Lacs and FSRQs is the equivalent width (EW) of the emission lines, with BL Lac objects identified as those with $EW < 5 \text{ \AA}$ (Beckmann and Shrader 2012). Although this is a simple and quick way to initially distinguish between the two subclasses, it is not totally reliable, since it does not account for the variability of the emission and the subsequent variability of the emission lines or for the effect of beaming (Ghisellini et al. 2011). In principle, the distance of FSRQs can be determined by studying the broad line region. However, for sources at redshifts $z > 2$, beamed emission overpowers the broad line region, making distance determination difficult. This is illustrated by Fig. 2.2, which shows the distribution of blazars according to redshift from the 13th edition of the blazar catalogue compiled by Véron-Cetty & Véron (2010). The vast majority (75%) of blazars are located at $z < 0.5$ with only very few at $z > 2$ (Beckmann and Shrader 2012). Two of these high redshift blazars are included in this work: PKS 0438–436 at $z = 2.86$ and PKS 1915–458 at

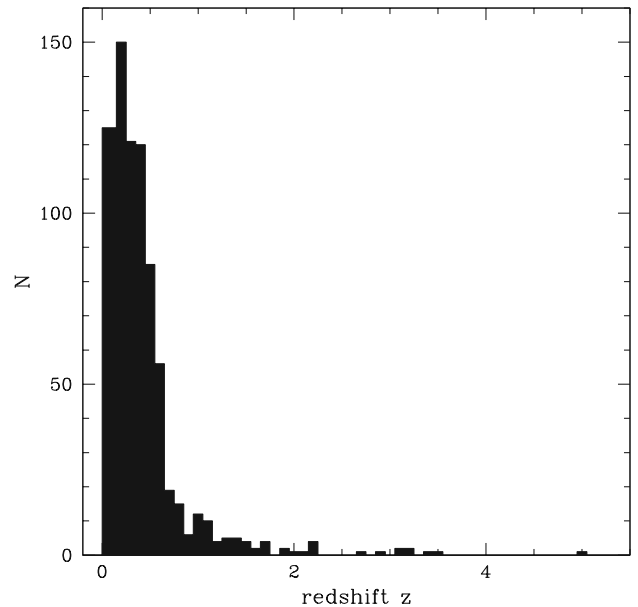


Figure 2.2.: A histogram showing the redshift distribution of the 760 blazars included in the catalogue by Véron-Cetty & Véron (2010). Image credit: Beckmann and Shrader (2012).

$z = 2.47$. The other two sources, PKS 1257–326 and PKS 2106–413, although not quite as distant, are located at $z = 1.256$ and $z = 1.058$ respectively, still significantly further away than most identified blazars.

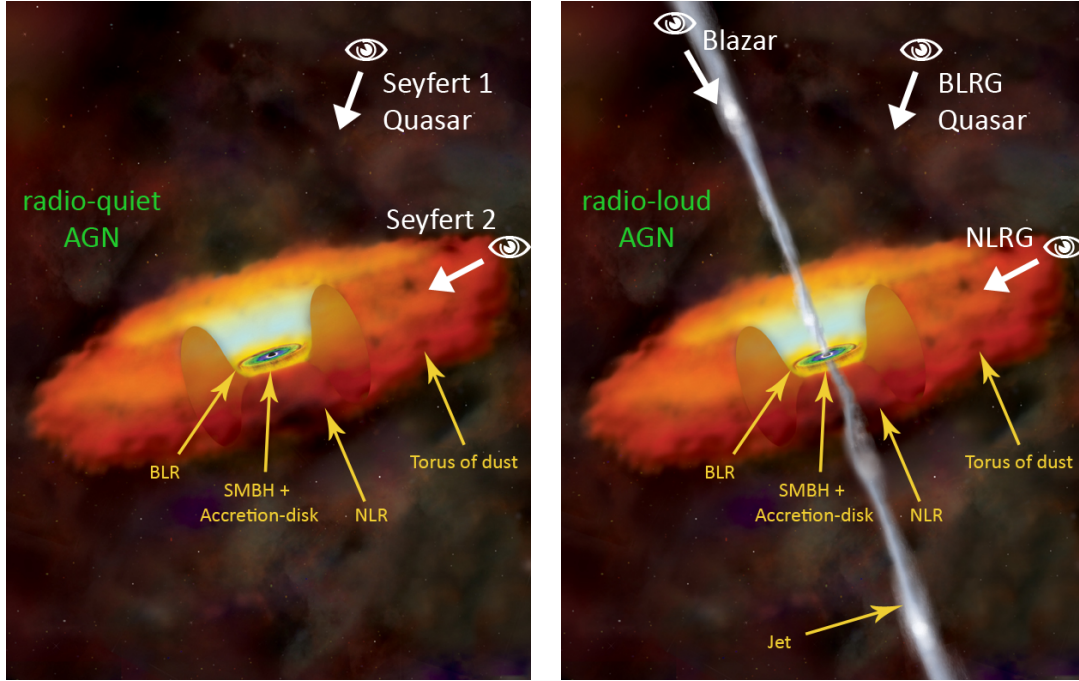


Figure 2.3.: Illustration of the AGN unification model according to Antonucci (1993) and Urry & Padovani (1995). The image on the left displays a radio-quiet AGN; the image on the right displays a radio-loud AGN. An AGN consists of a SMBH which is surrounded by the accretion disc and a torus of cold dust. The classification of an AGN depends on the angle of observation. Image Credit: Trüstedt (2013), adapted from NASA/CXC/M.Weiss.

The "Central Engine"

What provides the energy for such strong emissions across all wavelengths which are detected from AGN? The current model as pictured in Fig. 2.3 assumes that a SMBH surrounded by an accretion disc is the "central engine" of AGN (Peterson 1997). The accretion disc has a radius of approximately $r \sim 10^{-3}$ pc. Unless otherwise cited, the dimensions of the components of an AGN have been taken from Antonucci (1993). In the immediate vicinity of the SMBH and the accretion disc is the broad line region (BLR) with a radius of approximately $r \sim 0.01 - 0.1$ pc, which produces broad emission lines characteristic of AGN spectra with widths of the order $\sim 10\,000$ km/s. In order to produce such broadening, thermal line broadening would require extremely high temperatures $T \sim 10^{10}$ K, at which no emission lines would be produced because all atoms would be fully ionised. Therefore, the width of the emission lines is attributed to Doppler broadening. The BLR is not homogeneous; it has a filling factor of $\sim 10^{-7}$,

consisting of dense clouds of gas at temperatures of $T \sim 20\,000$ K (Schneider 2015). Due to its proximity to the SMBH, investigating the BLR via reverberation mapping can provide information about the innermost regions of the central engine of an AGN (Peterson 1997). A toroidal structure of cold dust surrounds the accretion disc and SMBH with a radius ranging from $r \sim 1$ to a few 10 parsecs. Depending on the line of sight, this torus can obscure the view of the central region (Beckmann and Shrader 2012). In addition to the aforementioned broad emission lines, narrow emission lines with typical widths of ~ 400 km/s are observed in the spectra of many AGN. These emission lines, while narrower than those produced in the BLR, are still broader than those in normal galaxies and are produced in the narrow line region (NLR), which is much larger than the BLR with a radius of $r \sim 100 - 1000$ pc. Smaller than that of the BLR, the NLR has a filling factor of only $\sim 10^{-2}$; the NLR is also inhomogeneous and consists of clouds of gas with temperatures of $T \sim 16\,000$ K (Schneider 2015). The NLR is the only component of an AGN which can be spatially resolved at optical wavelengths for nearby galaxies (Peterson 1997). Interestingly, this region appears as two conical regions extending from the centre of the AGN, implying that the ionising radiation of the AGN is emitted in two opposing directions perpendicular to the plane of the accretion disc (Schneider 2015). Problematically, no direct observation of a black hole is possible, due to the fact that such an object does not emit any radiation. Therefore, the observable behaviour of matter in the vicinity of the black hole must be studied in order to draw any conclusions about SMBHs (Beckmann and Shrader 2012). The following section provides fundamental arguments which support the black hole model.

Supermassive Black Holes (SMBH) Compared to the overall brightness of the host galaxy, AGN have been observed with luminosities ranging from $\sim 10^{42}$ erg/s to $\sim 10^{48}$ erg/s, as previously mentioned (Krolik 1999). From the length-scale of a source with radio emissions extending beyond 1 Mpc, a minimum age of the source can be derived to be $\gtrsim 10^7$ yr. Using this minimum age and under the assumption that the overall luminosity remains constant during the source’s lifetime, the total energy required to produce a bolometric luminosity of $L_{\text{bol}} \sim 10^{47}$ erg/s can be estimated to be $E \sim 3 \cdot 10^{61}$ erg. This estimation does not account for the variability of some AGN, however. some sources display intraday variability; these vary more than 50% in luminosity on time-scales of a day or shorter (Schneider 2015; Bignall et al. 2003). Considering this variability gives an upper limit estimate of the size of the central source $R \sim 3 \cdot 10^{15}$ cm. If nuclear fusion at maximum efficiency ($\lesssim 0.8\%$) is proposed as the main source of energy in AGN, the inner core would have to be made up of burnt-out matter with a Schwarzschild radius of $R_S = \frac{2GM}{c^2} \sim 6 \cdot 10^{14}$ cm, in the same order of magnitude as the entire central source. This is indicative of the significant role played by gravitational energy production, the only process more efficient in energy production than thermonuclear processes. The gravitational infall of the matter onto the black hole and its subsequent heating in the accretion disc can produce a maximum efficiency of $\sim 6\%$ or $\sim 29\%$ for a

non-rotating or a rotating black hole, respectively (Schneider 2015). Shakura & Sunyaev (1973) established this as the most probable mechanism of producing such high energies as emitted by AGN.

How massive is "supermassive"? A first estimate for the mass of the SMBH at the centre of an AGN can be derived from the Eddington limit, the upper limit of luminosity of an object with mass M in equilibrium with in-falling matter and radiation pressure. The process of accretion requires a bolometric luminosity $L < L_{\text{Edd}}$, with

$$L_{\text{Edd}} \lesssim \frac{4\pi GMm_p c}{\sigma_T} \simeq 1.3 \cdot 10^{38} \frac{M_\bullet}{M_\odot} \text{erg/s} \quad (2.1.1)$$

in which M_\bullet is the mass of the black hole, $\sigma_T \simeq 6.65 \cdot 10^{-25} \text{cm}^{-2}$ is the Thomson cross-section and m_p is the mass of a proton (Beckmann and Shrader 2012).

Rearranging Eq. 2.1.1 yields a lower limit for the mass of the SMBH with a given luminosity:

$$M_\bullet > M_{\text{Edd}} := \frac{\sigma_T L}{4\pi G c m_p} \approx 8 \cdot 10^7 \left(\frac{L}{10^{46} \text{erg/s}} \right) M_\odot \quad (2.1.2)$$

A quasar with a typical luminosity of $L \approx 10^{46} \text{erg/s}$ requires $M_\bullet \gtrsim 10^8 M_\odot$, whereas a Seyfert galaxy would require a black hole mass of $M_\bullet \gtrsim 10^6 M_\odot$. However, these approximations are not entirely accurate, since isotropic radiation has been assumed. The mass of the SMBH can be more accurately determined through a process called reverberation mapping, which observes the response of emission lines to continuum variations and, as previously mentioned, can also be used to study the size and structure of the broad line region (Schneider 2015; Peterson 1997).

Additionally, apparent superluminal motion of the collimated jets emitted by AGN also supports the existence of a SMBH at the core of AGN. This phenomenon will be discussed further in Sec. 2.1.3.

2.1.3. Radio Jets

The first observation of what are now recognised as jets was made by Heber Curtis in 1918. Curtis observed a "curious straight ray" emitted by galaxy M87 in the Virgo Cluster (Curtis 1918). Powered by the central engine of radio-loud AGN, jets transport energy, momentum, and angular momentum from the central region of the SMBH over distances of up to a megaparsec or more (Böttcher et al. 2012). Now identified as highly energetic, highly collimated outflows from SMBHs, jets are present in the 10 % of AGN which are identified as "radio-loud". The nonthermal continuum emission spectra displayed by these objects is caused by the synchrotron radiation of charged particles which is believed to be the mechanism for jet formation (Beckmann and Shrader 2012). The mechanism for jet formation established by Blandford & Znajek (1977) presents a model of a rotating black hole which is threaded by magnetic field lines, extracting energy and angular momentum electromagnetically. This has become the most commonly accepted

theory for powering the jet. Radiation processes for jet production are further discussed in Sec. 2.2.

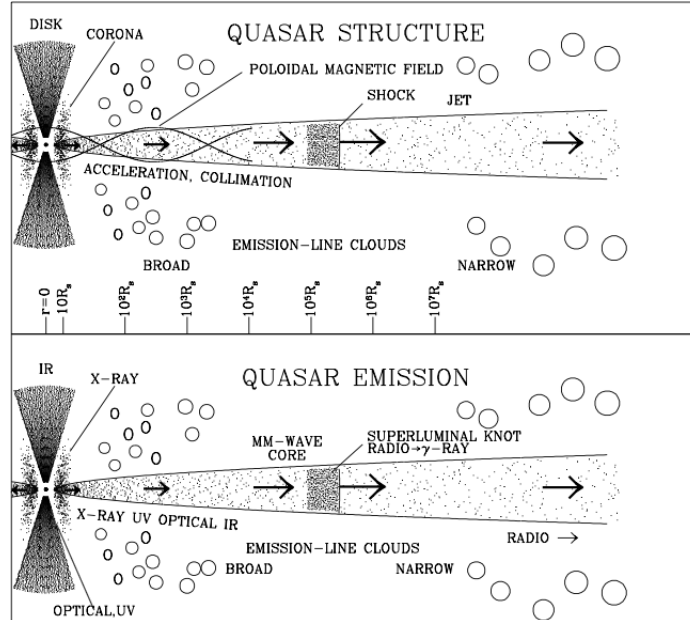


Figure 2.4.: Sketch of the structure of the jet in a radio-loud AGN. The density of the dots represents the strength of the emission and the length of the arrows corresponds to the Lorentz factor of the flow. The scale along the x -axis is logarithmic and is given in terms of the Schwarzschild radius (Beckmann and Shrader 2012). Image credit: Marscher (2005).

Figure 2.4 shows the structure of the jet in a radio-loud AGN. Jets are conical with an opening half-angle ϕ which can be as large as $\sim 5^\circ$ or smaller than 1° (Marscher 2009). A study by Jorstad et al. (2005) indicated that the opening angle ϕ is inversely proportional to the Lorentz factor γ , meaning that the speed of the jets is related to how closely the geometry of the jet can be approximated by a cylinder rather than a cone. The Lorentz factor will be further explained in the next section. The features most commonly observed in jets are the core, quasi-stationary features, and superluminal knots. The core is the most compact part of the jet and could be the area between optically thick and thin emission or a stationary component close to that transition region. The optically thick and thin regions will be addressed in Sec. 2.2.1. A third possibility is that the core could be a bend in the jet where the direction of emission comes closer to alignment with the line of sight. This phenomenon is not common and cannot explain the reliable appearance of cores in jets, since it is less likely that the jet would bend towards the line of sight than away from it. Quasi-stationary features are those identified as either stationary or moving at subluminal speeds. These can be caused by recollimation shocks in straight jets, jet bending or the formation of a shock in bent jets (Marscher 2009). The phenomenon of superluminal motion in jets is explained in detail later in this section.

Doppler Boosting and Jet One-sidedness

The relativistic motion of jets requires the consideration of relativistic effects, particularly the effect of boosting as caused by the Doppler shift. The Doppler shift increases the observed frequency and decreases the timescale of variability (Marscher 2009).

Due to this, radiation moving towards the observer will appear brighter than the source at rest by the Doppler factor

$$\mathcal{D}_+ = \left(\frac{1}{\gamma(1 - \beta \cos \theta)} \right)^{2+\alpha} \quad (2.1.3)$$

in which $\beta = \frac{v}{c}$, $\gamma = (1 - \beta^2)^{-\frac{1}{2}}$ is the Lorentz factor, θ is the angle between the line of sight and the velocity vector of the jet and α is the spectral index (Schneider 2015). For $v \rightarrow c$, this factor can become very large. Due to the same beaming mechanism, in the case of a counterjet moving in the opposite direction of the main jet, the radiation moving away from the observer will appear weaker than the source at rest by a factor

$$\mathcal{D}_- = \left(\frac{1}{\gamma(1 + \beta \cos \theta)} \right)^{2+\alpha} \quad (2.1.4)$$

For a jet of intensity $I(\nu)$, it can be shown that $I(\nu)/\nu^{-3}$ is Lorentz invariant and because the flux density $S(\nu) \propto I(\nu)$, it follows that $S(\nu)/\nu^{-3}$ is also Lorentz invariant (Rybicki & Lightman 1979). As such, for a source which follows a power law $S(\nu) \propto \nu^{-\alpha}$ (as will be further explained in Sec. 2.2), the observed flux density is given by

$$S_{\text{obs}}(\nu) = \mathcal{D}^{3+\alpha} S_{\text{emit}}(\nu) \quad (2.1.5)$$

in which \mathcal{D} is the relativistic Doppler factor, S_{obs} is the observed flux density and S_{emit} is the emitted flux density. The ratio of the flux of the jet to the counterjet is given by

$$R = \frac{S_{\text{jet}}}{S_{\text{counterjet}}} \frac{\mathcal{D}_+}{\mathcal{D}_-} = \left(\frac{1 + \beta \cos \theta}{1 - \beta \cos \theta} \right)^{2+\alpha} \quad (2.1.6)$$

and the logarithm of this ratio is plotted as a function of the viewing angle θ in Fig. 2.5. It is notable that the flux ratio becomes almost independent of the Lorentz factor for large viewing angles (Urry & Padovani 1995). The flux ratio and the curves plotted

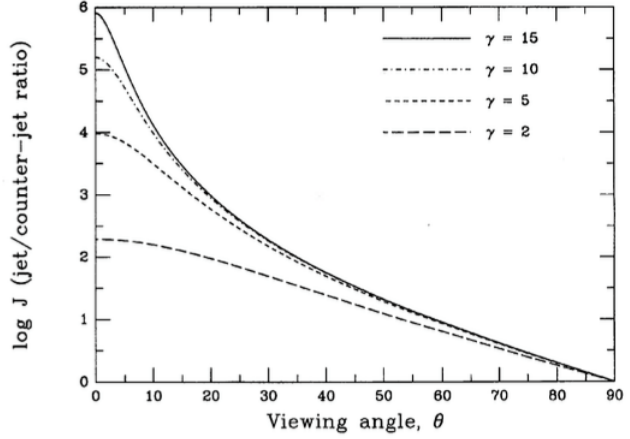


Figure 2.5.: The logarithm of the ratio of the flux of the jet and counterjet of an AGN as a function of viewing angle θ for different values of the Lorentz factor γ . Image credit: Urry & Padovani (1995).

in Fig. 2.5 explains the effect of "Doppler favouritism", the reason why most compact radio AGN are viewed as one-sided (Schneider 2015).

Brightness Temperature

In VLBI radio astronomy, the components of the jets have a "brightness temperature", which is the required temperature of a black body in order to emit radiation at the observed intensity at a frequency ν (Burke & Graham-Smith 2010). When fitting jet features with Gaussian components (see Sec. 3.2.2 for further details), the brightness temperature of a component in the rest frame of the source is given by

$$T_B = \frac{2 \ln 2}{\pi k} \frac{S_{\text{comp}} \lambda^2 (1+z)}{ab} \quad (2.1.7)$$

in which S_{comp} is the flux density of the component, a and b are the FWHMs of the Gaussian components along the major and minor axes respectively, λ is the wavelength of observation, z is the redshift of the source, and k is the Boltzmann constant (Kovalev et al. 2005). Upper limits are set on the value of T_B by physical limitations such as equipartition, which sets a limit of 10^{11} K (Readhead 1994), or the inverse Compton limit of 10^{12} K according to Kellermann & Pauliny-Toth (1969)(see Sec. 2.2.2 for further details). However, as stated by Kovalev et al. (2005), the value of T_B may exceed these limits, most likely due to the previously mentioned Doppler boosting. If this causality is true and if the range of intrinsic brightness temperatures is small, there should be a clear connection between T_B and the apparent jet velocity β_{app} , i.e. the highest speeds should be observed in the sources with a high brightness temperature.

Superluminal Motion

As mentioned in Sec. 2.1.2, the apparent superluminal velocities of jet components emitted by AGN also supports the generally accepted theory that a SMBH lies at the centre of an AGN, functioning in cooperation with the accretion disc as the central engine.

The most favoured model is that the superluminal motion of "knots" in radio jets is caused by shocks in the collimated plasma outflow (Blandford & Königl 1979). These knots, which are visible as regions of high intensity in VLBI images of AGN, represent localised peaks in either the magnetic field strength, relativistic electron density, or both. The shockwaves are usually modelled as transverse square waves which are caused by irregularities in the energy density or accelerations at the origin of the jet (Marscher 2009). An alternative model to these shockwaves is the "blob" model, which presents the knots as regions of higher density plasma which propagate along the jet flow (Beckmann and Shrader 2012).

Figure 2.6 shows a sketch of the superluminal motion of the knots in relativistic jets. The knot emits signals at times t_1 and $t_2 = t_1 + \Delta t$ and the observer sees signals separated

by

$$\Delta t_{\text{obs}} = \left(1 - \frac{v}{c} \cos \theta\right) \Delta t_{\text{emit}} \quad (2.1.8)$$

As the knot propagates along the jet, the observed distance travelled is

$$\Delta x = v \Delta t_{\text{emit}} \sin \theta \quad (2.1.9)$$

which yields the observed transverse velocity

$$v_{\text{app}} = \frac{v \sin \theta}{1 - \frac{v}{c} \cos \theta}, \quad \beta_{\text{app}} = \frac{v_{\text{app}}}{c} \quad (2.1.10)$$

for which $\theta = 0$ and $\theta = \pi$ correspond to a jet orientation directly towards or away from the observer, respectively.

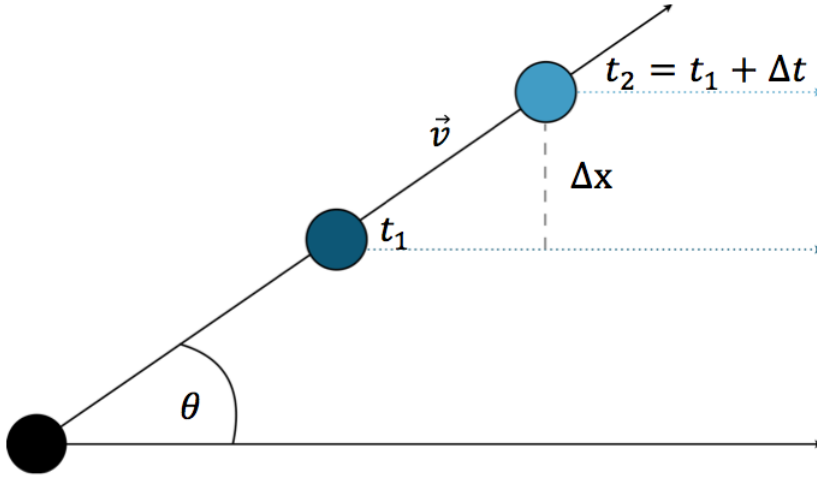


Figure 2.6.: Sketch of the geometry to explain the apparent superluminal motion of radio sources. A component moves with velocity v at an angle θ from the line of sight. For a detailed explanation, refer to the text.

According to Eq. 2.1.10, superluminal motion will be observed for relativistic motion $v \lesssim c$ with a small angle θ . However, this initial estimation is only valid for sources close to the point of observation and does not account for redshift or the expansion of the universe. Unless otherwise stated, the following explanation has been adapted from Chodorowski (2005), in which a detailed derivation of this effect from first principles is executed. In order to correctly estimate the apparent velocity of a jet component, the values of the redshift, proper motion, and angular diameter distance must be identified. The redshift z of an object is defined as the difference between the observed and emitted wavelength of light

$$z \equiv \frac{(\lambda_{\text{obs}} - \lambda_{\text{emit}})}{\lambda_{\text{emit}}} \quad (2.1.11)$$

The proper motion μ of an AGN is defined as the change in time of its angular position on the sky

$$\mu = \frac{\Delta\phi}{\Delta t} \quad (2.1.12)$$

The angular diameter distance D_A is dependent on the redshift of an object and is related to the luminosity distance D_L and the distance measure D by

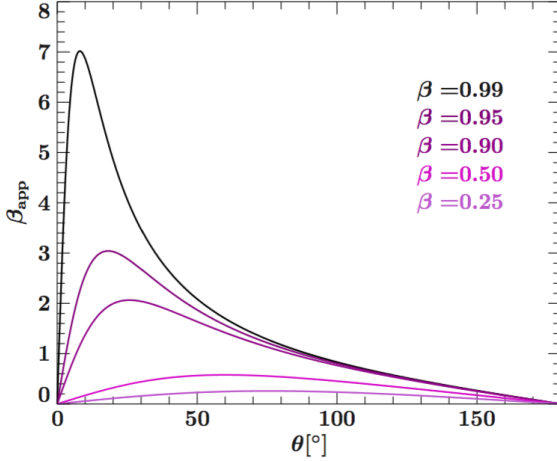


Figure 2.7.: The apparent velocity β_{app} is plotted as a function of the inclination angle θ for different intrinsic values of $\beta = v/c$. Image credit: Müller (2014).

The value usually referred to as "apparent velocity" in literature should actually be referred to as the "velocity measure"

$$v_m = (1 + z)v_{\text{app}} \quad (2.1.16)$$

which is the velocity which would be observed if one were located at the redshift z of the observed source. The apparent velocity β_{app} is highly dependent on the angle θ . Figure 2.7 shows that for $\beta \rightarrow 1$ and for small θ , the apparent velocity β_{app} can exceed the speed of light c . The values given for β_{app} in Sec. 4 have been corrected for the contributions from redshift and also account for the expansion of the universe. The values of the cosmological constants used to calculate these velocities are $H_0 = 70 \text{ km/s/Mpc}$, $\Omega_k = 0$ is the curvature constant for which the value of 0 corresponds to a flat universe, $\Omega_m = 0.3$ is the mean density of non-relativistic matter in the universe in units of critical density and $\Omega_\Lambda = 0.7$ is the cosmological constant Λ in units of critical density.

$$D_L = (1 + z)D = (1 + z)^2 D_A \quad (2.1.13)$$

which is related to the physical size Δy of an object which subtends the angle $\Delta\phi$ on the sky by

$$\Delta y = D_A \Delta\phi \quad (2.1.14)$$

yielding the true apparent transverse velocity of

$$v_{\text{app}} = \mu D_A \quad (2.1.15)$$

which is affected by the recession velocity of the source according to the current model of the expansion of the universe.

2.1.4. Broadband Emission Characteristics

The characteristic broadband emission spectrum of AGN has been attributed to synchrotron emission for photons at lower energies and inverse Compton processes for photons at higher energies. Figure 2.8 shows the blazar sequence according to Fossati et al. (1998). The typical spectral energy distribution of a blazar shows two prominent peaks. The presence of the lower peak is attributed to synchrotron radiation, whereas the exact emission processes which produce the higher peak are still under discussion. The first

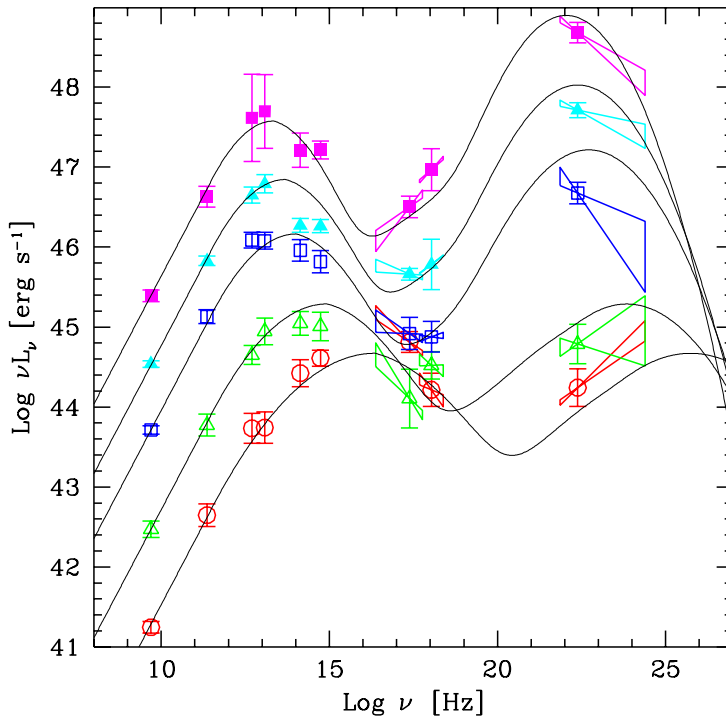


Figure 2.8.: Average SEDs for the total blazar sample, showing the characteristic double hump structure. Image credit: Fossati et al. (1998).

peak appears at different frequency ranges for different objects and is anticorrelated with the luminosity - more luminous sources have peaks at lower frequencies. The frequencies of the two peaks are also correlated; the smaller the frequency of the lower peak, the smaller the frequency of the high-energy component. Additionally, the luminosity ratio between the high and low frequencies increases with the bolometric luminosity of the source (Fossati et al. 1998). Even though the SEDs pictured in Fig. 2.8 are typical of blazar emissions, there are many cases in which bright radio-loud blazars have not been detected in the γ -ray range. Lister et al. (2015) studied the complete MOJAVE 1.5 Jy sample of AGN and discovered that many of the brightest radio-loud blazars in the northern sky have not been detected above 0.1 GeV by *Fermi*/LAT. The hypothesis presented by Lister et al. (2015) is based on the correlation of the peak frequencies between the two peaks. Blazars with synchrotron peaks located below $10^{13.4}$ Hz have

high-energy peaks which are located below the *Fermi*/LAT threshold of 0.1 GeV and as such are less likely to be detected by *Fermi*/LAT.

Figure 2.9 shows the distribution of synchrotron radiation peak frequency in rest and observer frames for sources which have and have not been detected by *Fermi*/LAT. The blue dashed lines represent those which have been detected. All of the non-detected AGN in this sample have synchrotron peak frequencies below $10^{13.4}$ Hz. Although these sources are in the northern sky, it is reasonable to assume that the detection of TANAMI sources by *Fermi*/LAT encounter the same hurdles and that this is analogous for the southern sky. This might help to explain why two of the four FSRQs studied in the scope of this work have not yet been detected in the γ -ray range by *Fermi*/LAT. Another hypothesis for the lack of γ -ray detection is the extragalactic background light (EBL). The EBL is defined as the integrated flux from all unresolved extragalactic sources (Bernstein 2006). It is possible that the γ -ray emission from FSRQs undergoes intergalactic absorption, caused by photon-photon collision and pair production. The intergalactic absorption coefficient, also called the optical depth $\tau(E)$, depends on the SED of the EBL. The intrinsic spectrum of the source is influenced according to the absorption given by $F_{\text{obs}}(E) = F_{\text{int}}(E) \cdot e^{-\tau(E)}$ (Aharonian et al. 2006). This energy dependence causes the intrinsic source spectrum to steepen as it is observed on Earth (Stecker et al. 2007). This steepening could also cause difficulties in observations with *Fermi*/LAT and other γ -ray instruments. Although the intergalactic γ -ray absorption could very well contribute to the lack of γ -ray detections, it is more likely that the main cause is pair production caused by interactions with photons in the BLR. Although the composition of jets is not yet clear, leptonic models are favoured by current research in blazars, but hadronic models cannot be eliminated (Beckmann and Shrader 2012). The first model proposed by Blandford & Königl (1979) considers a purely leptonic composition, which was later extended by Mannheim (1993) who presented evidence for the existence of an ultra-relativistic proton population in jets. Although the favoured models are purely leptonic, it is possible that the fundamental principles of leptonic models also apply to lepto-hadronic models (Beckmann and Shrader 2012). The processes included in both models will be discussed in Sec. 2.2, including leptonic processes, hadronic processes, and the absorption process relevant for γ -rays in astrophysical environments.

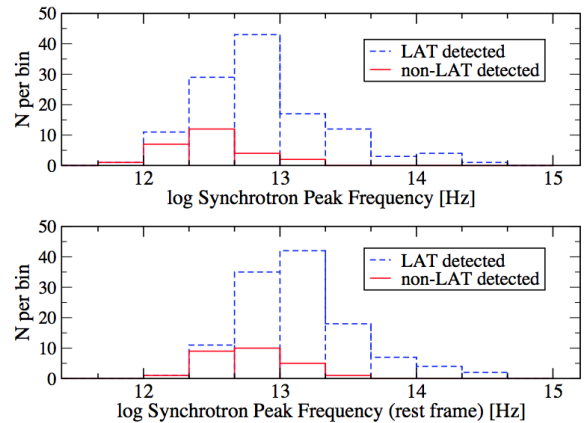


Figure 2.9.: Distributions of the observed synchrotron peaks for *Fermi*/LAT detected (blue dashed line) and non-*Fermi*/LAT detected blazars. The lower panel displays the same distribution for rest frame synchrotron peak frequency. Image credit: Lister et al. (2015).

2.2. Radiation Processes

As stated in Sec. 2.1.4, the emission spectrum of AGN can be modelled either with purely leptonic or lepto-hadronic models. The processes which dominate the SEDs of such sources will be explained in the following sections. For an extensive overview of the radiation processes relevant to AGN, please refer to Böttcher et al. (2012), Rybicki & Lightman (1979) and the sources within.

2.2.1. Synchrotron Radiation

Extremely relativistic particles accelerated in a magnetic field emit synchrotron radiation, the frequency spectrum of which can be as large as several times the gyration frequency. This process causes the radio emission observed in AGN (Beckmann and Shradler 2012). The process described in the following section is based on Rybicki & Lightman (1979) unless otherwise cited. Considering a particle with mass m and charge q in a magnetic field, the equation of motion is given by

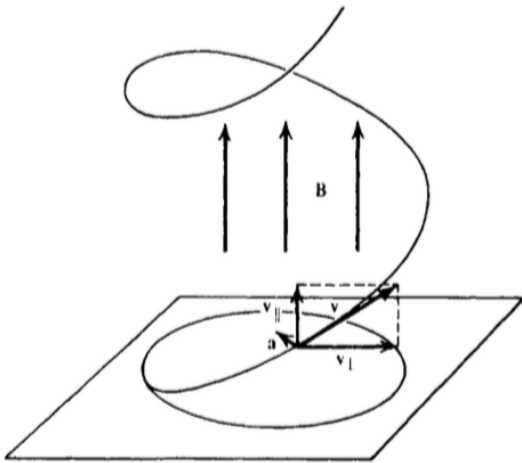


Figure 2.10.: Helical motion of a relativistic particle in a uniform magnetic field. Image credit: Rybicki & Lightman (1979).

$$\frac{d}{dt}(\gamma m \vec{v}) = \frac{q}{c}(\vec{v} \times \vec{B}) \quad (2.2.1)$$

$$\frac{d}{dt}(\gamma m c^2) = q \vec{v} \cdot \vec{E} = 0 \quad (2.2.2)$$

in which \vec{v} is the velocity of the particle and $\gamma = (1 - \beta^2)^{-\frac{1}{2}}$ is the Lorentz factor of the electrons with $\beta = v/c$. The Lorentz factor γ and $|\vec{v}|$ are constant. Separating the velocity into components parallel to the field \vec{v}_{\parallel} and normal to the field \vec{v}_{\perp} gives

$$\frac{d\vec{v}_{\parallel}}{dt} = 0, \quad \frac{d\vec{v}_{\perp}}{dt} = \frac{q}{\gamma m c} \vec{v}_{\perp} \times \vec{B} \quad (2.2.3)$$

which shows that \vec{v}_{\parallel} is constant and since $|\vec{v}|$ is also constant, it follows that $|\vec{v}_{\perp}|$ is also constant. The solution of uniform circular motion of the projected motion on the normal plane combined with uniform motion along the field yields helical motion as illustrated in Fig. 2.10 with the angular gyrofrequency

$$\omega_B = \frac{qB}{\gamma m c} \quad (2.2.4)$$

which accelerates perpendicular to the velocity with magnitude $a_{\perp} = \omega_B v_{\perp}$. The total emitted radiation is then given by

$$P = \frac{2}{3} r_0^2 c \beta_{\perp}^2 \gamma^2 B^2 \quad (2.2.5)$$

in which $r_0 = \frac{e^2}{mc^2}$. Averaging over all angles for a given speed β to account for an isotropic velocity distribution with the pitch angle α between the velocity vector and the magnetic field gives

$$\langle \beta_{\perp}^2 \rangle = \frac{\beta^2}{4\pi} \int \sin^2 \alpha d\Omega = \frac{2\beta^2}{3} \quad (2.2.6)$$

$$P = \left(\frac{2}{3}\right)^2 r_0^2 c \beta^2 \gamma^2 B^2 \quad (2.2.7)$$

which can be written as

$$P = \frac{4}{3} \sigma_T c \beta^2 \gamma^2 U_B \quad (2.2.8)$$

where $\sigma_T = 8\pi r_0^2/3$ is the Thomson cross-section and $U_B = \frac{B^2}{8\pi}$ is the magnetic energy density. Since the Thomson cross-section σ_T is proportional to $1/m^2$, the emitted power also scales with the mass, meaning that the radiation of massive particles is negligible.

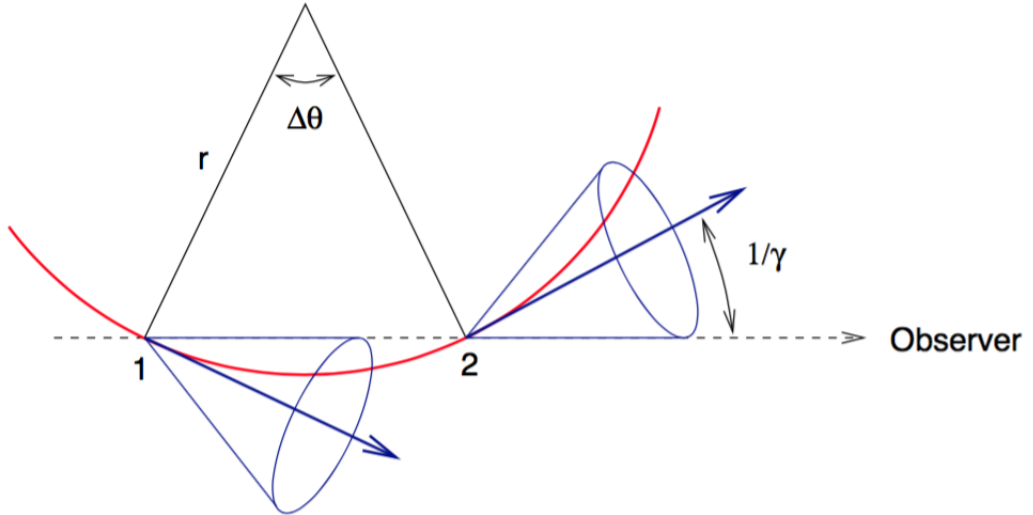


Figure 2.11.: Synchrotron emission cones of a charged particle on a helical trajectory through a magnetic field. Image credit: Rybicki & Lightman (1979).

Due to the perpendicularity of the acceleration to the velocity, the observer will see pulses along the particle's path which are emitted in cones with axes along the velocity vector \vec{v} with an angular width of $1/\gamma$, as shown in Fig. 2.11. Points 1 and 2 in Fig.

2.11 are the points at which the observer views the synchrotron emission. The distance travelled along the path can be calculated using the radius of curvature a and the change in angle $\Delta\theta$. Considering radiation from a number of particles, the observed spectrum is continuous with a maximum at the critical frequency

$$\nu_c = \frac{\omega_c}{2\pi} = \frac{3}{4\pi}\gamma^3\omega_B \sin\alpha \quad (2.2.9)$$

For the highly relativistic case, the power per unit frequency emitted is then given by

$$P(\nu) = \frac{\sqrt{3}q^3 B \sin\alpha}{mc^2} F(x) \quad (2.2.10)$$

where $x = \nu/\nu_c$ and $F(x) = x \int_x^\infty K_{5/3}(\zeta) d\zeta$ in which $K_{5/3}(\zeta)$ is the modified Bessel function of order $5/3$ (Beckmann and Shrader 2012).

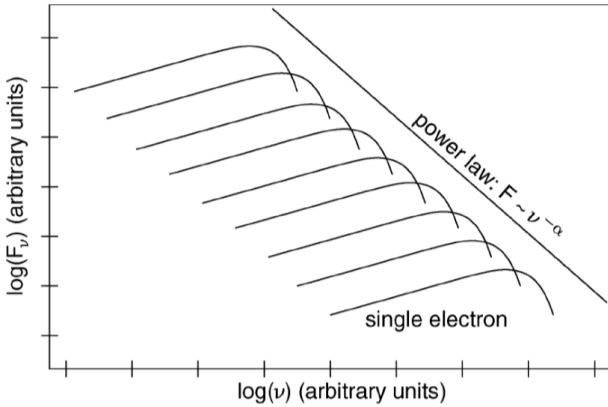


Figure 2.12.: The superposition of the spectra of electrons emitting synchrotron radiation results in a power law spectrum (assuming that the electron energy distribution follows a power law). Image credit: Schneider (2015).

The number density of particles with an energy between E and $E + dE$ is given by

$$n(E)dE = CE^{-p}dE, \quad E_1 < E < E_2 \quad (2.2.11)$$

in which C can vary with pitch angle and p is the particle distribution index. The power of nonthermal synchrotron radiation is given by

$$P(\nu) = \int_{E_1}^{E_2} P(E, \nu) n(E) dE \quad (2.2.12)$$

for which the integral is approximately constant for wide enough energy limits, meaning that the emitted spectrum is given by

$$P(\nu) \propto \nu^{-\alpha} \quad (2.2.13)$$

in which the spectral index is given by $\alpha = \frac{p-1}{2}$. This power law spectrum is illustrated in Fig. 2.12. It is important to note that this simple power law is only valid for an optically thin medium. The optical depth of a medium measured along the path of a travelling ray is given by

$$\tau_\nu(s) = \int_{s_0}^s \alpha_\nu(s') ds' \quad (2.2.14)$$

in which s_0 sets the zero point for the optical depth scale. A medium is optically thin for $\tau_\nu < 1$ and optically thick for $\tau_\nu > 1$. At low frequencies, the medium is optically thick, leading to synchrotron self-absorption, a process in which a low frequency photon interacts with a charged particle in the magnetic field and is absorbed. There is a transition frequency ν_{sa} which corresponds to an optical depth of $\tau_\nu = 1$, at which point the spectrum turns. Figure 2.13 shows the synchrotron spectrum from a power law distribution of electrons. For optically thin synchrotron emission, the intensity is proportional to the emission function

$$S_\nu \propto \nu^{-\alpha} \quad (2.2.15)$$

whereas for optically thick synchrotron emission, the intensity is proportional to the source function

$$S_\nu = \frac{j_\nu}{\alpha_\nu} = \frac{P(\nu)}{4\pi\alpha_\nu} \propto \nu^{5/2} \quad (2.2.16)$$

which is a ratio of the emission coefficient to the absorption coefficient.

As seen in Fig. 2.13, the optically thick region occurs at low frequencies and dominates until the transition frequency ν_{sa} is reached, at which point the photons travel further than the range of the emission region before they are absorbed (Beckmann and Shrader 2012).

As previously mentioned in Sec. 2.1.3, the core of a radio jet is the brightest feature in a radio image and appears as a stationary feature located closest to the SMBH in the transition region between optically thick and optically thin at $\tau = 1$. According to Blandford & Königl (1979), the synchrotron emission in an expanding jet causes the core region at $\tau = 1$ to move upstream as the frequency of observation is increased. This effect is called the *core-shift* and is displayed in Fig. 2.14. The grey ellipses denote the observed position of the jet core, with darker colours corresponding to higher observation frequencies. The downstream components of a jet are optically thin and as such, their position are stable as a function of frequency (Böttcher et al. 2012). Due to this stability, the coreshift of a radio jet can be measured by aligning optically thin components over different observing frequencies (Sokolovsky et al. 2011).

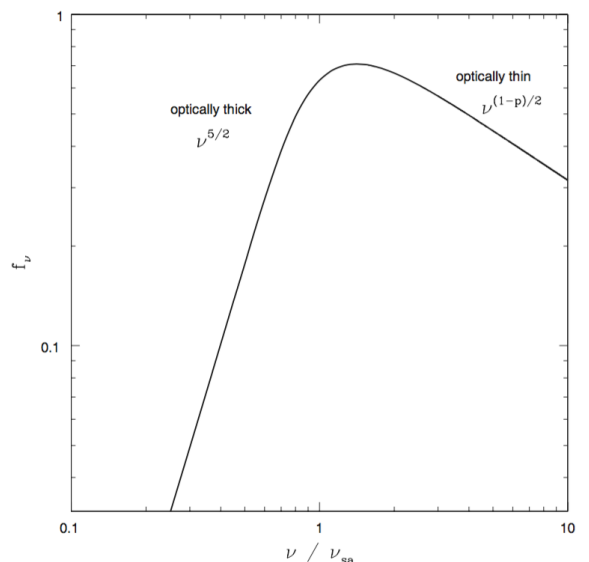


Figure 2.13.: The spectrum of synchrotron radiation for optically thick and optically thin media as a function of the self-absorption frequency ν_{sa} . At low frequencies, the optical thickness causes synchrotron self-absorption Image credit: Beckmann and Shrader (2012).

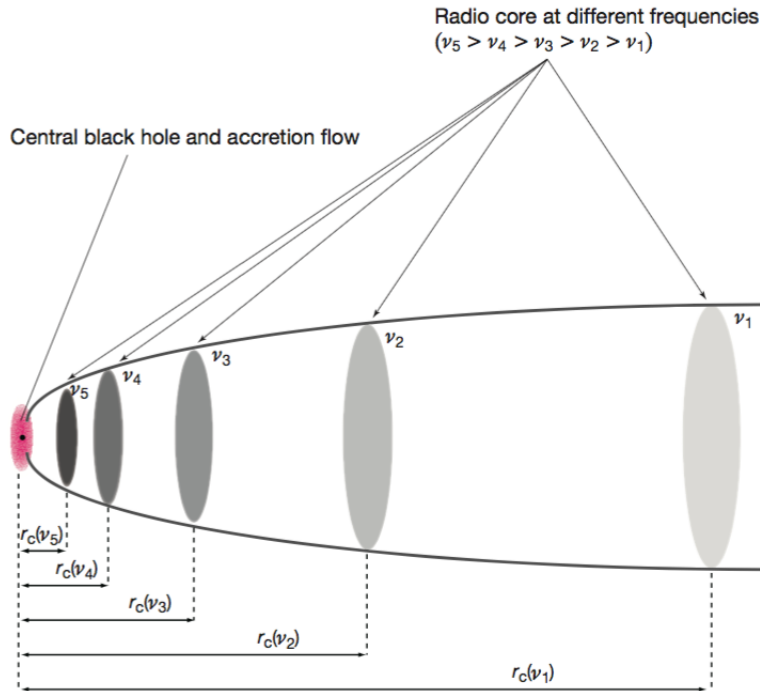


Figure 2.14.: Schematic diagram of the radio coreshift of a jet. The black dot represents the black hole surrounded by the (red ellipse) accretion disc. The observed positions of the cores of the jet are illustrated by grey ellipses, the position of which is dependent on the observing frequency. Image credit: Hada et al. (2011).

2.2.2. Inverse Compton Scattering

Compton scattering describes the process of an inelastic scattering in which a photon transfers energy to an electron. However, for a highly relativistic electron, energy can be transferred from the electron to a low frequency photon in a process called inverse Compton (IC) scattering (Rybicki & Lightman 1979). Unless cited otherwise, the explanation of this process follows Beckmann and Shrader (2012). Due to the fulfilment of the condition $h\nu \ll m_e c^2 / \gamma$, the Thomson scattering cross-section can be applied. Setting the observation frame as L and the rest frame of a relativistic electron as L' , the energy of the photon is much smaller than that of the electron $h\nu \ll mc^2$, such that the relativistic corrections in the Klein-Nishina formula are negligible (Rybicki & Lightman 1979). The energy of the photon in frame L is given by

$$h\nu' = \gamma h\nu \left(1 + \frac{v_e}{c} \cos \theta \right) \quad (2.2.17)$$

in which θ is the angle between the photon and the electron which travels with a velocity v_e in the observer's frame L . The angle appears smaller in the electron's frame L'

according to

$$\sin \theta' = \frac{\sin \theta}{\gamma \left(1 + \frac{v_e}{c} \cos \theta\right)} \quad (2.2.18)$$

Treating this as an elastic Thomson scattering, the photon's energy in the electron's frame is given by $E'_2 \simeq E'_1$, which translates back to the observation frame as

$$E_2 \simeq \gamma^2 E_1 \quad (2.2.19)$$

showing that the photon gains energy with the Lorentz factor, meaning that for highly relativistic electrons, a radio photon can be up-scattered to optical or X-ray energies. The energy gain of the photon is limited to $E_2 \leq E_1 + \gamma m_e c^2$ by the conservation of energy of the inverse Compton scattering in the observation frame. The maximum possible change in the frequency of the photon is then given by

$$\Delta \nu \leq \gamma m_e c^2 h^{-1} \quad (2.2.20)$$

The power of inverse Compton scattering is dependent on the density n_{ph} of photons which are available for scattering, meaning that the luminosity for the inverse Compton component is given by

$$L_{\text{IC}} \propto n_{\text{ph}} \gamma^2 E_1 \quad (2.2.21)$$

Considering the relativistic Doppler shift and the energy density of the photon field U_{ph} as given by

$$\frac{dE}{dt} = c \sigma_{\text{T}} U_{\text{ph}} \quad (2.2.22)$$

the luminosity is given by

$$L_{\text{IC}} = \frac{4}{3} \frac{v_e^2}{c} \sigma_{\text{T}} \gamma^2 U_{\text{ph}} \quad (2.2.23)$$

Following the same assumption of a power law distribution of electron energies as in Sec. 2.2.1 and assuming highly relativistic electrons, Eq. 2.2.23 can be integrated to yield the inverse Compton luminosity for the electron distribution

$$L_{\text{IC}} = \frac{4}{3} c \sigma_{\text{T}} U_{\text{ph}} C_{\gamma} \frac{\gamma_{\text{max}}^{3-p} - \gamma_{\text{min}}^{3-p}}{3-p} \quad (2.2.24)$$

in which γ_{min} and γ_{max} are the assumed minimum and maximum for the Lorentz factor of the electrons in the distribution, C is the normalisation, and p is the slope of the power law. In the case that $h\nu' \ll mc^2$ is not fulfilled in the electron's frame, the assumption of elastic scattering is no longer valid and the Thomson cross-section can no longer be applied. The previously neglected Klein-Nishina corrections must be considered for photons with high energies. This model depends on the photon energy and scattering angle and is described in detail in Blumenthal & Gould (1970). Within the inverse Compton regime with respect to the emission of jets, there are two possibilities for the

scattering to occur (Ghisellini et al. 1998). The first process is synchrotron self-Compton (SSC), which occurs when the seed photon is produced by the synchrotron emission. The photons are then further up-scattered by the electrons which are responsible for the synchrotron emission. In order for SSC to occur, the plasma must be optically thick. Photons which have already been up-scattered by IC processes remain part of the photon population and can therefore be scattered multiple times in an effect which strongly depends on the brightness of the source. Above a threshold brightness temperature T_{thresh} , the IC losses cool the electrons, leading to the inverse Compton catastrophe. Kellermann & Pauliny-Toth (1969) described the ratio between the inverse Compton and synchrotron radiation as

$$\frac{L_{\text{IC}}}{L_{\text{sync}}} = \left(\frac{T_{\text{B}}}{T_{\text{thresh}}} \right)^5 \left[1 + \left(\frac{T_{\text{B}}}{T_{\text{thresh}}} \right)^5 \right] \quad (2.2.25)$$

For $T_{\text{thresh}} \simeq 10^{12}$ K, inverse Compton processes will dominate the emissions as soon as $T_{\text{B}} > T_{\text{thresh}}$ with little to no synchrotron emission. A further limit to the brightness temperature by equipartition has been proposed by Readhead (1994). For a brightness temperature of 10^{11} K $\lesssim T_{\text{B}} \lesssim 10^{12}$ K, the ratio in Eq. 2.2.25 approaches unity, as the synchrotron losses and the IC losses are of the same order. This equipartition is stable over time scales of years, whereas at $T_{\text{B}} \sim 10^{12}$ K, the IC catastrophe would cause an object to lose most of its energy in X-rays over a time scale as short as a few days (Readhead 1994). The second process is known as external Compton (EC) scattering, in which the seed photons for the IC scattering are photons from external radiation regions. The production mechanism of γ -rays in a leptonic model depends on the location - inside the BLR, γ -rays are mostly produced by EC on UV photons, by EC on IR photons between the BLR and the torus, and by SSC or EC on CMB photons at further distances (Ghisellini & Tavecchio 2009; Costamante et al. 2018). The standard model of an SED of the majority of γ -ray detected FSRQs has been the EC process on BLR photons (Ghisellini et al. 1998). Costamante et al. (2018) noticed a problem with this model: the external photons which are used for the external Compton scattering processes become targets for γ - γ absorption and pair production. This could be a crucial insight to understanding the lack of γ -ray detections for some FSRQs.

2.2.3. Hadronic Processes

Until now, the processes described have been for purely leptonic models. Synchrotron radiation as described in Sec. 2.2.1 is also possible for protons, but since the power per unit frequency is inversely proportional to the mass of a particle as shown in Eq. 2.2.10, the power produced per particle by proton synchrotron radiation is $\sim 1/2000$ the amount produced by electron synchrotron radiation. As such, proton synchrotron radiation only significantly contributes to high-energy emissions if the proton population is large enough to account for the fractional output of power. If the proton popula-

tion is neither significant enough in proton synchrotron radiation nor accelerated in a strongly magnetised environment such that the threshold energy for $p\gamma$ pion production is reached, the high-energy radiation will be dominated by the leptonic emission processes described above (Böttcher 2010). However, if one or both of these criteria are fulfilled, such that the energy loss rate of the protons is equal that of the electrons, high-energy emissions in the form of synchrotron-supported pair cascades will be induced (Mannheim 1993). Sufficient acceleration to energies of $E_p^{\max} \gtrsim 10^{19}$ eV would require a magnetic field of several tens of Gauss (Böttcher 2010). According to Mücke & Protheroe (2000), the synchrotron radiation of primary protons and secondary muons and mesons must also be considered in such strong magnetic fields. The electromagnetic cascades will dominate the high-energy emissions, while the low-frequency synchrotron emission is still caused by primary leptons (Böttcher 2010). There is a variety of electromagnetic cascades caused by different decay processes: photons from π^0 -decay in the " π^0 cascade", electrons from the $\pi^\pm \rightarrow \mu^\pm \rightarrow e^\pm$ decay in the " π^\pm cascade", p -synchrotron photons in the " p -synchrotron cascade", and μ^- , π^- , and K -synchrotron photons in the " μ^\pm -synchrotron cascade" (Böttcher et al. 2012). The γ -ray spectra produced by π^0 -cascades and π^\pm -cascades are featureless, whereas those produced by p -synchrotron cascades and μ^\pm -synchrotron cascades feature a two-component γ -ray spectrum (Mücke & Protheroe 2001; Mücke et al. 2003).

2.2.4. γ - γ Pair Production

Pair production, the process in which γ -ray photons interact with each other and lower energy photons to produce an electron-positron pair, is the only relevant absorption process for γ -rays in FSRQs (Böttcher et al. 2012). γ - γ pair production or γ - γ annihilation is particularly relevant to the scope of this thesis with respect to the BLR. As mentioned in Sec. 2.2.2, the target photons for EC processes also absorb γ -rays from the EC processes. Additionally, γ -rays between 10 GeV and 1 TeV interact with infrared-ultraviolet photons and are subsequently attenuated by pair production (Liu et al. 2008). Liu & Bai (2006) studied the γ - γ attenuation optical depth of the gamma rays which interact with the BLR photons, considering four main parameters: the γ -ray emitting radius R_γ , the luminosity L_{BLR} of the BLR, the half thickness h of the BLR, and the ratio of the Thomson optical depth to the covering factor of the BLR $\tau_{\text{BLR}}/f_{\text{cov}}$.

Consider two photons of energy ϵ_1 and ϵ_2 , respectively. These photons interact under a collision angle $\theta = \cos^{-1} \mu$ and produce an electron positron pair, $\gamma + \gamma \rightarrow e^+ + e^-$, which, in the centre-of-momentum frame, have equal Lorentz factors and equal normalised velocities. The threshold condition on the energy ϵ_1 is given by

$$\epsilon_1 \geq \frac{2}{\epsilon_2(1 - \mu)} \quad (2.2.26)$$

which reduces to $\epsilon_{1,\text{thr}} = 1/\epsilon_2$ for a head-on collision with interaction angle $\mu = -1$. The

inverse process may also occur, in which an electron and positron annihilate, producing two γ -ray photons. The influence of this process on the γ -ray spectrum depends on the location of the absorbing radiation field. If this is located outside the emission region, γ - γ absorption can be described by an exponential absorption term compared to the intrinsic emission F_v^{int}

$$F_v^{\text{obs}}(\epsilon) = F_v^{\text{int}}(\epsilon)e^{\tau_{\gamma\gamma}(\epsilon)} \quad (2.2.27)$$

in which $\tau_{\gamma\gamma}$ is the opacity for γ - γ absorption of a γ -ray photon. If the absorption occurs within the emission region, the influence of the absorption on the spectrum is defined by the radiative transfer equation (Böttcher et al. 2012).

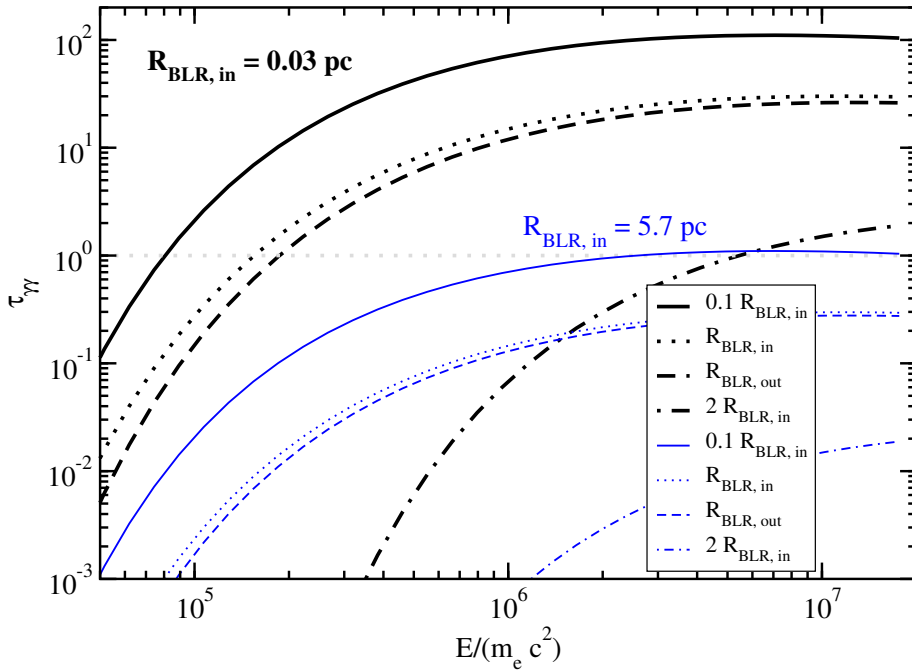


Figure 2.15.: γ - γ absorption due to photons from the BLR in the bright quasar 3C 279. The labels indicate the location of the γ -ray emission region. Image credit: Böttcher et al. (2009).

Figure 2.15 shows the γ - γ opacity of the BLR radiation field as a function of the photon energy ϵ and the location of the γ -ray emission site for the γ -ray bright quasar 3C 279. The luminosity of the accretion disc is given by $L_D = 2 \cdot 10^{45}$ erg/s, the radially averaged Thomson depth of the BLR is $\tau_{\text{BLR}} = 0.1$. The black lines denote a distance of the central engine to the inner edge of the BLR of $R_{\text{BLR},\text{in}} \sim 0.03$ pc. All parameters have been inferred from Pian et al. (2005). With the parameters set to these standard values, the plot shows that very high energy γ -rays which are produced inside the BLR are subject to extreme γ - γ absorption from the same photons which would be seed photons for Compton scattering in a purely leptonic model (Böttcher et al. 2009). The blue lines denote the value of $R_{\text{BLR},\text{in}} \sim 5.7$ pc as calculated by Böttcher et al. (2009), showing that γ -rays produced near the inner boundary of the BLR with energies up to several TeV

would not be affected by γ - γ absorption. This model implies, however, that absorption in the BLR field would correspond to a very high level of intrinsic γ -ray production, forcing strict requirements for jet parameters in the one-zone leptonic model.

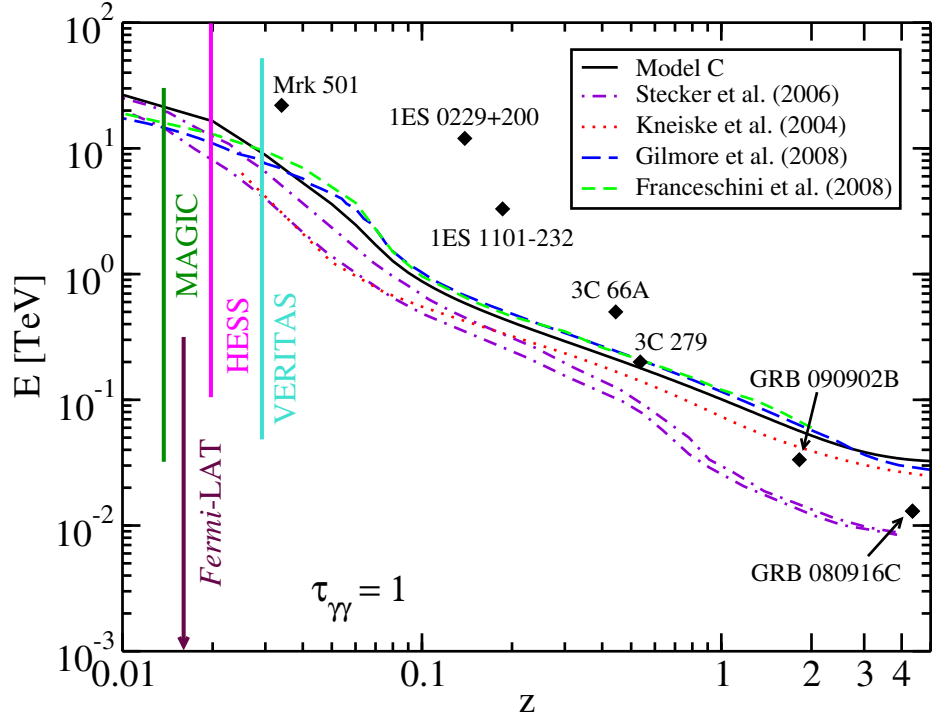


Figure 2.16.: $\tau_{\gamma\gamma} = 1$ for several models of the EBL as a function of redshift. Image credit: Finke et al. (2010).

As mentioned in Sec. 2.1.4, the absorption of γ -rays can also occur through interactions with the EBL. The EBL comprises infrared emissions from the dust of young galaxies and emissions from stars at infrared and optical energies. The spectrum of the EBL and consequently the γ - γ opacity for high-energy γ -rays are dependent on redshift, as shown in Fig. 2.16. For different models of the EBL, the energy at which the universe becomes optically thick to γ -rays, corresponding to $\tau_{\gamma\gamma} = 1$, is plotted as a function of redshift (Finke et al. 2010). This relation is known as the Fazio-Stecker relation (Fazio & Stecker 1970). The diamonds denote the maximum γ -ray photon energy bins from blazars observed with Cherenkov telescopes and γ -ray bursts observed with *Fermi*/LAT. Since the high-energy γ -rays of many blazars are above the boundary of $\tau_{\gamma\gamma} = 1$ for all models, it is clear that the γ -ray emissions suffer absorption by the EBL. At high redshifts, the highest energy photons from γ -ray bursts constrain the EBL (Finke et al. 2010).

2.3. Very Long Baseline Interferometry (VLBI)

Since Jansky's first observation of radio emissions from the Milky Way, radio astronomy has played an crucial role in observational astrophysics. In addition to its suitability in probing the cosmic microwave background, radio observations enable the investigation of not only thermal but also non-thermal phenomena, due to the long wavelengths. The Earth's atmosphere has so-called observing "windows", as shown in Fig. 2.3. The broadest window is at wavelengths corresponding to radio emissions, meaning that observations can be made from the Earth's surface without encountering atmospheric absorption (Burke & Graham-Smith 2010). Radio astronomy, particularly Very Long Baseline Interferometry (VLBI), enables the observation of the finer structures of astrophysical sources, especially the jets of AGN.

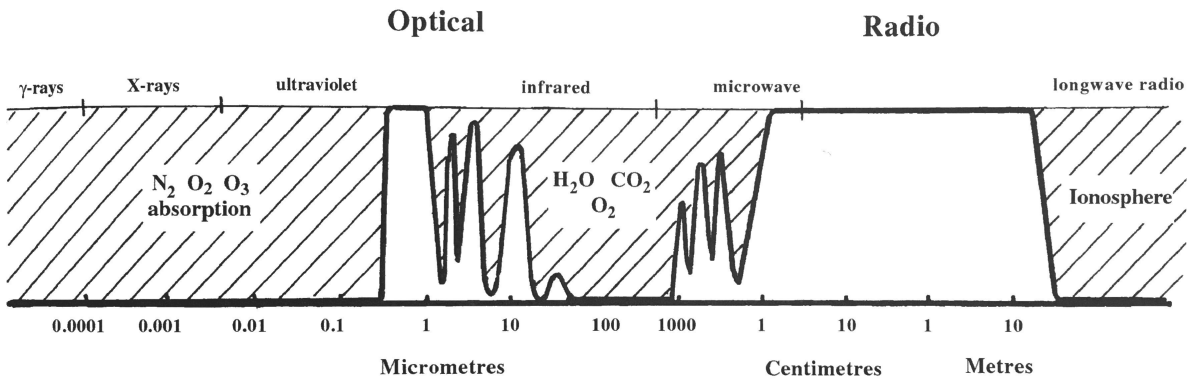


Figure 2.17.: The electromagnetic spectrum showing the wavelength ranges of the atmospheric "windows". Image credit: Burke & Graham-Smith (2010).

The Rayleigh criterion defines the angular resolution θ of a circular aperture with diameter D at wavelength λ as

$$\theta \approx 1.22 \frac{\lambda}{D}, \quad [\theta] = \text{rad} \quad (2.3.1)$$

which limits the size of the sources a radio telescope can resolve (Bass et al. 1995). The Effelsberg Radio Telescope is one of the largest steerable telescopes in the world, measuring an impressive 100 m in diameter. The minimum angular resolution for observations in the X-Band (corresponding to $\lambda \approx 3.5$ cm) would then be $\theta \approx 1.2$ arcmin, which is not sufficient to resolve jets on kiloparsec or even parsec scales, for which resolutions of arcseconds or smaller are required. In order to obtain such high resolution, VLBI is implemented, a technique in which receiving antennae all over the world are operated independently with no real-time connection to each other. VLBI utilises an array of interferometers, each comprising two radio telescopes, to observe the same object, producing resolutions much higher than could be achieved by any individual radio telescope (Thompson et al. 2004).

The aspects of VLBI which are relevant to the scope of this work will be discussed

in the following sections. Unless otherwise cited, this follows Burke & Graham-Smith (2010), which offers a detailed introduction to radio astronomy. For more in-depth discussions of synthesis and imaging in radio interferometry, please refer to Thompson et al. (2004) and Taylor et al. (1999).

2.3.1. The Two-Element Interferometer

The simplest form of a telescope array is a two-element interferometer, as pictured in Fig. 2.18. Two telescopes are connected by the baseline vector \mathbf{b} . The unit vector \mathbf{s} gives the direction of the observed radio source. The radio source is tracked by both antennae, one of which is defined as the reference antenna.

The signal arrives at the other antenna with a geometrical time delay of

$$\tau_g = \mathbf{b} \cdot \frac{\mathbf{s}}{c} \quad (2.3.2)$$

which can be adjusted by including an instrumental time delay τ_i . The instrumental time delay is set to $\tau_i = 0$ for the following discussion. The time-averaged product of the two amplitudes, one of which is delayed by time τ , is given by the cross-correlation

$$R_{xy}(\tau) = \langle x(t)y(t - \tau) \rangle \quad (2.3.3)$$

which has dimensions of power, leading to the alternative name of the cross-power product. In order to describe the output of an interferometer as opposed to the output of a single antenna, the cross-correlation $R_{xy}(\tau)$ can be Fourier transformed to give the cross-spectrum power density

$$S_{xy}(\nu) \equiv X(\nu)Y^*(\nu) \quad (2.3.4)$$

which is the product of the transform of $x(t)$ and the complex conjugate of the transform of $y(t)$. For monochromatic signals, the Fourier transform consists of a delta-function at the frequency ν and one with a phase-shift of $2\pi\nu\tau_g$. The product is also proportional to the effective antenna area $A(\mathbf{s})$, yielding

$$S_{xy}(\nu) = A(\mathbf{s})S \exp(i2\pi\nu\tau_g) = A(\mathbf{s})S \exp(i2\pi\mathbf{b}_\lambda \cdot \mathbf{s}) \quad (2.3.5)$$

in which S is the source flux density and $\mathbf{b}_\lambda = \frac{\mathbf{b}}{\lambda}$ is the dimensionless form of the baseline measured in wavelengths.

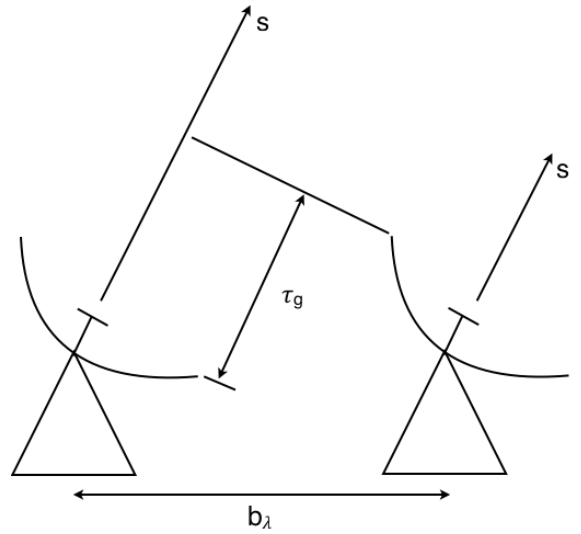


Figure 2.18.: Sketch of a two-element interferometer after Burke & Graham-Smith (2010).

Until now, the instrumental time delay has been set as $\tau_i = 0$. To describe an interferometer comprising two steerable telescopes directed at an arbitrary source position, one considers a source close to the reference position \mathbf{s}_0 defined by the position $\tau_g = \tau_i$. The reference position \mathbf{s}_0 is called the phase-tracking centre, and τ_i can be called the equalising time delay since it corrects the geometrical time delay τ_g . The direction to the source is then given by

$$\hat{\mathbf{s}} = \hat{\mathbf{s}}_0 + \sigma \quad (2.3.6)$$

in which σ is a vector normal to \mathbf{s}_0 .

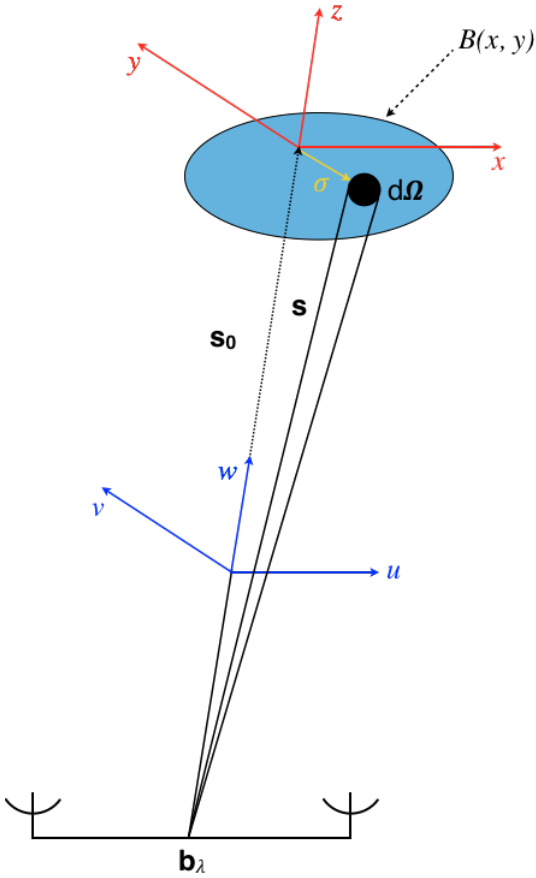


Figure 2.19.: Geometrical sketch of the two-element interferometer and the definition of the u, v - and x, y -planes. The interferometer is pointed at the element $d\Omega$ of the source's brightness distribution $B(x, y)$. This element is located at a distance σ from the phase tracking centre \mathbf{s}_0 . Figure after Burke & Graham-Smith (2010).

Figure 2.19 shows the geometrical relationship of the interferometer, the source, and the u, v -plane. The individual components illustrated in Fig. 2.19 will be explained in more detail in the following paragraphs. Considering this interferometer, only the small differential due to the displacement σ must be considered, since τ_i is an exact correction for the geometrical time delay. In order to apply these fundamentals to radio astronomy, the finite bandwidth of the receiver and finite size of a source must replace the assumptions of a point source with single frequency emissions. First addressing the receiver bandwidth, all interferometers have a finite bandwidth \mathcal{B} . The radio spectrum across the band can be approximated as flat, since the radio spectrum of a continuum source changes slowly with frequency and the bandwidth of an interferometer only covers a small fraction, an assumption which simplifies the analysis. Due to the finite bandwidth \mathcal{B} , the angular range over which fringes appear is decreased. The angle of the vector pointing to the source determines the nature of the interference patterns of the signals. If the source is normal to the baseline, constructive interference will appear at all frequencies.

However, if the source's location is not normal to the baseline, the phase change of the fringe pattern will be different at different frequencies across the band. These interfer-

ences lead to the confinement of the fringe patterns to a narrow beam, also called the delay beam, the centre of which can be moved by changing the delay of one of the telescopes. The effects of the delay beam can be calculated by considering the cross-product power

$$P_{xy} = \int_{-\infty}^{\infty} S_{xy}(\nu, \mathbf{s})G(\nu)d\nu \quad (2.3.7)$$

in which $G(\nu)$ is the square bandpass of the receiver which is centred at ν_0 and zero elsewhere and the single frequency response from Eq. 2.3.5 can be summed over the bandpass since the signal at any frequency is independent of that at other frequencies. Although an interferometer does not have an exactly square bandpass, this approximation is sufficient in most cases. Assuming that the effective area of the receivers and the flux are constant across the bandpass and including the aforementioned instrumental time delay, the cross-spectrum power density becomes

$$S_{xy}(\mathbf{s}) = A(\nu_0, \mathbf{s})S(\nu_0)\text{sinc}[\mathcal{B}(\tau_g - \tau_i)] \exp[-2\pi\nu_0(\tau_g - \tau_i)] \quad (2.3.8)$$

The delay beam $\text{sinc}[\mathcal{B}(\tau_g - \tau_i)]$ reduces the fringe oscillations $\exp(-2\pi\nu_0\tau_g)$.

In order to account for the finite size of a source, consider the geometrical sketch in Fig. 2.19. The interferometer receives radiation from an extended radio source with brightness $B_\nu(\mathbf{s})$ which subtends a solid angle $d\Omega$ in the direction \mathbf{s} . The phase tracking centre is then defined as \mathbf{s}_0 and, in following with Eq. 2.3.6, σ is the vector from \mathbf{s}_0 to the element of the source from which the signal is received. Replacing the source flux with B_{ν_0} and the effective area with the relative antenna area \mathcal{A} then yields a cross-spectral density which is integrated over the entire radio source. Assuming that the source size is small in comparison to the response pattern of the delay beam, bandwidth effects can be neglected. As long as the width of the field of view fulfils the requirement $\theta \ll (\nu/\mathcal{B})(1/b_\lambda)$, the centre frequency of the bandpass $\nu = \nu_0$ can be set as the defining frequency. This yields

$$S_{xy}(\mathbf{s}_0) = \int \mathcal{A}(\sigma)B_\nu(\sigma) \exp\{i2\pi[\mathbf{b}_\lambda \cdot (\mathbf{s}_0 + \sigma) - \nu\tau_i]\}d\Omega \quad (2.3.9)$$

In order to translate the above considerations to VLBI interferometry, consider an array consisting of many two-element interferometers, each pair with the baseline vector \mathbf{b}_{ij} of the i -th and j -th element of the array. Defining the baseline in terms of wavelength $\mathbf{b}_{ij,\lambda} \equiv \mathbf{b}_{ij}/\lambda$ and setting the instrumental delay such that it exactly corrects for the tracking-centre delay yields the complex visibility

$$V_{ij} \equiv S_{xy}(\mathbf{b}_{ij} \cdot \mathbf{s}_0) = \nu\tau_i \quad (2.3.10)$$

which subsequently yields the fundamental equation for a practical interferometer of which the amplitude and phase are the main observables

$$V_{ij} = \int \mathcal{A}(\sigma) B_\nu(\sigma) \exp(i2\pi \mathbf{b}_{ij,\lambda} \cdot \sigma) d\Omega \quad (2.3.11)$$

The natural coordinate system for the correlator response is the u, v -plane which is perpendicular to the source direction \mathbf{s}_0 and parallel to the offset vector σ . The coordinates of this system are (u, v, w) and \mathbf{s}_0 defines the w -direction. The coordinate distances are expressed in wavelengths, and the complex visibility is then given by

$$V_{ij}(\mathbf{s}_0, u, v) = \int \mathcal{A}(l, m) B_\nu(l, m) \exp[i2\pi(ul + vm + wn)] d\Omega \quad (2.3.12)$$

in which l, m, n are the direction cosines of the unit vector \mathbf{s} and since the source direction \mathbf{s}_0 is perpendicular to the u, v -plane, $w = 0$. Expressing the solid angle in terms of (l, m) gives

$$d\Omega = \frac{dldm}{\sqrt{1 - l^2 - m^2}} \quad (2.3.13)$$

the denominator of which will never become imaginary due to the angles l and m always being close to 90° . This then yields

$$V_{ij} = \int_{4\pi} \mathcal{A}(l, m) B_\nu(l, m) \exp[i2\pi(ul + vm)] \frac{dldm}{\sqrt{1 - l^2 - m^2}} \quad (2.3.14)$$

from which it can be seen that $V(u, v)$ is the Fourier transform of a modified source brightness

$$V_{ij} \xleftrightarrow{\text{FT}} \frac{\mathcal{A}(l, m) B_\nu(l, m)}{\sqrt{1 - l^2 - m^2}} \quad (2.3.15)$$

Generally, the offset angle σ is small, meaning that in most cases, x is parallel to u . Because the source is usually small compared to the size of the beam, the variation of gain with angle can also be neglected, assuming that the telescopes are pointed accurately. Using a small-angle approximation, Eq. 2.3.14 then becomes

$$V(u, v) \approx \mathcal{A} \int B(x, y) \exp[i2\pi(ux + vy)] dx dy \quad (2.3.16)$$

The complex visibility function received by the antennae in the u, v -plane is the Fourier transform of the brightness distribution. The geometry of this is shown in Fig. 2.19. The coordinates (l, m) of the source plane become the celestial angular coordinates (x, y) for small angles. The Fourier transform is measured in the u, v -plane. The observation from one interferometer in which the amplitude and phase of the complex visibility are measured will only give one value in the source's brightness distribution. By making many

observations with several interferometers, the complete Fourier transform of the source brightness distribution, $b(u, v) = V(u, v)$ can be obtained, which can subsequently be inverted to produce the source's complete brightness distribution $B(l, m)$.

2.3.2. Array Interferometry

When considering the array interferometry of VLBI, the phase instability of radio interferometers plays a significant role in observations. Jennison (1958) demonstrated that in an array of three antennae as shown in Fig. 2.20, the approximate sum over the visibility phases around the closed loop of baselines, called the closure phase, is not affected by antenna dependent errors. As such, the closure relations for phases and amplitudes can be used to self-calibrate the observations. The following section follows Cornwell (1989) and Cornwell & Fomalont (1999), unless otherwise cited.

Consider an array of N telescopes in which θ_{ij} is the phase between the i -th and j -th telescope. Each telescope has a phase error ϕ , as illustrated in Fig. 2.20. Ignoring additive noise, the coherence phase θ_{ij} which is measured between elements i and j of the array is related to the true coherence phase $\hat{\theta}_{ij}$ by

$$\theta_{ij} = \hat{\theta}_{ij} + \phi_i - \phi_j \quad (2.3.17)$$

The sum around the loop is given by

$$\theta_{ijk} = \theta_{ij} + \theta_{jk} + \theta_{ki} \quad (2.3.18)$$

and the true sum is given by

$$\hat{\theta}_{ijk} = \hat{\theta}_{ij} + \hat{\theta}_{jk} + \hat{\theta}_{ki} \quad (2.3.19)$$

which shows that

$$\begin{aligned} \theta_{ijk} &= \hat{\theta}_{ij} + \phi_i - \phi_j + \hat{\theta}_{jk} + \phi_j - \phi_k + \hat{\theta}_{ki} + \phi_k - \phi_i \\ &= \hat{\theta}_{ij} + \hat{\theta}_{jk} + \hat{\theta}_{ki} = \hat{\theta}_{ijk} \end{aligned} \quad (2.3.20)$$

and as such, the observed sum and the true sum are equal, proving that this sum is independent of antenna-based phase errors. Considering an array comprising N telescopes, there is a total of $\frac{N(N-1)}{2}$ independent fringe phases with a total of $\frac{(N-1)(N-2)}{2}$ closure phases. The closure phase consequently contains information about the structure of an observed object and can constrain the structural determination of an object in the

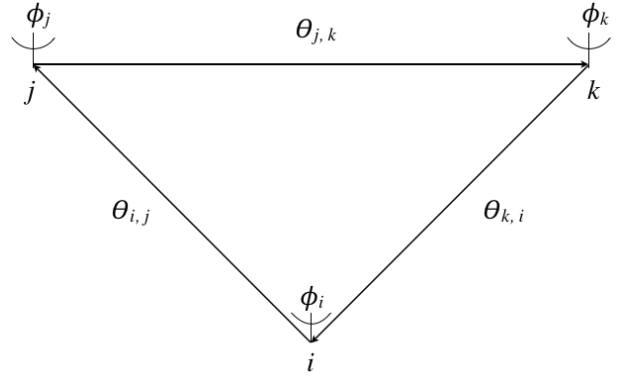


Figure 2.20.: A loop of three radio antennae, i, j, k each with a phase error ϕ and phase θ between each pair of telescopes. Figure after Cornwell (1989).

eventuality that the coherence phase is corrupted. Closure phases from different configurations of antennae can be used to calculate phase corrections for individual antennae relative to the phase correction of a chosen antenna (Burke & Graham-Smith 2010). Similarly, the closure relation for the fringe amplitudes of a group of four telescopes is given by

$$A_{ijkl}(t) = \frac{|\hat{V}_{ij}||\hat{V}_{kl}|}{|\hat{V}_{ik}||\hat{V}_{jl}|} \quad (2.3.21)$$

This closure amplitude is independent of atmospheric and telescope specific effects, and again ignoring noise, the measured and true closure amplitudes are equal. The larger an array is, the smaller the difference in independent fringe phases (amplitudes) and the corresponding closure phases (amplitudes), meaning that more information from the fringe phases (amplitudes) is contained in the closure phases (amplitudes). The fractions f_ϕ and f_A of recovered phase and amplitude information dependent on the number of telescopes N are given by

$$f_\phi = \frac{N-2}{N} \quad (2.3.22)$$

$$f_A = \frac{N-3}{N-1} \quad (2.3.23)$$

According to its definition, the closure phase is not affected by a change to a single antenna. As such, the constraints of the closure phase can be used in imaging by considering the antenna phases ϕ_i as degrees of freedom when estimating the brightness of the sky. The advantages of this approach are that the closure phases do not have to be calculated or stored, and that receiver noise can be treated by selecting antenna phases which reduce the mean square discrepancy between the observed coherences $\hat{A}_{i,j}$ and the coherences predicted by a model $A_{i,j}$ which are modified by the antenna phases with

$$S = \sum_{ij} |A_{i,j} - e^{i\phi_i} e^{-i\phi_j} \hat{A}_{i,j}|^2 w_{i,j} \quad (2.3.24)$$

in which the weighting factor $w_{i,j}$ can be set to favour baselines with good signal-to-noise ratios or to exclude those which are known to be problematic. More will be explained about the function of weighting in imaging in Sec. 3.2.1. Once the antenna phases have been calculated by self-calibration, they can be used to calibrate nearby objects. In order to ensure that there are more constraints than degrees of freedom, assumptions about the object being imaged must be made, or the array being used must have a certain degree of redundancy of measurement. Closure quantities alone are not sufficient to produce an image, but by using them in iterative algorithms, hybrid images can be produced. Such an iterative process using the closure phase was developed by Readhead & Wilkinson (1978) to produce images consistent with the closure quantities. A typical self-calibration algorithm is shown in Fig. 2.21.

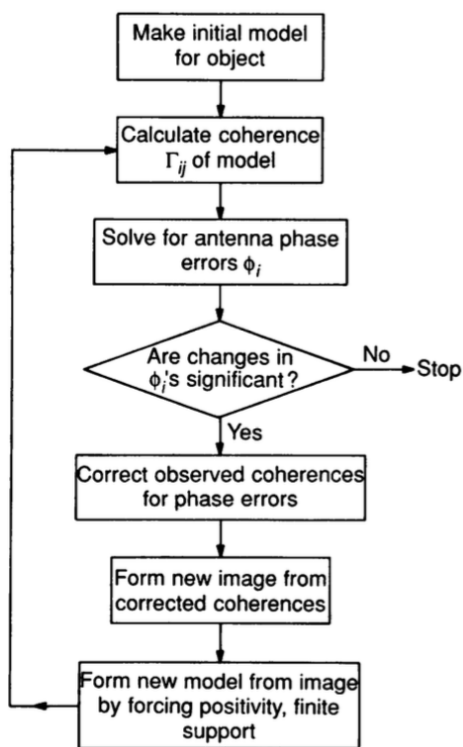


Figure 2.21.: A flow chart for a typical algorithm for the self-calibration algorithm. The coherence Γ in the second step is referred to as A in the text. Image credit: Cornwell (1989).

Ryle & Neville (1962) demonstrated that the coverage of a single baseline can be improved by exploiting the rotation of the Earth during longer observations lasting twelve hours each. Individual telescopes tracking the source produce arcs on the u, v -plane in a technique initially called Earth-rotation synthesis, now known as aperture synthesis. The effect of aperture synthesis on the MERLIN interferometer can be seen in Fig. 2.22. For different declination angles δ , different patterns in the u, v -plane coverage are visible, with horizontal lines corresponding to the celestial equator $\delta = 0^\circ$ and ellipses which approach circularity as the declination angle approaches the zenith. An array of N telescopes produces a set of $\frac{N(N-1)}{2}$ fringe visibilities $V_{ij}(u_k, v_k)$ which provides an approximation of the Fourier transform of the source's brightness. A complete sampling $V(u, v)$ of the u, v -plane would be the Fourier transform of the brightness distribution $B(x, y)$. A well-defined Fourier transform becomes easier to construct with increasing N . The limitations of the sampling of the Fourier-transform plane are expressed as a spectral sensitivity function $W(u, v)$. This is also sometimes called the spatial transfer function because under observation from an array, a point source $\delta(x, y)$ appears as a spread pattern which is the Fourier transform of $W(u, v)$. This spread

A similar algorithm was developed by Readhead et al. (1980) using the closure amplitudes rather than the phases. One of the most significant problems posed by the construction of hybrid images with iterative algorithms such as those developed by Readhead & Wilkinson (1978) is that it is difficult to correctly treat noise due to its additive nature in the vector visibility rather than in the amplitude or phase, leading to a complicated Rice distribution in the phase. Additionally, it is difficult to select closure quantities for an array with a large number of elements because the closure quantities will have varying signal-to-noise ratios (SNRs) for a source which displays significant structure. Finally, the calibration effects in radio imaging are antenna dependent rather than baseline dependent, meaning that it is simpler to apply other constraints to a telescope-based approach.

As mentioned in the previous section, the observation of one interferometer yields one value in the source's brightness distribution.

pattern, labelled $b_0(x, y)$, is generally called the synthesis beam or the "dirty" beam. The deconvolution of the dirty image is further discussed in Sec. 3.2.1. According to Thompson et al. (2004), the measured visibility can be expressed as a function of the spectral sensitivity and the weighting factor as

$$V_{\text{measured}}(u, v) = w(u, v)W(u, v)V(u, v) \quad (2.3.25)$$

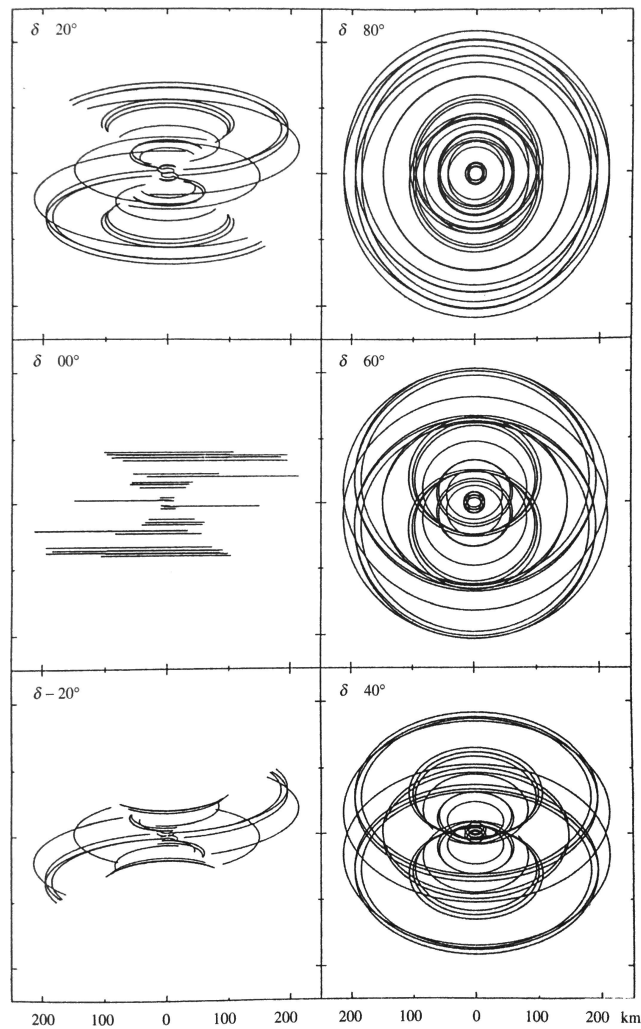


Figure 2.22.: Using six telescopes observing over an 8-hour tracking period, the u, v -plane coverage of the MERLIN interferometer is shown for six different declinations δ . Image credit: Burke & Graham-Smith (2010).

3. Observations and Data Reduction

3.1. The TANAMI Programme

TANAMI (Tracking Active galactic Nuclei with Austral Milliarcsecond Interferometry) is a multiwavelength programme which combines high-resolution radio imaging and spectral monitoring with higher frequency observations at IR, optical/UV, X-ray and γ -ray energies to monitor AGN jets of the southern hemisphere, targeting AGN south of -30° declination. Unless otherwise cited, the information in this section is from the TANAMI papers by Ojha et al. (2010) and Kadler et al. (2015).



Figure 3.1.: The telescopes of the TANAMI array. TANAMI combines the Australian Long Baseline Array with telescopes in South Africa, Antarctica and Chile to take snapshot observations at 8.4 and 22 GHz. Image credit: TANAMI/Kadler M./Wilms J.

TANAMI observes at two frequencies, 8.4 and 22.3 GHz (X- and K-Band), in order to calculate spectral indices of jets and to measure the time evolution of observed sources. Snapshot observations are typically made with an integration time of approximately

60 minutes per frequency observed. The sources are observed at intervals of approximately four months with typical angular resolutions of $1.5 - 4$ by $0.5 - 1.0$ mas (Ojha et al. 2010). These observations are made using the Parkes, Mopra, ATCA, Hobart, and Ceduna telescopes which comprise Australia’s Long Baseline Array (LBA). The LBA is supplemented by an antenna at Haartebeesthoek in South Africa and the 34 m and 70 m telescopes operated by the NASA Deep Space Network in Tidbinbilla in the Australian Capital Territory, completing the southern VLBI network. Further extending the TANAMI array through a programme approved by the International VLBI Service, the aforementioned telescopes are further augmented by the GARS antenna at O’Higgins, Antarctica, and TIGO, which was moved in 2015 from Concepción, Chile to La Plata, Argentina and was subsequently renamed the Argentinian-German Geodetic Observatory (AGCO) (Müller et al. 2018).

Table 3.1.: The TANAMI Array

Telescope	Diameter [m]	Location
Parkes	64	Parkes, New South Wales, Australia
ATCA	5×22	Narrabri, New South Wales, Australia
Mopra	22	Coonabarabran, New South Wales, Australia
Hobart	26	Mt. Pleasant, Tasmania, Australia
Ceduna	30	Ceduna, South Australia
DSS43 ¹	70	Tidbinbilla, ACT, Australia
DSS34 & DSS45 ¹	34	Tidbinbilla, ACT, Australia
Hartebeesthoek ²	26	Hartebeesthoek, South Africa
O’Higgins ³	9	O’Higgins, Antarctica
TIGO ³	6	Concepción, Chile
Warkworth	12	Auckland, New Zealand
Katherine	12	Northern Territory, Australia
Yarragadee	12	Western Australia
ASKAP	36×12	Murchison, Western Australia

Note: Table according to Ojha et al. (2010) and Rösch (2016).

¹ Operated by the Deep Space Network of the National Aeronautics and Space Administration.

² Unavailable between September 2008 and September 2010. ³ Operated by the German Bundesamt für Kartographie und Geodäsie.

Further increasing image fidelity and resolution, the array is expanded by AuScope telescopes in Yarragadee, Western Australia and Katherine, Northern Territory, a telescope in Warkworth, New Zealand, and an ASKAP antenna in Western Australia. Additional observations from a radio flux-density monitoring programme with ATCA (Australia Telescope Compact Array) at frequencies of 4.8, 8.6, 17/19, 38 and 40 GHz and the single University of Tasmania telescope at Ceduna at 6.7 GHz complete the TANAMI

array. Figure 3.1 displays the radio telescopes of the TANAMI array, with the exception of the more recent additions of ASKAP, Katherine, and Yarragadee. A full list of participating antennae is presented in Table 3.1. In this work, one epoch refers to one 24 hour observation and only observations at 8.4 GHz were analysed.

Originally a radio programme focused on high-resolution VLBI observations and flux-density monitoring, TANAMI has vastly expanded to encompass observations across the multiwavelength spectrum. The Ceduna Hobart Interferometer (CHI) comprising the radio telescopes in Hobart, Tasmania and Ceduna, South Australia, is able to measure the flux densities of flaring objects within thirty minutes of a triggering event from *Fermi* (Blanchard et al. 2012). Over the past few years, several telescopes have contributed to the NIR/optical part of the spectrum, including the Rapid Eye Mount (REM) telescope, Gemini South, the Telescopio Nazionale Galileo (TNG), the Nordic Optic Telescope, and Atom. The Cerro Tololo Inter-American Observatory (CTIO) contributes data from the SARA consortium telescope and public data from the SMARTS programme. Many TANAMI sources have been monitored in the X-ray range by a combination of several guest observations on the satellites RXTE, XMM-*Newton*, INTEGRAL, Suzaku and *Swift*, the last of which also provides additional optical/UV observing time. Cooperation with the *Fermi* Large Area Telescope (LAT) in the γ -ray range and the neutrino telescopes of the ANTARES collaboration complete TANAMI's multiwavelength observation of the southern sky.

In the scope of this work, observations with the TANAMI array of the four FSRQs between 2008 and 2013 were analysed. The individual configuration of telescopes which provided data for each observation of each source are listed in Sec. 4.

3.2. Data Reduction with DIFMAP

In order to be able to analyse VLBI data, initial phase and amplitude calibrations must be performed by the National Radio Astronomy Observatory's Astronomical Image Processing System (AIPS) software (Greisen 2003). For the TANAMI programme, all data is calibrated by Dr. Roopesh Ojha of NASA's Goddard Space Flight Centre. Further information about fringe fitting and VLBI data reduction with AIPS can be found Cotton (1995) and Diamond (1995) respectively. Unless otherwise cited, the information in this section follows the DIFMAP Cookbook (Taylor 1997).

3.2.1. Imaging

Once calibrated by AIPS and subsequently saved as a UVFITS file, the data are inspected and edited by DIFMAP, a computer program which uses an iterative mapping technique called "difference mapping" to produce an image (Shepherd 1997). Before the data reduction can begin, the data are read into DIFMAP. The polarisation is selected and the following parameters must be set: the data are averaged with `uvaverage` in order to

speed up calculations and provide a statistical error for the data bins. TANAMI data are conventionally averaged over 32 seconds. The u,v weighting and the appropriate weighting of the visibilities by errors are set with `uvweight`. The default uniform weighting weights the data inversely to the number of visibilities in each bin. In this work, natural weighting was selected for all sources. Natural weighting is equal weighting of all data points, providing higher sensitivity than uniform weighting. Before the first iteration of an image can be created, the size of the image and the cell sizes must be defined using the command `mapsize`. DIFMAP is only able to properly deconvolve the inner quarter of the image, so the map size should be at least twice the size of the source. For TANAMI data, the conventional settings are 1024 pixels with the mas cell size per pixel set to 0.175 mas.

The next step in the imaging process is to inspect the data for "bad" data points, outliers, and other anomalies which could cause complications or difficulties in the production of a final image. DIFMAP includes several plots which are crucial in gaining an accurate first impression of the data. `tplot` displays a data point for every time interval for which an observation with a telescope yielded data. Gaps in this plot indicate gaps in the observation coverage and can be indicative of the resulting image quality. `uvplot` displays the u,v coverage of the observation. `radplot` shows the amplitude as a function of the u,v radius. Outliers are easily spotted and can be flagged as such. In addition to removing outliers from within `radplot`, `vplot` provides a more detailed view of all data and can be used to interactively execute baseline-based edits for individual intermediate frequencies (IFs). Both `radplot` and `vplot` also display the model once it has been developed, allowing a direct comparison of the model to the data points.

Once these preliminary steps have been carried out, the `clean` algorithm can be implemented in the process of "difference mapping". The `clean` algorithm, developed by Högbom (1974), is an iterative procedure which, considering a radio source as several point sources, identifies the locations and strengths of these point sources, building a model to deconvolve the so-called "dirty" image (Cornwell et al. 1999). For a more detailed analysis of the `clean` algorithm, please refer to Högbom (1974) and Cornwell et al. (1999). Through repetitions of the `clean` algorithm and self-calibrations with the latest model, a final deconvolved "`clean`" image can be obtained. The difference mapping procedure used to produce the images in this thesis starts by placing a window around the emission peak of the dirty image, limiting the area in which the `clean` algorithm is executed. An initial point-source starting model is applied and the dirty image is cleaned and self-calibrated. The command `gscale` is executed at this point to self calibrate to determine the overall telescope amplitude corrections. The developing model is subtracted from the data with each iteration, producing a progressively "cleaner" residual map with δ components corresponding to the subtracted flux density. As the difference mapping procedure continues, further windows are set around the brightest areas in the residual map, expanding the area in which the clean components are placed. Loops can be defined so that DIFMAP automatically executes `clean` and `selfcal` for a given number of iterations. This should be repeated until the cleaned flux no longer increases. When a

satisfactory model has been developed, the data are self amplitude- and phase-calibrated using the command `selfcal true`, `true` in decreasing time intervals of 180, 60, 20, 5, 1, and 0 minutes, corresponding to the decreasing closure phases. Between each iteration of this self-calibration, the previously mentioned `radplot` and `vplot` should be checked regularly to compare the developing model to the data and to remove any outliers. In addition, `corplot` displays a correction plot to track what changes have been made to the data. The data should be saved after every self-calibration so that each stage of the cleaning can be accessed independently. After the final self-calibration, all clean windows are deleted and a deep clean is executed with a large number of iterations, followed by a phase self-calibration and a final deep clean. This produces the final "clean" image, the self-calibrated data, and a model. The model can then be compared to the raw, not self-calibrated data. The sources studied in this work have between four and eight observation epochs each. In multi-epoch imaging, once the general structure of a jet has been identified, the clean windows from the penultimate step of one epoch can be loaded in DIFMAP and applied to the "dirty" image of the next epoch. Multi-epoch imaging also allows for comparison between epochs to identify potential artificially imaged features which may appear as a result of erroneously placed clean windows or noise.

3.2.2. Model Fitting

After a final "clean" image has been produced following the aforementioned procedure, a model consisting of a small number of elliptical Gaussian components can be built to describe the data. A comprehensive description of model fitting can be found in Pearson (1995) and a detailed explanation of least-squares fit methods can be found in Bevington and Robinson (2003). DIFMAP uses an iterative process of self-calibration and model-fitting to produce a model which is the sum of the elliptical Gaussian components (Pearson 1995). In order to create the model, the δ components from the `clean` process must be removed. This can be done all at once by clearing the current model with the command `clrmod`; alternatively, the δ components can be removed individually in the area of interest of the clean image, starting with the core and moving outwards to model fit the jet components. The models in this work were developed according to the latter method in order to facilitate an accurate placement of Gaussian components suitable for describing the clean image. A new Gaussian component is defined in the image in a few simple steps. Typing `n` within the image environment prepares for the definition of a new component. The first click of the mouse defines the centre of the component, the second sets the length of the major axis, and the third sets the length of the minor axis. Typing `n` a second time concludes the definition of a new Gaussian component. Eliminating the third click produces a circular component, the size of which is defined by the major axis. The given flux of the Gaussian component is the flux of the pixel at the centre of the ellipse. The command `modelfit` followed by a chosen number executes that number of iterations of model fitting, which displays the parameters of the model fit components and the reduced χ^2 after each iteration. The model is improved by continued iterations

of `modelfit` until the reduced χ^2 no longer decreases. A low value close to 1 is ideal for the reduced χ^2 . At this point, the parameters of the model can be viewed and edited with the command `edmod`. Within the editor, all remaining δ components can be removed and the size of individual Gaussian components can be fixed to meet the resolution limit, avoiding physically impossible values of the brightness temperature. This process is described in further detail in Sec. 4. In addition, it is sometimes necessary to create an image by restoring the clean image with a different beam size than that estimated by DIFMAP (Taylor 1997). The command `restore` allows the user to input the major and minor axes in milliarcseconds and to determine the angle in degrees from North to East. In the case that there is a large difference in beam sizes between different epochs, it can be helpful to restore the images with the same beam size in order to more easily compare features across epochs.

3.3. Further Data Analysis

In order to produce time-evolution images and plots of component characteristics as a function of time, S-Lang scripts were written using functions of the Interactive Spectral Imaging Software (ISIS) (Houck & DeNicola 2000). The clean, model-fitted data were read by ISIS to execute the calculations and produce all plots in this work.

4. Results

The sources which are studied in the scope of this thesis are four TANAMI detected flat-spectrum radio quasars. TANAMI began by studying the bright compact radio sources of the southern sky. In order to supplement the TANAMI observations, a collaboration was initiated with the *Fermi*/LAT satellite in 2008 to search for γ -ray radiation from AGN. Many of the sources in the TANAMI catalogue were then detected by *Fermi*/LAT at γ -ray energies. The FSRQs included in the scope of this thesis are of particular interest because despite displaying strong radio emissions, to date, none have been included in the *Fermi* catalogue. However, it is possible that all four FSRQs emit weak γ -ray emissions over long time scales which are below the detection threshold of *Fermi*/LAT and are only detectable during strong γ -ray flares. Light curves for the γ -ray emissions have been produced for all sources in the sample and will be analysed in Sec. 5. The results in the following sections are presented for each source individually. The images and plots for the sample of flat-spectrum radio quasars have all been produced following the procedure outlined in Sec. 3.2.

The kinematics plots for each source display the fitted Gaussian components as circles or ellipses (fitted according to Sec. 3.2.2) plotted over the clean maps (produced according to Sec. 3.2.1). The first contour is set at three times the root-mean-square noise level with the following contours increasing logarithmically by a factor of two. The vertical distance between the images corresponds to the time elapsed between observations, the dates of which are printed alongside each image within the kinematics plots. The dashed lines represent the proper motion of the components. The x -axis, defined as the relative right ascension in milliarcseconds, is set in all kinematics figures in this work such that the core of the jet lies at 0 mas. Individual `clean` maps which have been produced following the procedure outlined in Sec. 3.2.1 for each epoch of each source can be found in Appendix A, facilitating comparison of the fine structures of the jets between epochs.

The following sections are structured as follows. A brief introduction is provided for each source, including known parameters and results from relevant publications with focus on the characteristics and findings which are relevant to understanding the γ -ray quiescence of the sources in the sample. The results of the imaging process are stated and explained, followed by a description of the self-consistent Gaussian model which has been constructed. Results for the brightness temperature, flux density, and kinematics which have been inferred from the model are presented and described comprehensively for each component.

4.1. PKS 0438–436

PKS 0438–436 is a flat-spectrum radio quasar with a redshift of $z = 2.856$ (Punsly et al. 2018). After having been included in several larger surveys, this blazar was identified as having the highest known radio luminosity (Morton et al. 1978) and the second strongest synchrotron core (Punsly 1995). What makes this object even more interesting is that it is unremarkable in luminosity in the optical band between 4000 and 7000 Å, while still emitting a total radio luminosity equivalent to the optical output of 10^{13} Suns (Morton et al. 1978). The combination of strong core-dominated radio emission and high optical polarisation indicates relativistic beaming towards us (Wilkes et al. 1992). Additionally, following observations by *Einstein* and *ROSAT*, Wilkes et al. (1992) identified PKS 0438–436 as the highest luminosity quasar with significant absorption of soft X-rays. The unexpected absorption of $\sim 1 \cdot 10^{22} \text{ cm}^{-2}$ is most likely intrinsic to PKS 0438–436. On 11 December 2016, *Fermi*/LAT observed strong γ -ray emission from a source positionally consistent with PKS 0438–436 (Cheung 2016). Previously, PKS 0438–436 had no γ -ray detections from EGRET, AGILE, or *Fermi*/LAT. A more detailed discussion of the γ -ray flare will follow in Sec. 5.2.1 and the complete analysis can be found in Punsly et al. (2018).

4.1.1. Imaging

Eight observations of TANAMI data between 7 February 2008 and 14 March 2013 were analysed for PKS 0438–436. The telescope configuration for each observation is listed in Table 4.1. Only the telescopes which provided data for this source are included in the table. Figure 4.1 shows the time evolution of PKS 0438–436 over the whole observation

Table 4.1.: Observation Epochs for PKS 0438–436

Date ¹ YYYY-MM-DD	Name	Telescopes ²
2008-02-07	V252C	CD, HO, MO, AT, PA
2008-06-09	V252F	HART, CD, HO, MO, AT, PA
2008-11-27	V252I	DSS43, TC, OH, CD, HO, MO, AT, PA
2009-12-13	V252O	CD, TC, PA, MP, HO, AT
2010-07-24	V252S	DSS43, TC, PA, MP, HO, CD, AT
2011-01-01	V252X	WW, TC, PA, MP, HO, HH, DSS43, CD, AT
2011-11-13	V252AB	WW, DSS43, PA, MP, HO, HH, CD, AT
2013-03-14	V252AIJ	WW, PA, KE, HO, CD, AK

Note: ¹ date of observation ² The following abbreviations are used for the telescopes: AT: ATCA, AK: ASKAP, CD: Ceduna, HH: Hartebeesthoek, HO: Hobart, KE: Katherine, MP: Mopra, OH: O’Higgins, PA: Parkes, DSS43: Tidbinbilla 70 m, TC: TIGO, WW: Warkworth.

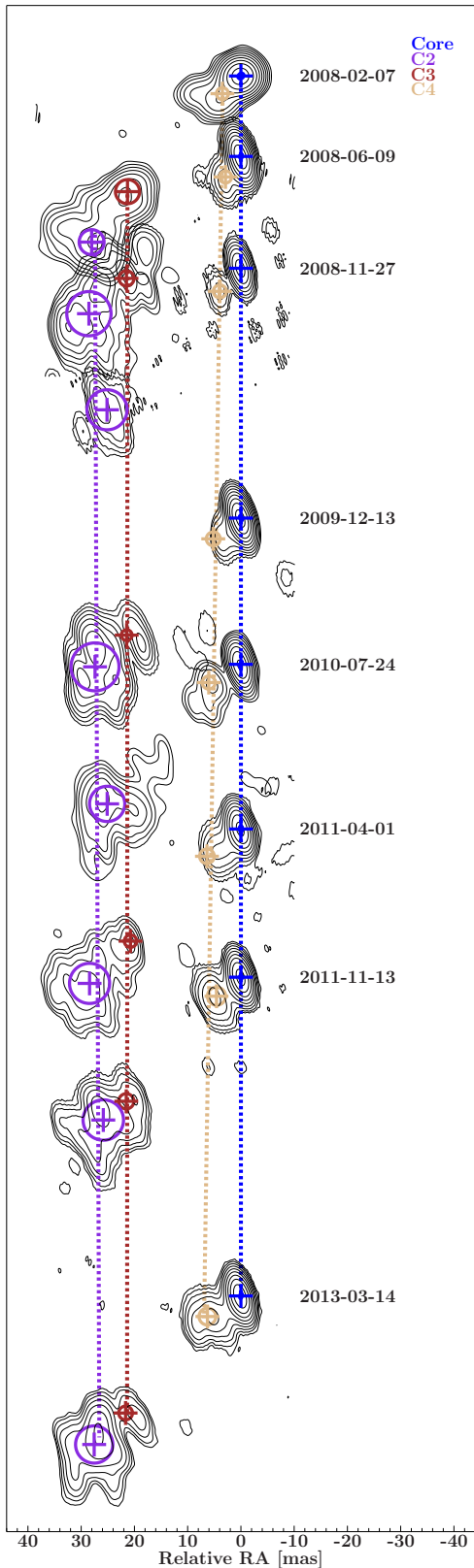


Figure 4.1.: Time evolution of PKS 0438–436.

period. The images comprising Fig. 4.1 have been restored according to the procedure described in Sec. 3.2.2 to be able to better compare the images from individual epochs with each other. The original individual images are included in Appendix A.1. The major and minor axes for the restoring beam were measured from the epoch with the second largest beam size, V252F, in order to minimise the loss of the finer structures of the jet which would have occurred had the images been restored with the even larger beam of epoch V252C. All epochs show a core-dominated structure with a compact jet extending in a south-easterly direction from the core. The jet is divided into two separate substructures, the inner region closest to the core and a larger, slightly weaker outer structure. Both the core region and the outer region are each composed of two smaller substructures.

4.1.2. Model Fitting

The components are identified according to their time of origin, from the outside of the jet to the core, with the component nearest the core as the newest component labelled with the highest number. This convention is consistently applied to all following sources. The structure of PKS 0438–436 has been model fitted with Gaussian components in accordance with the procedure outlined in Sec. 3.2.2, comprising the core and three further components. The core and C4 model the internal structure while C2 and C3 model the outer structure, with the exception of the epochs V252I and V252S, in which the outer structure is modelled by C2 alone. Referring to epoch V252C in Fig. 4.1, the

Table 4.2.: Parameters of Gaussian models of PKS 0438–436.

Epoch Code	S	R	Θ	a	b	P.A.	T_B	ID
Date	[Jy]	[mas]	[$^\circ$]	[mas]	[mas]	[$^\circ$]	[K]	
	0.892	0.05	134.9	1.2	0.9	−49.1	$5.25 \cdot 10^{10}$	Core
V252C	0.069	4.86	133.7	2.2	2.2	−171.5	$9.40 \cdot 10^8$	C4
2008-02-07	0.211	30.50	135.6	4.5	4.5	−50.7	$7.00 \cdot 10^8$	C3
	0.225	42.03	138.1	4.7	4.7	150.3	$6.98 \cdot 10^8$	C2
	0.884	0.03	74.5	0.8	0.5	−6.0	$1.54 \cdot 10^{11}$	Core
V252F	0.071	4.84	142.7	2.3**	2.3**	−171.5	$9.33 \cdot 10^{8\dagger}$	C4
2008-06-09	0.095	31.4 3	137.0	2.8	2.8	−50.7	$8.03 \cdot 10^8$	C3
	0.349	41.1 0	136.0	8.3	8.3	150.3	$3.42 \cdot 10^8$	C2
	0.636	0.03	48.6	7.7	0.2*	−2.0	$3.09 \cdot 10^{11\dagger}$	Core
V252I	0.067	5.87	137.4	2.4**	2.4**	−68.2	$7.64 \cdot 10^{8\dagger}$	C4
2008-11-27	0.324	36.6 0	136.6	7.5	7.5	−87.1	$3.86 \cdot 10^8$	C2
	0.582	0.17	17.4	0.9	0.4	18.8	$9.85 \cdot 10^{10}$	Core
V252O	0.031	6.45	125.6	2.6**	2.6**	−171.5	$3.14 \cdot 10^{8\dagger}$	C4
2009-12-13	0.063	30.65	135.5	2.0	2.0	−50.7	$1.04 \cdot 10^9$	C3
	0.400	39.07	135.4	9.0	9.0	150.3	$3.33 \cdot 10^8$	C2
	0.474	0.23	−23.1	1.1	0.2*	−19.9	$1.36 \cdot 10^{11}$	Core
V252S	0.061	6.77	118.4	2.4	2.4	128.4	$6.94 \cdot 10^8$	C4
2010-07-24	0.303	36.11	136.1	6.6	6.6	167.7	$4.67 \cdot 10^8$	C2
	0.594	0.04	−154.5	1.2	0.6	0.6	$5.82 \cdot 10^{10}$	Core
V252X	0.066	8.19	129.1	2.7	2.7	−171.5	$5.94 \cdot 10^8$	C4
2011-01-01	0.059	29.59	135.6	2.3	2.3	−50.7	$7.43 \cdot 10^8$	C3
	0.315	40.6 4	135.7	7.5	7.5	150.3	$3.75 \cdot 10^8$	C2
	0.498	0.05	153.5	0.8	0.5	−3.7	$8.78 \cdot 10^{10}$	Core
V252 AB	0.126	5.86	128.2	3.4	3.4	−171.5	$7.38 \cdot 10^8$	C4
2011-11-13	0.057	31.80	137.3	2.9	2.9	−50.7	$4.68 \cdot 10^8$	C3
	0.342	37.31	136.1	7.6	7.6	150.3	$4.01 \cdot 10^8$	C2
	0.530	0.03	−175.5	0.9	0.4	−9.5	$9.12 \cdot 10^{10}$	Core
V252AIJ	0.138	7.39	121.8	3.2	3.2	−171.5	$9.35 \cdot 10^8$	C4
2013-03-13	0.065	30.89	135.5	2.6	2.6	−50.7	$6.62 \cdot 10^8$	C3
	0.319	39.25	135.4	7.0	7.0	150.3	$4.40 \cdot 10^8$	C2

Note: S is flux density; R and Θ are the coordinates of the component in which R is the distance of the component to the designated phase centre and Θ is the angle in degrees from north to east. a and b are the major and minor axes of the components, respectively. P.A. is the position angle of the major axis of the component in degrees from north to east. T_B is the brightness temperature. ID is the identification of the component. * upper limit. ** size according to linear fit of all epochs.

† lower limit.

innermost component C4 is located at a radial distance of 4.68 mas from the core in a south-easterly direction. There is a fairly large gap between the inner and outer jet structure, with components C3 and C2 approximately 30.50 mas and 42.03 mas from the core respectively, both in a south-easterly direction. The model fitting parameters for each component over all epochs are presented in Table 4.2. A resolution limit was calculated for each component in each epoch according to Kovalev et al. (2005). The minimum resolvable size θ_{lim} of a Gaussian component fitted to naturally weighted VLBI data is given by

$$\theta_{\text{lim}} = b_{\psi} \sqrt{\frac{4 \ln 2}{\pi} \ln \left(\frac{\text{SNR}}{\text{SNR} - 1} \right)} \quad (4.1.1)$$

in which b_{ψ} is the half-power beam size measured along an arbitrary position angle ψ and the signal-to-noise ratio is given by $\text{SNR} = \frac{S_{\text{comp}}}{\sigma_{\text{comp}}}$. The values in Table 4.2 which are marked with a * are components which were unresolved according to Eq. 4.1.1 and have been increased to the calculated value of the resolution limit. The values marked ** have been further adjusted: the resolution limit θ_{lim} was met, but the size of C4 in epochs V252F, V252I, and V252O was still much smaller than in all other epochs. Therefore, the sizes were increased to the value corresponding to the linear fit of the size of C4 from all other epochs. These adjustments also affect the brightness temperature - setting an upper limit θ_{lim} to the size of the component then gives a lower limit to the brightness temperature, which is inversely proportional to the major and minor axes of the component, as shown by Eq. 2.1.7. A model fit component smaller than the resolution limit as set by Eq. 4.1.1 would show an improbably high brightness temperature. The values of T_{B} which are given as lower limits are marked with a † in Table 4.2.

4.1.3. Brightness Temperature

The brightness temperature of each component is plotted as a function of time in Fig. 4.2. Over the first three epochs, the brightness temperature of the core increases before dipping back down in epoch V252O and then varying slightly around approximately 10^{11} K. Components C2 and C4 both also display somewhat lower brightness temperatures in epoch V252O, contrary to the behaviour of C3, which displays its highest brightness temperature in this epoch. The peak brightness temperature $T_{\text{B}} = 3.09 \cdot 10^{11}$ K is displayed by the core in epoch V252I. This value, while considerably higher than that of other epochs, is still within the inverse Compton limit of 10^{12} K, previously explained in Sec. 2.2.2. There are no unexpected extraordinarily large spikes or dips, the presence of which would be a strong indication of an error in the model fit components, either in size, location, or both.

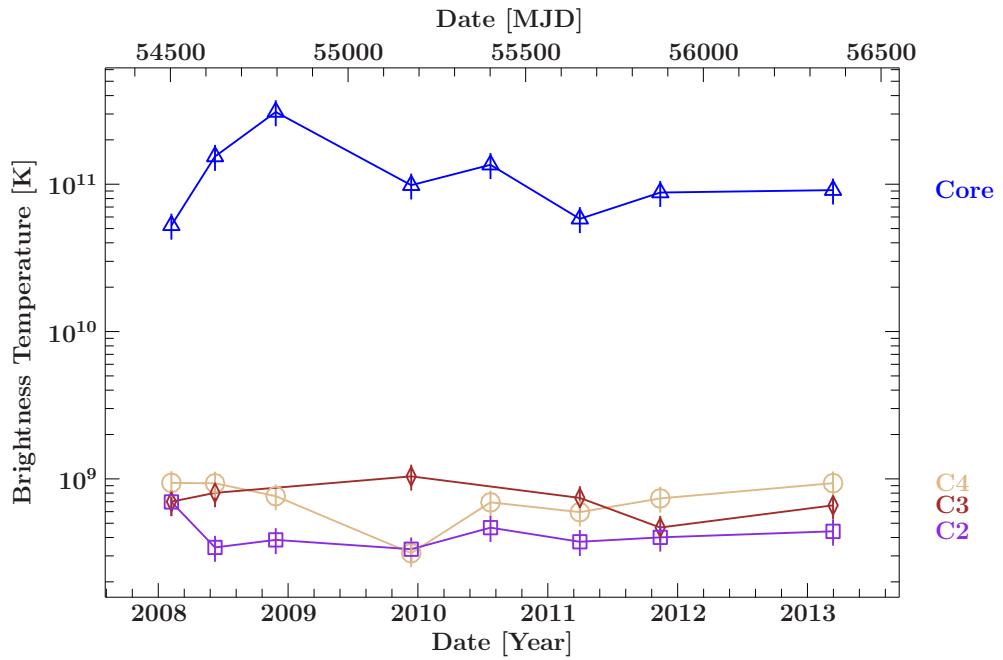


Figure 4.2.: Brightness temperature of the jet components of PKS 0438–436 plotted as a function of time. The error bars correspond to an estimated relative error of 20% from calibration and imaging errors according to Ojha et al. (2010).

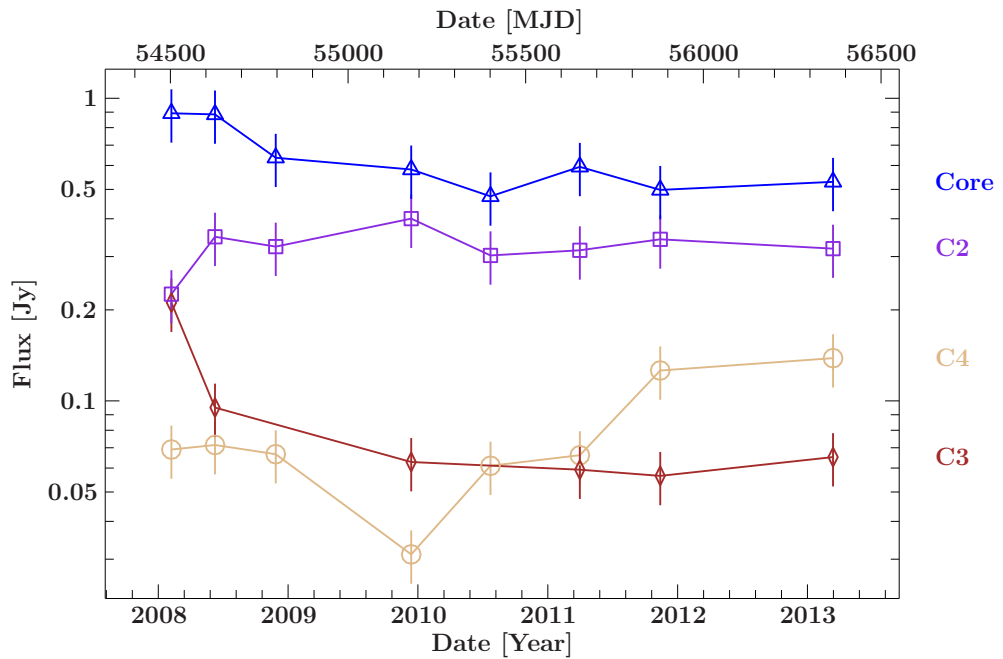


Figure 4.3.: Flux densities of the jet components of PKS 0438–436 plotted as a function of time. The error bars correspond to an estimated relative error of 20% from calibration and imaging errors according to Ojha et al. (2010).

4.1.4. Flux Density

Figure 4.3 displays the flux densities in Jansky of the individual jet components of PKS 0438–436 as a function of time. Theoretically, a decrease in flux is expected with time, as the components move further away from the core of the jet. This trend is followed by the outermost components C2 and C3, once again in contrast to the behaviour of C4, the flux of which increases over time. The flux density of C4 is weaker in epoch V2520 than in the preceding and succeeding epochs. This difference is slightly exaggerated by the logarithmic scale of the y -axis. Possible reasons for this will be discussed in Sec. 5.2.1.

4.1.5. Kinematics

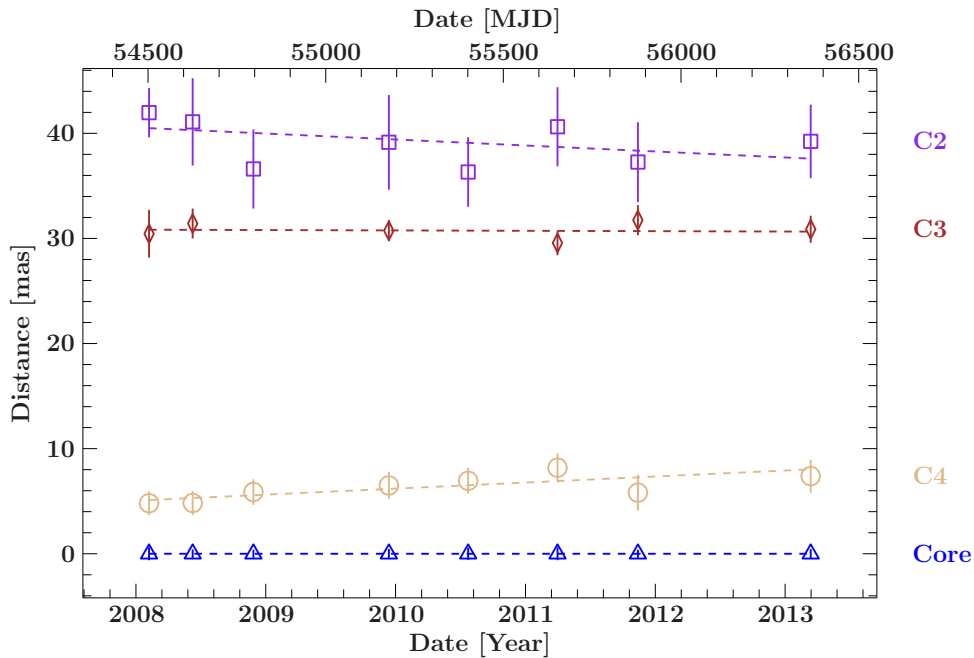


Figure 4.4.: Distance of the jet components of PKS 0438–436 relative to the position of the core component plotted as a function of time. The gradients of the dashed lines correspond to the speed of the components calculated according to the radial distance of the component from the core. The error bars correspond to the semi-major axis of the respective jet component.

Figure 4.4 shows the relative distance of the jet components from the core as a function of time. The slopes of the dashed lines correspond to the speed of the components and the error bars have been estimated from the semi-major axis of the jet component. The speed has been calculated by linear regression of the radial distance of the components from the core component over time. These values are presented in Table 4.3, the proper motion μ in units of mas/yr and β_{app} in terms of the speed of light c . Components

C2 and C3 have negative speeds, indicating motion towards the core, while C4 has a positive speed, indicating motion away from the core component. At first glance, all three components exhibit superluminal motion, with C2 and C4 displaying astoundingly fast speeds. The speeds of all components become much less remarkable when one considers the rather large errors.

Table 4.3.: Apparent speed of the jet components of PKS 0438–436 relative to the core.

Component	μ [mas/yr]	β_{app} [c]
C2	-0.570 ± 0.449	-56.100 ± 44.120
C3	-0.035 ± 0.220	-3.421 ± 21.649
C4	0.576 ± 0.178	56.624 ± 17.538

4.2. PKS 1257–326

The flat-spectrum radio and X-ray quasar PKS 1257–326 is located at $z = 1.256$ (Perlman et al. 1998). After having been included both radio and X-ray surveys, PKS 1257–326 was studied extensively by Bignall et al. (2003), who investigated the rapid radio intraday variability (IDV) of this source. With flux density variations of up to 40% on time scales as short as 45 minutes, Bignall et al. (2003) identified PKS 1257–326 as one of the fastest three IDV sources to date. Further investigations of the time delays of PKS 1257–326 by Bignall et al. (2006) confirmed the mechanism causing this rapid variability as interstellar scintillation. Building on this foundational data on extreme radio scintillation, Walker et al. (2017) theorised that this phenomenon is caused by interactions with the radially elongated plasma structures around hot stars in the solar neighbourhood. The source of the scattering material, which must be located at line-of-sight distances $\ll 1$ kpc from us, was identified as the star Alhakim. Woods (2017) questioned this theory, indicating a disparity in the parallels drawn by Walker et al. (2017) between the radio scintillation patterns of PKS 1257–326 and those of the Helix Nebula, the globular cometary structure of which was the basis for the inferred similarities between the Helix and the star Alhakim.

4.2.1. Imaging

Eight observations of TANAMI data between 7 February 2008 and 14 June 2013 were analysed for PKS 1257–326. The telescope configuration for each observation is listed in Table 4.4. Only the telescopes which provided data for this source are included in the table.

Table 4.4.: Observation Epochs for PKS 1257–326

Date ¹ YYYY-MM-DD	Name	Telescopes ²
2008-02-07	V252C	HART, CD, HO, MO, AT, PA
2008-06-09	V252F	HART, CD, HO, MO, AT, PA
2008-11-27	V252I	DSS43, TC, OH, CD, HO, MO, AT, PA
2009-09-05	V252N	DSS43, PA, MP, HO, CD
2010-05-07	V252R	DSS43, TC, PA, MP, HO, CD, AT
2011-08-13	V252AA	YG, PA, MP, KE, HO, AT
2012-09-15	V252AE	PA, HO, AT
2013-06-14	V252AK	WW, DSS34, PA, MO, HO, HH, CD, AT

Note: ¹ date of observation ² The following abbreviations are used for the telescopes: AT: ATCA, AK: ASKAP, CD: Ceduna, HH: Hartebeesthoek, HO: Hobart, KE: Katherine, MP: Mopra, OH: O’Higgins, PA: Parkes, DSS34 & DSS43: Tidbinbilla (34 & 70 m), TC: TIGO, WW: Warkworth, YG: Yarragadee.

Figure 4.5 shows the time evolution of PKS 1257–326 over the observation period. All epochs show a core-dominated structure with a compact jet in a north-westerly direction. There is a clear discrepancy in angular resolution between epochs, with especially poor resolution in epoch V252AE. During this observation, only the three telescopes listed in Table 4.4 for this epoch sporadically provided data, producing a snapshot observation. Due to the low volume of data, the image for this epoch cannot be self calibrated according to the standard imaging procedure outlined in Sec. 3.2.1. The image for epoch V252AE is only phase calibrated, not amplitude calibrated, eliminating the steps `selfcal true` and `gscale` for these calibrations from the imaging process. The morphology of PKS 1257–326 comprises two substructures, the core and inner region and an outer structure at approximately -8 mas. The inner region of the core is sometimes resolved as two smaller substructures next to each other, as in epochs V252C, V252F, V252I, V252R, and V252AK. Adequate resolution was not achieved in the other epochs, in which one central region is visible. The images from epochs V252N and V252AA display a defined outer component, in contrast to the stretched core visible in epoch V252AE.

4.2.2. Model Fitting

The structure of PKS 1257–326 has been model fitted with Gaussian components in accordance with Sec. 3.2.2, comprising the core and, depending on the epoch, one or two outer components, with the exception of epoch V252AE. The snapshot observation can only be modelled with one component for the core of the jet, leading to a decreased significance in kinematic analysis for this particular epoch. Referring to epoch V252C,

component C3 is located at a radial distance of approximately 2.85 mas in a north-westerly direction from the core. There is a separation between the inner structure and the outer structure modelled by C2, which in epoch V252C lies at a radial distance of 9.65 mas from the core in a north-westerly direction. Due to the large beam size in epoch V252N, the jet can only be modelled with C2 in addition to the core. The large beam size does not allow for the identification of any finer structure within the jet. The model fitting parameters for each component over all epochs are presented in Table 4.5. A resolution limit was calculated for each component in each epoch according to Kovalev et al. (2005) (refer to Sec. 4.1 for a detailed explanation). As for PKS 0438–436, the values marked * in Table 4.5 have been increased to the resolution limit θ_{lim} , yielding a lower limit for the brightness temperature T_{B} , indicated in Table 4.5 with a †.

4.2.3. Brightness Temperature

The values of the brightness temperature of each component are plotted against time in Fig. 4.6. Over the course of the eight observations, the brightness temperature of the core fluctuates fairly significantly, ranging from $7.40 \cdot 10^9$ K in epoch V252AA to a maximum value of $1.84 \cdot 10^{11}$ K in the final observation, V252AK. The brightness temperature of all components remains within the inverse Compton limit of 10^{12} K, previously explained in Sec. 2.2.2. Component C3 displays a sudden drop in brightness temperature in epoch V252R before increasing in the final epoch, V252AK. It is difficult to draw

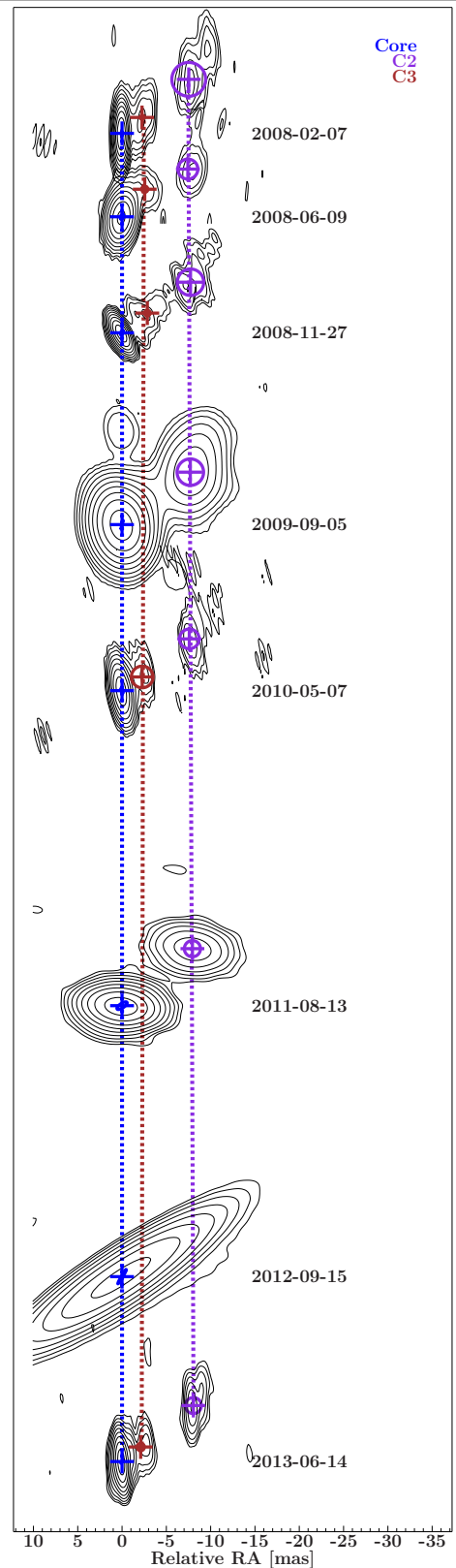


Figure 4.5.: Time evolution of PKS 1257–326.

conclusions regarding the behaviour of this component due to its absence in the models for the epochs immediately before and after this unexpected minimum. There are no unexpected extraordinarily large spikes or dips, the presence of which would be a strong indication of an error in the model fit components, either in size, location, or both.

Table 4.5.: Parameters of Gaussian models of PKS 1257–326.

Epoch Code	S	R	Θ	a	b	P.A.	T_B	ID
Date	[Jy]	[mas]	[$^\circ$]	[mas]	[mas]	[$^\circ$]	[K]	
V252C	0.141	0.05	178.1	0.3	0.2	−11.5	$1.14 \cdot 10^{11}$	Core
2008-02-07	0.010	2.85	−52.4	0.4	0.4	−83.1	$2.23 \cdot 10^9$	C3
	0.018	9.65	−51.3	3.8	3.8	130.7	$4.87 \cdot 10^7$	C2
V252F	0.154	0.01	−120.2	0.6	0.3	−39.9	$2.28 \cdot 10^{10}$	Core
2008-06-09	0.006	3.97	−38.3	0.7*	0.7*	108.4	$9.03 \cdot 10^{8\dagger}$	C3
	0.016	9.60	−53.7	3.0	3.0	130.1	$7.26 \cdot 10^7$	C2
V252I	0.142	0.02	−163.8	0.5	0.3	−22.0	$4.07 \cdot 10^{10}$	Core
2008-11-27	0.006	3.60	−52.4	0.6	0.6	110.3	$5.93 \cdot 10^8$	C3
	0.016	9.60	−53.7	3.0	3.0	130.1	$7.26 \cdot 10^7$	C2
V252N	0.141	0.11	156.7	1.0	0.4*	−11.6	$1.28 \cdot 10^{11\dagger}$	Core
2009-09-05	0.018	9.62	−52.8	3.0	3.0	132.9	$8.00 \cdot 10^7$	C2
	0.098	0.04	−175.2	0.5	0.2*	15.8	$3.35 \cdot 10^{10\dagger}$	Core
V252R	0.004	2.73	−56.5	2.4*	2.4*	110.3	$2.55 \cdot 10^{7\dagger}$	C3
2010-05-07	0.011	9.55	−52.6	2.2	2.2	130.1	$9.22 \cdot 10^7$	C2
	0.128	0.04	−163.4	1.3	0.5	−56.2	$7.40 \cdot 10^9$	Core
V252AA	0.022	100.2	−51.2	1.8	1.8	170.6	$2.50 \cdot 10^8$	C2
2011-08-13	0.152	0.03	−65.5	1.9	0.2	−30.3	$1.73 \cdot 10^{10}$	Core
	0.116	0.05	−178.0	0.5	0.05	−34.3	$1.84 \cdot 10^{11}$	Core
V252AK	0.007	2.63	−53.0	0.8	0.8	−76.1	$4.05 \cdot 10^8$	C3
2013-06-14	0.014	10.19	−52.1	1.8	1.8	−77.6	$1.70 \cdot 10^8$	C2

Note: S is flux density; R and Θ are the coordinates of the component in which R is the distance of the component to the designated phase centre and Θ is the angle in degrees from north to east. a and b are the major and minor axes of the components, respectively. P.A. is the position angle of the major axis of the component in degrees from north to east. T_B is the brightness temperature. ID is the identification of the component. * upper limit. † lower limit.

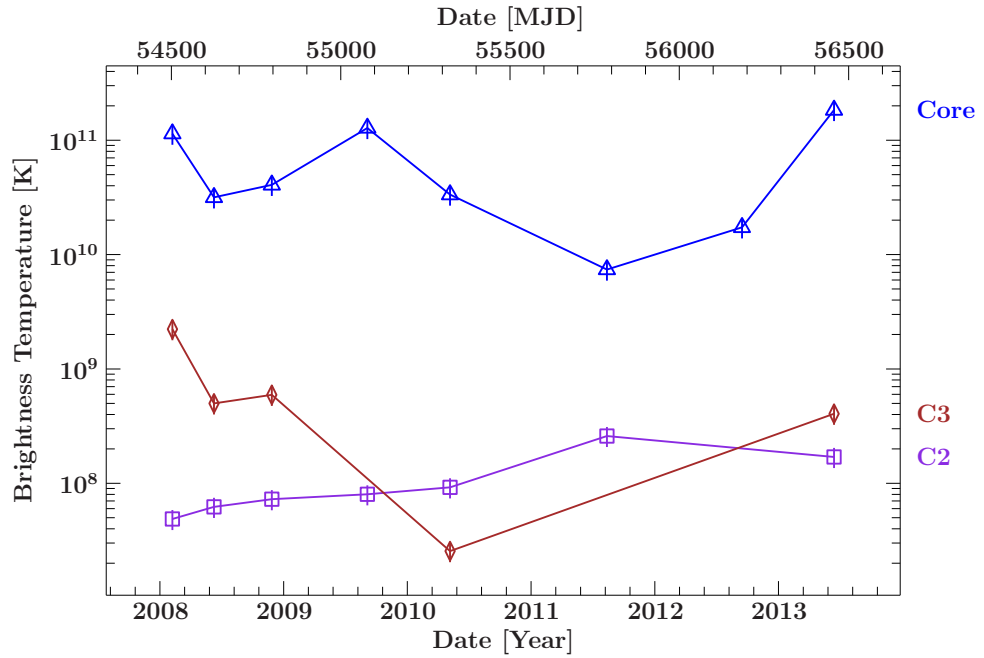


Figure 4.6.: Brightness temperature of the jet components of PKS 1257–326 plotted as a function of time. The error bars correspond to an estimated relative error of 20% from calibration and imaging errors according to Ojha et al. (2010).

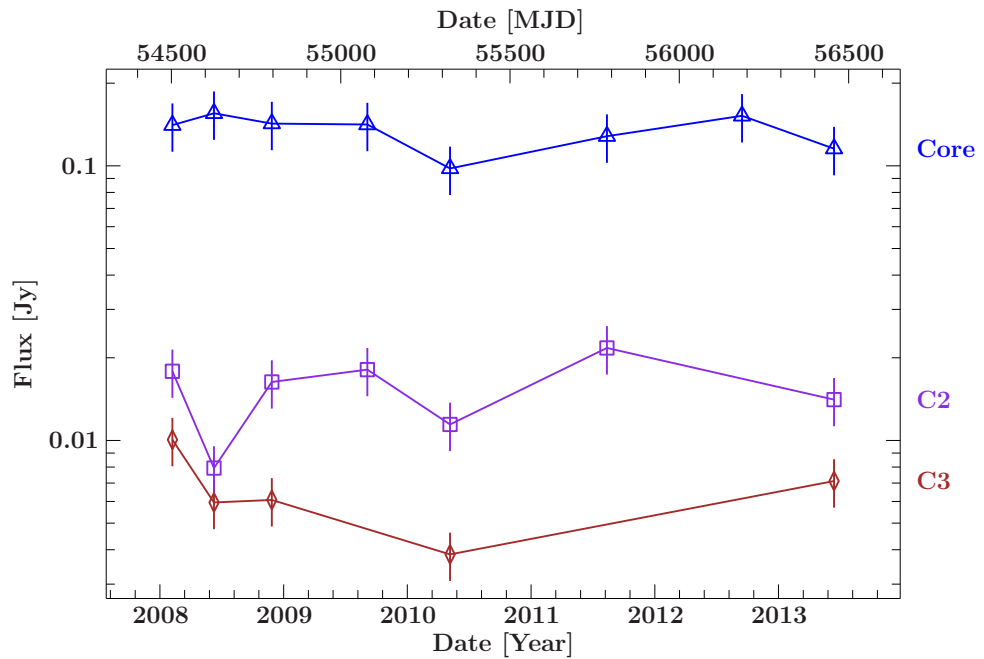


Figure 4.7.: Flux densities of the jet components of PKS 1257–326 plotted as a function of time. The error bars correspond to an estimated relative error of 20% from calibration and imaging errors according to Ojha et al. (2010).

4.2.4. Flux Density

Figure 4.7 displays the flux densities in Jansky of the individual jet components of PKS 1257–326 as a function of time. As mentioned in the previous section, a decrease in flux is expected with time, as the components move further away from the core of the jet. With the exception of a sudden drop in flux displayed by C2 and C3 in epoch V252F, a general decreasing trend is followed by both components. As for the brightness temperature, it is difficult to draw any conclusion regarding the fluctuation of the flux of C3 due to the lack of data available.

4.2.5. Kinematics

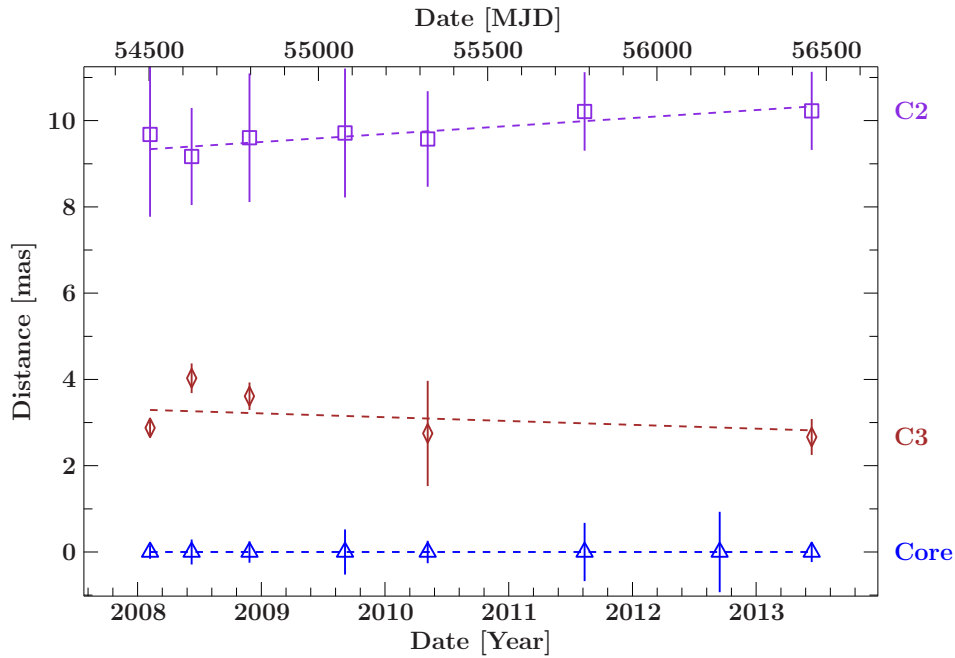


Figure 4.8.: Distance of the jet components of PKS 1257–326 relative to the position of the core component plotted as a function of time. The gradients of the dashed lines correspond to the speed of the components calculated according to the radial distance of the component from the core. The error bars correspond to the semi-major axis of the respective jet component.

Table 4.6.: Apparent speed of the jet components of PKS 1257–326 relative to the core.

Component	μ [mas/yr]	β_{app} [c]
C2	0.185 ± 0.004	11.346 ± 2.758
C3	-0.088 ± 0.160	-5.425 ± 9.842

Figure 4.8 shows the relative distance of the jet components from the core as a function of time. The calculation of the slopes and the error bars are the same as for Fig. 4.4. The speed has been calculated by linear regression of the radial distance of the components from the core component over time. These values are presented in Table 4.6, the proper motion μ in units of mas/yr and β_{app} in terms of the speed of light c . The negative slope of component C3 seems to indicate movement of the component towards the core, but comparison with the values listed in Table 4.6 shows that the error is larger than the given value, meaning that no conclusion can be drawn regarding the speed of component C3. Component C2 has a steeper positive slope, corresponding to superluminal motion with an apparently velocity $\beta_{\text{app}} = (11.346 \pm 2.758)c$.

4.3. PKS 1915–458

PKS 1915–458 is a flat-spectrum radio quasar located at $z = 2.47$ (Jackson et al. 2002). This redshift is cited from private communications with N. Tasker with no mention of measurement or observation technique and, as such, has not yet been confirmed. This source has been included in many catalogues but has not yet been studied in detail. In 2010, *Fermi*/LAT detected γ -ray emissions with a flux $E > 100$ MeV of $(0.36 \pm 0.15) \cdot 10^{-6}$ photons/cm²s from a source positionally consistent with PKS 1915–458. This flare was the first γ -ray observation of PKS 1915–458 which is unusually distant for a flaring LAT blazar (Sokolovsky et al. 2010). Following the *Fermi*/LAT detection, a *Swift* Target of Opportunity (ToO) observation was carried out with a total observation time of 8.3 ksec. The *Swift* X-ray telescope (XRT) observed an X-ray source which was also positionally consistent with PKS 1915–458 (Sokolovsky et al. 2010). Despite these observations, PKS 1915–458 was excluded from the *Fermi* 2FGL catalogue since it did not meet the likelihood Test Statistic requirement $TS > 25$ which corresponds to approximately 4σ significance (Buson 2013; Nolan et al. 2012).

4.3.1. Imaging

Four observations of TANAMI data between 1 April 2011 and 17 August 2013 were analysed for PKS 1915–458. The telescope configuration for each observation is listed in Table 4.7. Only the telescopes which provided data for this source are included in the table. Figure 4.9 shows the time evolution of PKS 1915–458 over the observation period. All four epochs show a core-dominated structure with a jet which propagates in a south-westerly direction. There are at least three substructures visible in every epoch, with a total of four individual substructures visible in epoch V252AF, although the flux of the outermost component becomes rather weak in the final observation and is no longer robust.

Table 4.7.: Observation Epochs for PKS 1915–458

Date ¹ YYYY-MM-DD	Name	Telescopes ²
2011-04-01	V252X	WW, MP, HO, HH, CD, AT
2011-11-13	V252AB	WW, DSS45, TC, PA, MP, HO, HH, CD, AT
2012-09-16	V252AF	PA, KE, HO, HH, CD, AT
2013-08-17	V252AL	YG, WW, TC, PA, MP, KE, HO, HH, CD, AT, AK

Note: ¹ date of observation ² The following abbreviations are used for the telescopes: AT: ATCA, AK: ASKAP, CD: Ceduna, HH: Hartebeesthoek, HO: Hobart, KE: Katherine, MP: Mopra, OH: O’Higgins, PA: Parkes, DSS45: Tidbinbilla (34 m), TC: TIGO, WW: Warkworth, YG: Yarragadee.

The resolution of all images is fairly consistent, facilitating a straightforward comparison of morphology between epochs. The most remarkable aspects which can be seen in the multi-epoch images of PKS 1915–458 are the consistency in morphology and the rate at which the outer components move away from the core. The kinematics of this FSRQ will be examined in further detail in Sec. 4.3.5.

4.3.2. Model Fitting

The structure of PKS 1915–458 has been model fitted with Gaussian components in accordance with Sec. 3.2.2, comprising the core and a total of three outer components. Components C2 and C3 are present in epochs V252X, V252AB, and V252AF. In the final epoch V252AL, the structure of the outermost component C2 can no longer be fitted with a Gaussian component, but a new component C4 appears between the core and C3. The model fitting parameters for each component over all epochs are presented in Table 4.8. Referring to epoch V252X, C3 lies close to the core at a radial distance of approximately 1.16 mas in a south-westerly direction and C2 is located at a distance of 3.48 mas in the same direction. A resolution limit was calculated for each component in each epoch according to Kovalev et al. (2005) (refer to Sec. 4.1 for a detailed explanation). As for PKS 0438–436, the values marked * in Table 4.8 have been increased to the resolution limit θ_{lim} , yielding a lower limit for the brightness temperature T_{B} , indicated in Table 4.8 by a †.

4.3.3. Brightness Temperature

The values of the brightness temperature of each component are plotted against time in Fig. 4.10. The brightness temperature of the core increases over time from $7.67 \cdot 10^{10}$ K in epoch V252X to $2.36 \cdot 10^{11}$ K in the final observation of epoch V252AL. This maximum value is within the limit set by the inverse Compton catastrophe of 10^{12} K, as introduced in Sec. 2.2.2. The brightness temperatures of components C2 and C3 display an overall

decrease. The change in T_B of C3 is notable, with the value decreasing steeply from $5.93 \cdot 10^9$ K in epoch V252X to $4.56 \cdot 10^8$ K in epoch V252AL, a decrease larger than one order of magnitude in just over two years. This rapid decrease is consistent with the fast evolution in morphology displayed by PKS 1915–458. The brightness temperature of C4 is not plotted since this component only appears in the final epoch V252AL. Despite this, it is interesting to note that its initial brightness temperature of $T_B = 6.81 \cdot 10^9$ K is of the same order of magnitude as the first measurement of the flux density in component C3 in epoch V252X.

4.3.4. Flux Density

Figure 4.11 displays the flux densities in Jansky of the individual jet components of PKS 1915–458 as a function of time. As mentioned in the previous sections, a decrease in flux is expected with time, as the components move further away from the core of the jet. The flux of the jet core remains fairly constant over the four epochs, while the respective fluxes of C2 and C3 demonstrate a decreasing trend, as expected. The difficulty in identifying component C2 with a Gaussian component in epoch V252AL is unsurprising when the rapidity of the decrease in flux is considered, decreasing from 0.026 Jy in epoch V252X to 0.002 Jy in epoch V252AF, a timespan of just under a year and a half. As for the brightness temperature, the flux density of component C4 has not been included in Fig. 4.11. However, the flux density of C4 $S = 0.035$ Jy as listed in Table 4.8 is exactly the same as the first measurement of the flux density of C3. When

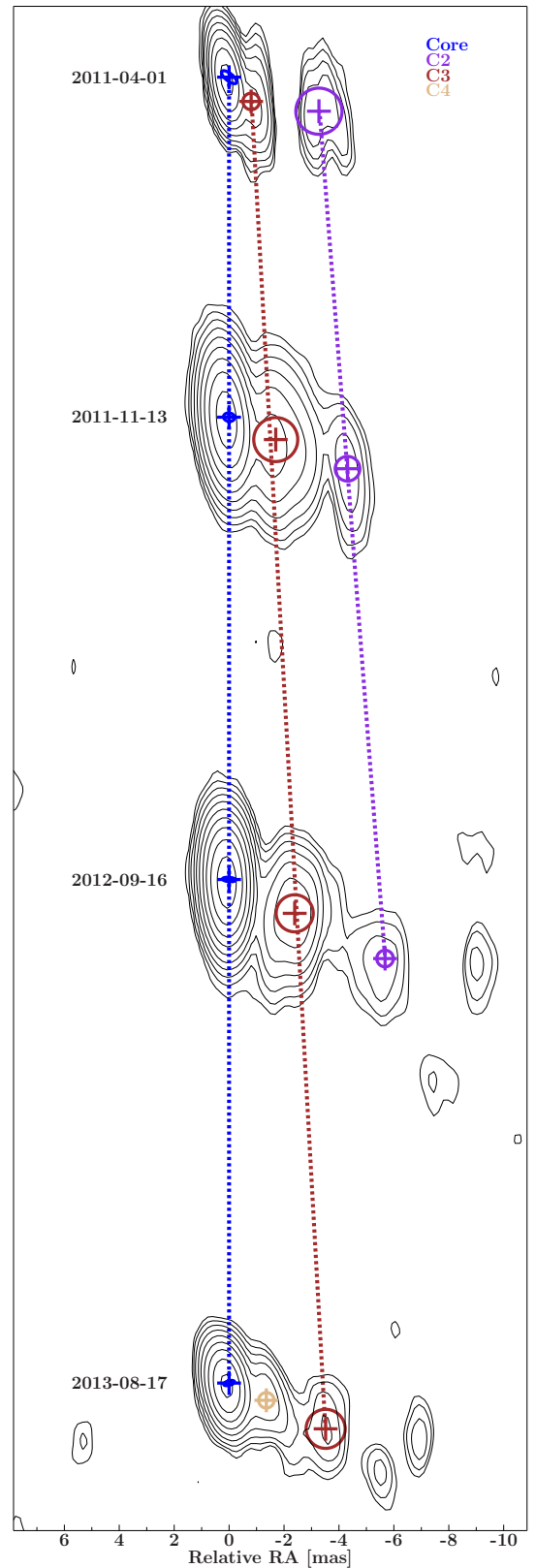


Figure 4.9.: Time evolution of PKS 1915–458.

Table 4.8.: Parameters of Gaussian models of PKS 1915–458.

Epoch Code Date	S [Jy]	R [mas]	Θ [$^\circ$]	a [mas]	b [mas]	P.A. [$^\circ$]	T_B [K]	ID
V252X 2011-04-01	0.229	0.04	0.1	0.7	0.3	51.5	$7.67 \cdot 10^{10}$	Core
	0.035	1.16	-136.2	0.6	0.6	-179.0	$5.93 \cdot 10^9$	C3
	0.026	3.48	-110.1	1.7	1.7	-175.8	$5.61 \cdot 10^8$	C2
V252AB 2011-11-13	0.142	0.06	18.4	0.4	0.3	81.8	$6.92 \cdot 10^{10}$	Core
	0.043	1.84	-114.3	1.6	1.6	116.6	$1.02 \cdot 10^9$	C3
	0.004	4.67	-113.0	0.9*	0.9*	-141.7	$3.17 \cdot 10^{8\dagger}$	C2
V252AF 2012-09-16	0.250	0.03	32.3	0.5	0.2	85.2	$2.02 \cdot 10^{11}$	Core
	0.036	2.66	-116.9	1.3	1.3	-178.9	$1.20 \cdot 10^9$	C3
	0.002	6.34	-116.7	0.6*	0.6*	-176.6	$3.63 \cdot 10^{8\dagger}$	C2
V252AF 2013-08-17	0.257	0.03	16.8	0.4	0.2	-75.3	$2.36 \cdot 10^{11}$	Core
	0.035	1.48	-114.1	0.6	0.6	-159.0	$6.81 \cdot 10^9$	C4
	0.015	3.87	-115.1	1.4	1.4	-161.2	$4.56 \cdot 10^8$	C3

Note: S is flux density; R and Θ are the coordinates of the component in which R is the distance of the component to the designated phase centre and Θ is the angle in degrees from north to east. a and b are the major and minor axes of the components, respectively. P.A. is the position angle of the major axis of the component in degrees from north to east. T_B is the brightness temperature. ID is the identification of the component. * upper limit. † lower limit.

the errors are taken into consideration, the flux densities are still very similar and clearly within the same order of magnitude.

4.3.5. Kinematics

Figure 4.12 shows the relative distance of the jet components from the core as a function of time. The calculation of the slopes error bars is the same as for Fig. 4.4. The speed has been calculated by linear regression of the radial distance of the components from the core component over time. These values are presented in Table 4.9, the proper motion μ in units of mas/yr and β_{app} in terms of the speed of light c . Component C2 has a very steep positive slope, corresponding to an apparent velocity of $\beta_{\text{app}} = (180.416 \pm 0.626)c$. However, component C2 only appears in three of the four observed epochs and, as such, is not a reliable indication of the velocity of the jet when considered individually. Component C3 is identified in all four of the observations and according to the kinematics analysis, moves with an apparent velocity of $\beta_{\text{app}} = (101.265 \pm 3.811)c$. Although not quite as extraordinarily fast as C2, this is still an astonishingly fast apparent velocity,

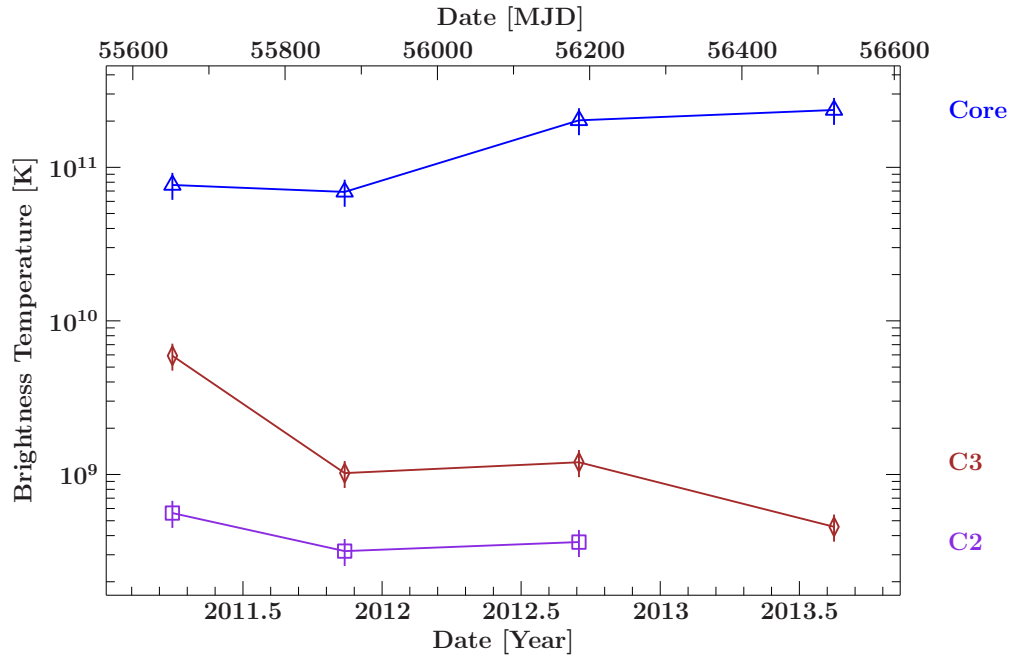


Figure 4.10.: Brightness temperature of the jet components of PKS 1915–458 plotted as a function of time. The error bars correspond to an estimated relative error of 20% from calibration and imaging errors according to Ojha et al. (2010).

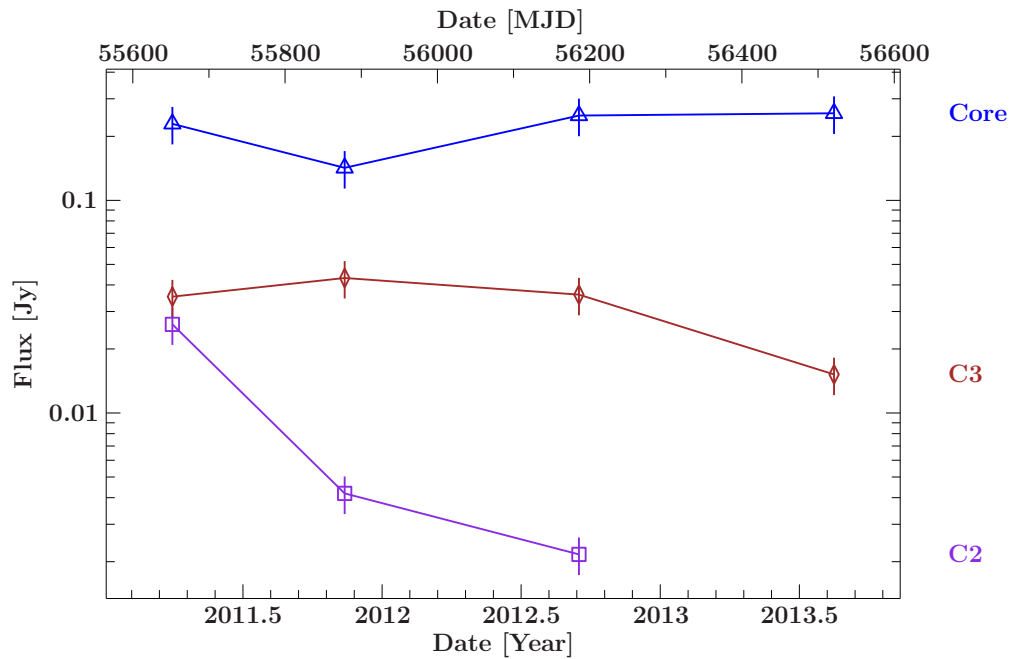


Figure 4.11.: Flux densities of the jet components of PKS 1915–458 plotted as a function of time. The error bars correspond to an estimated relative error of 20% from calibration and imaging errors according Ojha et al. (2010).

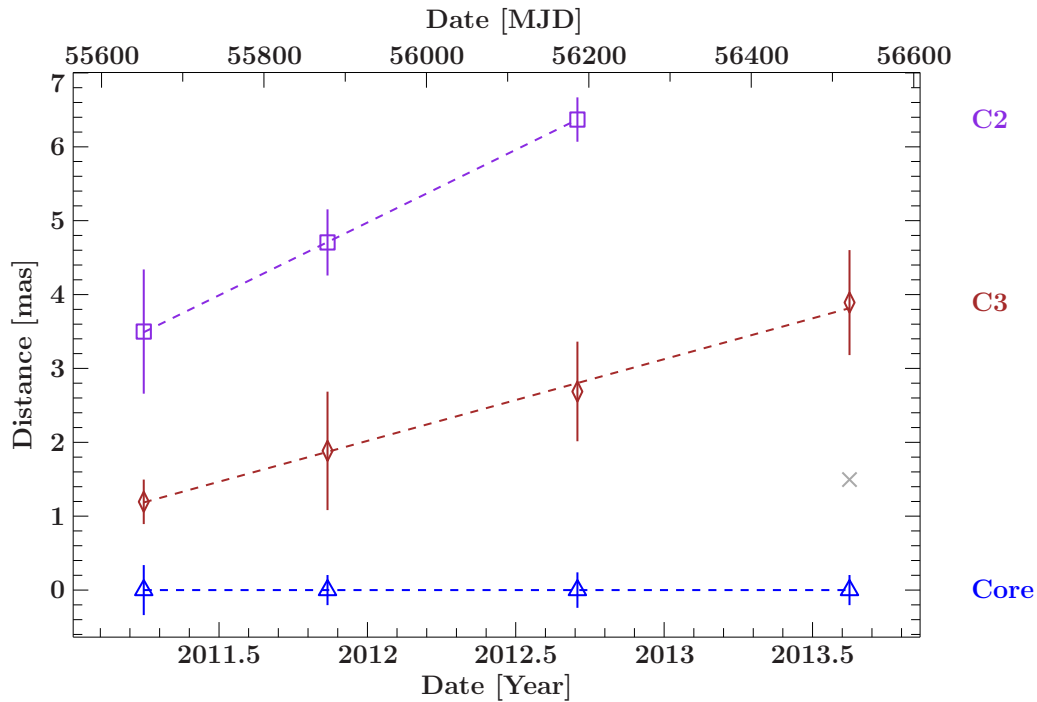


Figure 4.12.: Distance of the jet components of PKS 1915–458 relative to the position of the core component plotted as a function of time. The gradients of the dashed lines correspond to the speed of the components calculated according to the radial distance of the component from the core. The error bars correspond to the semi-major axis of the respective jet component.

Table 4.9.: Apparent speed of the jet components of PKS 1915–458 relative to the core.

Component	μ [mas/yr]	β_{app} [c]
C2	1.970 ± 0.007	180.416 ± 0.626
C3	1.106 ± 0.042	101.265 ± 3.811

in agreement with the initial impression of the jet’s speed as indicated by the apparent velocity of component C2. Although the determined apparent velocities are not conclusive due to the small number of available observations, the development of component C4 between epochs V252AF and V252AL supports the initial kinematics analysis for the extremely fast apparent velocity of component C3. Component C4 is indicated by a grey cross in Fig. 4.12. Although single data points are not usually included in such plots, C4 was included in Fig. 4.12 to emphasise the apparent velocity of the jet of PKS 1915–458. In epoch V252AL, C4 appears at a radial distance $R = 1.45$ mas from the core. It can be inferred that the jet component travelled this distance within the eleven months since the previous observation, yielding a value of $\mu = 1.58$ mas/yr for

the proper motion of C4, approximately between the values of proper motion for components C3 and C2. The apparent superluminal motion of the jet at such large speeds is especially interesting when the high redshift $z = 2.47$ of PKS 1915–458 is considered. This will be discussed further in Sec. 5.2.3.

4.4. PKS 2106–413

PKS 2106–413 is a flat-spectrum radio quasar located at $z = 1.058$ (White et al. 1988) with a moderately polarised radio core with 3.5% polarisation, according to Impey & Tapia (1990). Although this source has been included in many larger catalogues, it has not been extensively studied as an individual source. Siebert et al. (1998) studied PKS 2106–413 as part of an investigation of the X-ray properties of the Parkes sample of FSRQs, including a detection by ROSAT of 0.033 ± 0.012 counts/s. In 2014, the γ -ray-quiet PKS 2106–413 was included in an investigation of how jet-bending in AGNs is affected by γ -ray emissions. PKS 2106–413 was identified as having no parsec scale bends ($N_{pc} = 0$) and a maximum jet-bend angle of 0° (Graham & Tingay 2014). More recently, Böck et al. (2016) included PKS 2106–413 in an analysis of the radio and gamma-ray properties of extragalactic jets from the TANAMI sample. PKS 2106–413 does not have a γ -ray counterpart in the 1FGL catalogue, allowing only the calculation of upper limits for γ -ray flux and luminosity. It is notable that the likelihood Test Statistic for PKS 2106–413 is listed as $TS = 0$.

4.4.1. Imaging

Table 4.10.: Observation Epochs for PKS 2106–413

Date ¹ YYYY-MM-DD	Name	Telescopes ²
2008-02-07	V252C	HH, CD, HO, MP, AT, PA
2008-06-09	V252F	HART, CD, HO, MP, AT, PA
2008-11-27	V252I	DSS43, OH, CD, HO, MP, AT, PA
2010-07-24	V252S	DSS43, TC, PA, MP, HO, CD, AT
2011-04-01	V252X	WW, MP, HO, HH, CD, AT
2011-11-13	V252AB	WW, DSS43, DSS45, TC, MP, HO, CD, AT
2012-09-16	V252AF	DSS43, DSS34, PA, KE, HO, HH, CD, AT, AK
2013-08-17	V252AL	YG, WW, TC, PA, MP, KE, HH, CD, AT, AK

Note: ¹ date of observation

² The following abbreviations are used for the telescopes: AT: ATCA, AK: ASKAP, CD: Ceduna, HH: Hartebeesthoek, HO: Hobart, KE: Katherine, MP: Mopra, OH: O’Higgins, PA: Parkes, DSS43 & DSS45/34: Tidbinbilla (70 m and 34 m), TC: TIGO, WW: Warkworth, YG: Yarragadee.

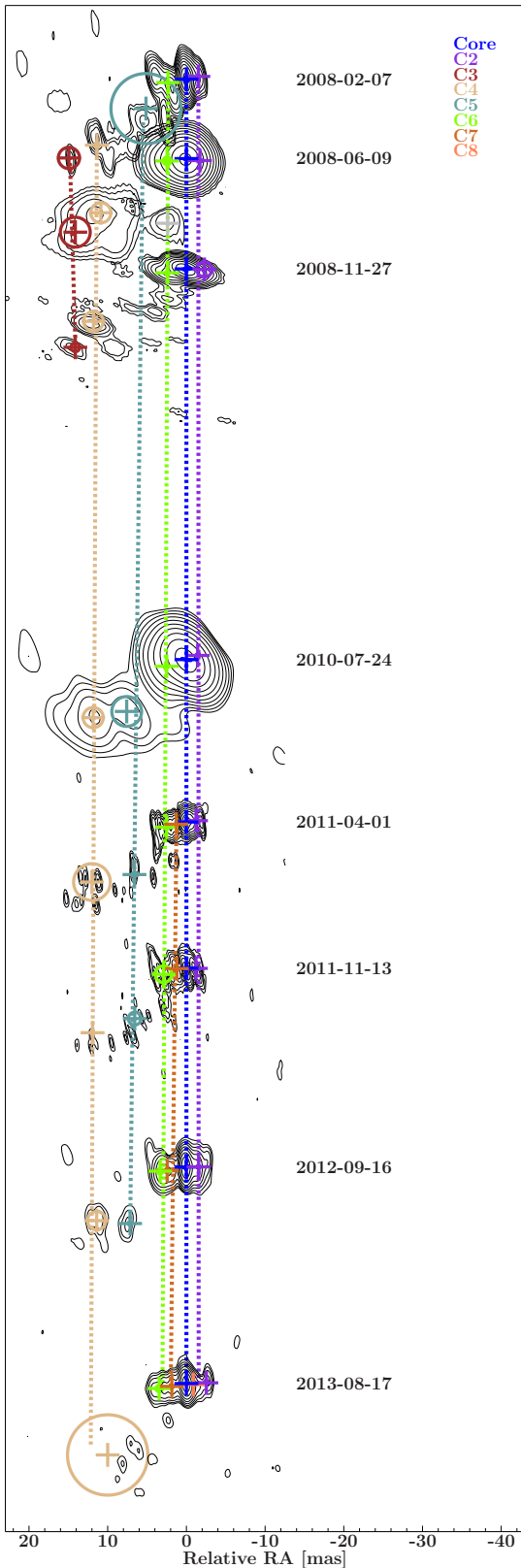


Figure 4.13.: Time evolution of PKS 2106–413.

Eight observations of TANAMI data between 7 February 2008 and 17 August 2013 were analysed for PKS 2106–413. The telescope configuration for each observation is listed in Table 4.10. Only the telescopes which provided data for this source are included in the table.

Figure 4.13 shows the time evolution of PKS 2106–413 over the observation period. All epochs of PKS 2106–413 display a core-dominated structure with a compact jet. The structure of the jet is somewhat more complex than the previous three sources, with substructures visible on both sides of the core. The jet initially follows a trajectory directly to the west of the core before doubling back on itself and propagating in a south-easterly direction. There is a discrepancy in the angular resolution obtained with different observations. The images for epochs V252I and V252O have the lowest resolution, and the presence of the jet structure to the west of the core component can only be inferred, not directly identified. The inner structure closest to the core appears to expand in both directions, both eastward and westward of the core. The integrity of the diffuse outer structures varies over the epochs, partially because of the difference in resolution and partially because the outer regions of the jet are relatively weak compared to the core, as can be seen by the concentration of contours. Individual images of each epoch are included in Appendix A.4, in which the morphology of the complex inner structure of PKS 2106–413 can be studied in further detail.

Table 4.11.: Parameters of Gaussian models of PKS 2106–413.

Epoch Code	S	R	Θ	a	b	P.A.	T_B	ID
Date	[Jy]	[mas]	[$^\circ$]	[mas]	[mas]	[$^\circ$]	[K]	
V252C 2008-02-07	1.074	0.01	−106.0	0.7	0.5	−2.3	$9.99 \cdot 10^{10}$	Core
	0.083	1.57	−76.9	0.2*	0.2*	−90.0	$4.91 \cdot 10^{10\dagger}$	C2
	0.074	2.36	100.4	0.2*	0.2*	90.0	$7.79 \cdot 10^{10\dagger}$	C6
	0.137	6.34	126.1	8.9	8.9	−87.5	$6.23 \cdot 10^7$	C5
	0.018	14.12	126.4	0.6*	0.6*	107.8	$1.94 \cdot 10^{9\dagger}$	C4
	0.002	17.96	123.9	2.7*	2.7*	80.4	$8.37 \cdot 10^{6\dagger}$	C3
V252F 2008-06-09	1.204	0.05	−84.4	0.6	0.1*	−68.2	$7.75 \cdot 10^{11\dagger}$	Core
	0.040	1.79	−97.9	0.4*	0.4*	−76.0	$1.15 \cdot 10^{10\dagger}$	C2
	0.121	2.43	97.1	1.0	1.0	108.4	$4.60 \cdot 10^9$	C6
	0.026	12.82	122.4	2.6	2.6	−64.8	$1.45 \cdot 10^8$	C4
	0.027	16.9	123.6	3.8	3.8	−63.2	$6.75 \cdot 10^7$	C3
V252I 2008-11-27	1.016	0.04	−79.2	0.8	0.2	−80.4	$1.77 \cdot 10^{11}$	Core
	0.030	2.33	−91.5	1.9	1.9	−79.9	$2.93 \cdot 10^8$	C2
	0.074	2.43	101.5	3.4	3.4	90.0	$2.27 \cdot 10^{10}$	C6
	0.043	13.5	119.5	2.5	2.5	125.0	$2.51 \cdot 10^8$	C4
	0.004	17.24	124.3	1.1*	1.1*	80.7	$1.30 \cdot 10^{8\dagger}$	C3
V252S 2010-07-24	0.613	0.03	−26.2	1.2	0.1*	79.8	$1.71 \cdot 10^{11\dagger}$	Core
	0.072	1.55	−69.0	0.4	0.4	−90.0	$1.64 \cdot 10^{10}$	C2
	0.076	2.62	108.3	0.4*	0.4*	108.4	$1.99 \cdot 10^{10\dagger}$	C6
	0.020	10.02	130.9	3.8	3.8	180.0	$5.05 \cdot 10^7$	C5
	0.019	13.93	121.8	2.6	2.6	−174.0	$1.04 \cdot 10^8$	C4
V252X 2011-04-01	0.390	0.05	93.3	0.5	0.05*	75.8	$6.30 \cdot 10^{11}$	Core
	0.159	1.18	−82.0	0.5	0.5	−79.7	$2.71 \cdot 10^{10}$	C2
	0.090	1.35	102.2	0.2*	0.2*	103.6	$8.11 \cdot 10^{10}$	C7
	0.105	2.64	104.6	0.4	0.4	114.2	$2.84 \cdot 10^{10}$	C6
	0.010	9.43	135.1	0.6*	0.6*	135.0	$1.16 \cdot 10^9$	C5
	0.057	14.26	122.4	4.7	4.7	113.9	$9.36 \cdot 10^7$	C4
V252AB 2011-11-13	0.280	0.04	5.1	0.5	0.07*	−24.6	$2.88 \cdot 10^{11}$	Core
	0.145	1.20	−89.0	0.4	0.4	−79.7	$3.39 \cdot 10^{10}$	C2
	0.115	1.21	90.3	0.3	0.3	103.6	$3.48 \cdot 10^{10}$	C7
	0.113	2.99	104.1	2.1	2.1	113.2	$9.12 \cdot 10^8$	C6
	0.023	9.14	134.1	1.6	1.6	101.4	$3.18 \cdot 10^8$	C5
	0.012	14.45	124.4	0.3*	0.3*	−63.2	$3.50 \cdot 10^9$	C4

Continued on next page.

Table 4.11 continued from previous page

Epoch Code	S	R	Θ	a	b	P.A.	T_B	ID
Date	[Jy]	[mas]	[°]	[mas]	[mas]	[°]	[K]	
	0.436	0.03	−141.6	0.7	0.05*	−71.1	$4.20 \cdot 10^{11}$	Core
	0.078	1.57	−90.4	0.4	0.4	−85.6	$2.17 \cdot 10^{10}$	C2
V252AF	0.075	2.47	101.6	0.5	0.5	114.2	$1.05 \cdot 10^{10}$	C7
2012-09-16	0.044	3.36	99.5	0.7	0.7	103.6	$3.23 \cdot 10^9$	C6
	0.010	10.14	135.4	0.5	0.5	153.7	$1.68 \cdot 10^9$	C5
	0.018	13.28	121.0	2.3	2.3	144.7	$1.21 \cdot 10^8$	C4
	0.373	0.03	101.0	0.5	0.03*	−82.5	$8.31 \cdot 10^{11}$	Core
	0.051	0.85	−99.7	0.2	0.2	−90.0	$3.69 \cdot 10^{10}$	C8
V252AL	0.021	2.52	−88.0	0.6	0.6	−87.0	$1.95 \cdot 10^9$	C2
2013-08-17	0.057	1.92	101.0	0.3*	0.3*	103.6	$1.86 \cdot 10^{10}$	C7
	0.046	3.55	100.3	0.8	0.8	114.2	$2.41 \cdot 10^9$	C6
	0.015	13.53	132.1	10.2	10.2	114.9	$5.23 \cdot 10^6$	C4

Note: S is flux density; R and Θ are the coordinates of the component in which R is the distance of the component to the designated phase centre and Θ is the angle in degrees from north to east. a and b are the major and minor axes of the components, respectively. P.A. is the position angle of the major axis of the component in degrees from north to east. T_B is the brightness temperature. ID is the identification of the component. * upper limit. † lower limit.

4.4.2. Model Fitting

The structure of PKS 2106–413 has been model fitted with Gaussian components in accordance with Sec. 3.2.2, comprising the core and a total of seven other components over the eight epochs, a more complicated model than the previous sources. Interestingly, PKS 2106–413 can be described by a model which has Gaussian components on both sides of the core component, consistent with the first impression of the morphology. The components C2 and C6 nearest to the core are present in all eight observations. The outermost component C3 is only present in epochs V252C, V252F and V252I. Component C4 is present in all eight observations and is the outermost component from epoch V252S onwards. Component C5 is identified in all epochs excluding V252F and V252I. Components C2 and C6 are joined by components C7 to the west of the core in epoch V252X and C8 to the east of the core in epoch V252AL. The model fitting parameters for each component over all epochs are presented in Table 4.11. Referring to epoch V252C, component C2 is at a radial distance of 1.57 mas almost directly to the west of the core and remains fairly stationary throughout the remaining epochs, as will be mentioned later in Sec. 4.4.5. Component C6 is located at a distance of 2.36 mas directly to the east and slightly southward of the core, forming a line between the core,

C2 and C6. Component C5 is located at a steeper angle southeast of the core at a distance of 6.34 mas but is only identified in five of the eight observations. Component C4, the most consistently identifiable and fittable of the outer jet components, lies at a distance of 14.12 mas in a southeasterly direction. C3 is located at a radial distance of 17.96 mas southeast of the core. This component is only present in epochs V252C, V252F and V252I. In epoch V252X, a new component, C7 appears at a radial distance of 1.18 mas from the core, between the core and C6. The final component which comprises the intricate inner structure of this jet is first identified in the final observation epoch, V252AL. Component C8 lies at a radial distance of 0.85 mas between the core and C2. In the final epoch, C4 loses structure, becoming difficult to model. A resolution limit was calculated for each component in each epoch according to Kovalev et al. (2005) (refer to Sec. 4.1 for a detailed explanation). As for all other sources, the values marked * in Table 4.11 have been increased to the resolution limit θ_{lim} , yielding a lower limit for the brightness temperature T_{B} , indicated in Table 4.11 with a †.

4.4.3. Brightness Temperature

The values of the brightness temperature of each component is plotted against time in Fig. 4.14. The brightness temperature of the core increases over time from $9.99 \cdot 10^{10}$ K in epoch V252C to $1.71 \cdot 10^{11}$ K in the final observation of epoch V252AL. This maximum value is within the limit set by the inverse Compton catastrophe of 10^{12} K, as introduced in Sec. 2.2.2. The brightness temperatures of the remaining components are fairly scattered, with C2, C4, C6, and C7 displaying a decreasing overall trend, and C3 and C5 displaying an overall increase in brightness temperature. The evolution of C2 is particularly curious, initially dropping abruptly from $4.91 \cdot 10^{10}$ K in epoch V252C to $2.93 \cdot 10^8$ K in epoch V252I, a decrease larger than two orders of magnitude. Within the year and a half between epochs V252I and V252S, the next available observation of PKS 2106–413, the brightness temperature of C2 increases to $1.64 \cdot 10^{10}$ K, slowly increasing over the next two epochs before dropping back down to a final value of $1.95 \cdot 10^9$ K. Possible explanations for this unusual behaviour will be discussed in Sec. 5.2.4.

4.4.4. Flux Density

Figure 4.15 displays the flux densities in Jansky of the individual jet components of PKS 2106–413 as a function of time. As mentioned in the previous sections, a decrease in flux is expected with time, as the components move further away from the core of the jet. The change in flux of the components of PKS 2106–413 is slightly less confusing than that of the brightness temperature, with most components following an overall decreasing trend. The exception is component C3, which displays an unexpected spike in flux in epoch V252F. Possible explanations for this surprising feature will be discussed further in Sec. 5.2.4.

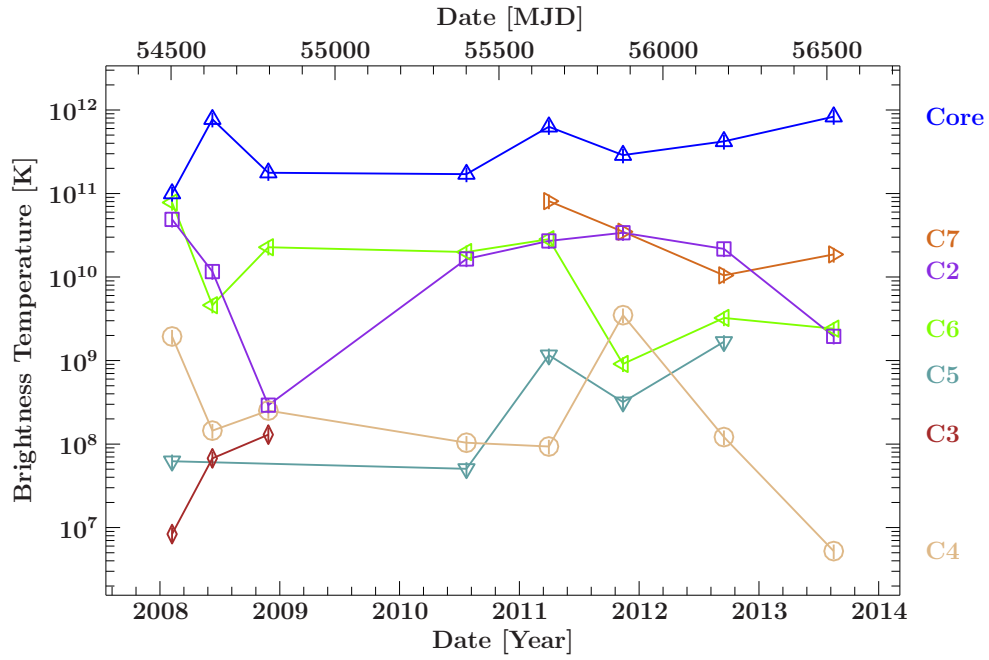


Figure 4.14.: Brightness temperature of the jet components of PKS 2106–413 plotted as a function of time. The error bars correspond to an estimated relative error of 20% from calibration and imaging errors according to Ojha et al. (2010).

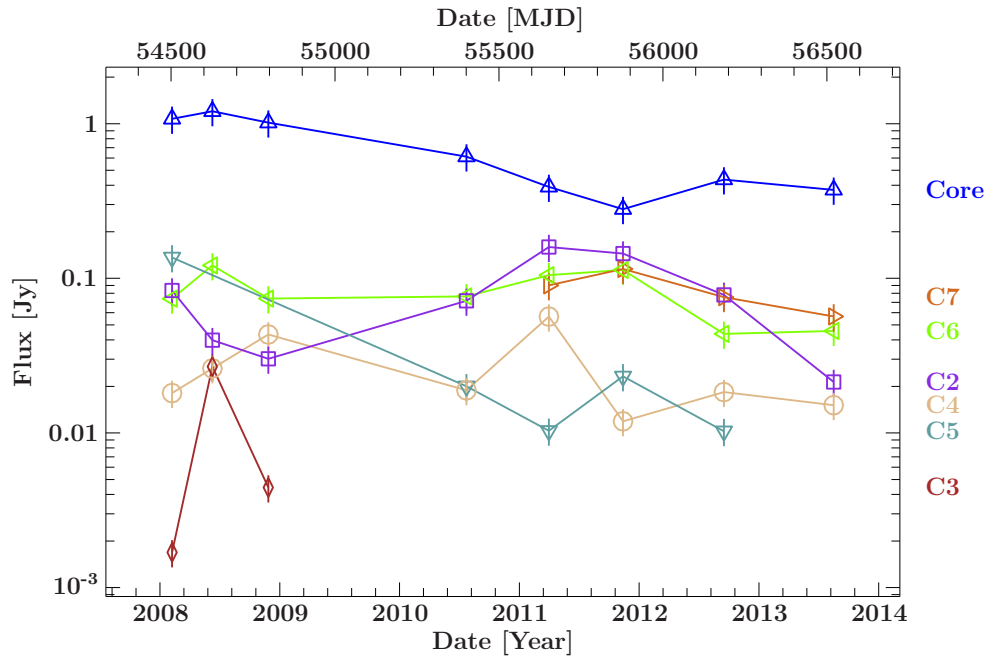


Figure 4.15.: Flux densities of the jet components of PKS 2106–413 plotted as a function of time. The error bars correspond to an estimated relative error of 20% from calibration and imaging errors according to Ojha et al. (2010).

4.4.5. Kinematics

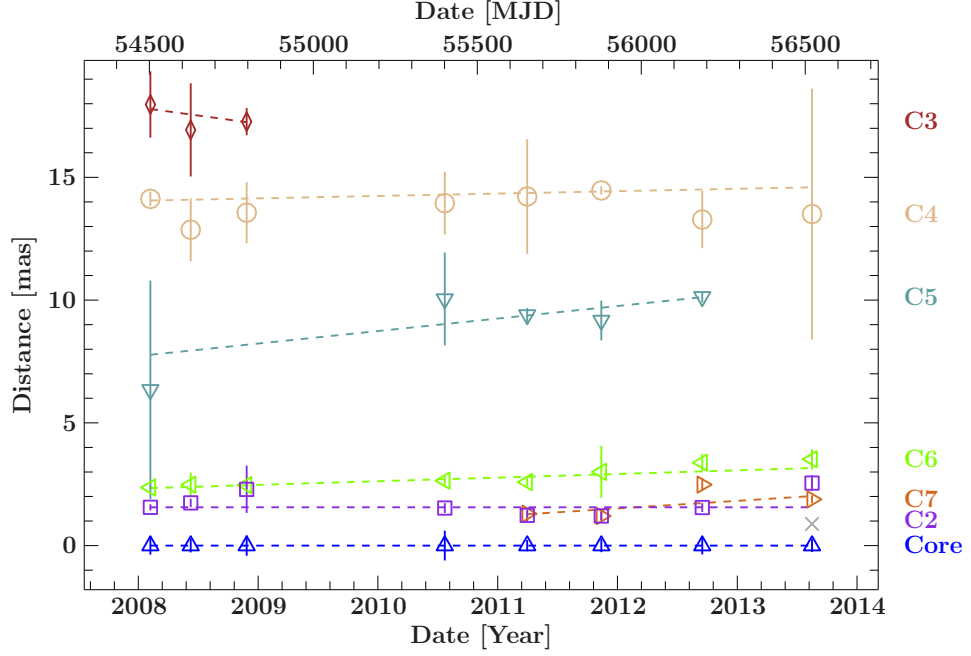


Figure 4.16.: Distance of the jet components of PKS 2106–413 relative to the position of the core component plotted as a function of time. The gradients of the dashed lines correspond to the speed of the components calculated according to the radial distance of the component from the core. The error bars correspond to the semi-major axis of the respective jet component.

Table 4.12.: Apparent speed of the jet components of PKS 2106–413 relative to the core.

Component	μ [mas/yr]	β_{app} [c]
C2	0.001 ± 0.059	0.036 ± 3.220
C3	-0.666 ± 0.623	-36.251 ± 3.391
C4	0.098 ± 0.056	5.330 ± 3.040
C5	0.509 ± 0.125	27.715 ± 6.828
C6	0.148 ± 0.033	8.043 ± 1.772
C7	0.310 ± 0.191	16.883 ± 10.424

Figure 4.16 shows the relative distance of the jet components from the core as a function of time. The slopes of the dashed lines correspond to the speed of the components and the error bars have been estimated from the semi-major axis of the jet component. The speed has been calculated by linear regression of the radial distance of the components from the core component over time. These values are presented in Table 4.12, proper motion

μ in units of mas/yr and β_{app} in terms of the speed of light c . As previously mentioned, component C2 remains fairly stationary with $\mu = 0.001 \pm 0.059$ mas. Based on the gradient of the dashed line for C3, this component appears to move rapidly towards the core. However, the proper motion listed for component C3 $\mu = -0.666 \pm 0.623$ mas in Table 4.12 is almost zero when the error is considered, and is not reliable since this component is only present in three epochs; C3 can no longer be identified after epoch V252I. The apparent velocities for the sources are unremarkable; the intriguing feature of this source is the morphology of the inner structure with components identifiable on both sides of the core.

5. Discussion

5.1. Possible Reasons for γ -ray Faintness

As briefly mentioned in Sec. 1, there are four main explanations for the lack of γ -ray detections of the four FSRQs in this sample. The first possibility is that due to a high redshift, the extragalactic background light plays a significant role in absorption of γ -radiation before it can be detected; γ -ray extinction is caused by pair production in the soft background photon field (Punsly et al. 2018).

According to Franceschini et al. (2008), the extragalactic background light across different frequencies is an essential factor which contributes to opacity with regard to the propagation of high-energy photons. As mentioned in Sec. 2.2.4, very high-energy photons are susceptible to opacity effects caused by photon-photon interactions and pair-production in local backgrounds, for example the photon population in the BLR. Due to the high density of photons of 400 cm^{-3} in the cosmic microwave background (CMB), photons with energies above 100 TeV have a very short mean free path and, as such, decay rapidly. This means that extragalactic sources which emit γ -radiation above this threshold energy are undetectable. The detectability of sources below 100 TeV depends on their distance. This is due to the opacity caused by other background emissions than the CMB. Figure 5.1 shows the redshift distributions for FSRQs and BL Lacs in the 2LAC and 3LAC Clean Samples. The average redshift of the γ -ray detected FSRQs lies at $\langle z \rangle = 1.33 \pm 0.08$, showing that the number density of FSRQs increases up to a limit

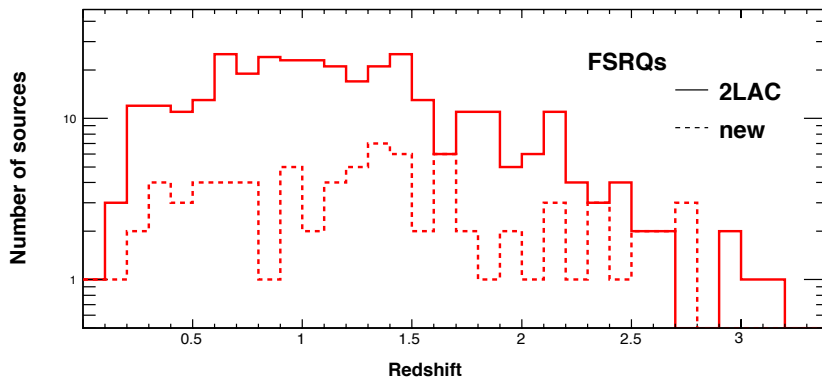


Figure 5.1.: The redshift distribution of FSRQs, BL LACs, and different kinds of BL Lacs. Solid lines are 2LAC sources; dashed lines are new 3LAC sources. Image credit: Ackermann et al. (2015).

$z \simeq 0.5 - 2.0$ before decreasing rapidly at redshifts $z > 2.0$ (Ackermann et al. 2015).

The second possibility is that the luminosity of a source is too high, causing a redshift of the SED, shifting the synchrotron peak out of the observation window of *Fermi*/LAT. Figure 5.2 shows the analytical approximations of blazar SEDs for five different γ -ray luminosity bins plotted over the SEDs of all blazars included in the sample by Ghisellini (2016). The sample consists of all blazars with redshift which have been detected by *Fermi*/LAT and are listed in the 3LAC catalogue. As the luminosity increases, the Compton dominance of the SED increases and the peaks are shifted to the left. The γ -ray spectrum becomes steeper with increasing luminosity. The fixed passband of *Fermi*/LAT makes detection difficult for AGN with inverse Compton peaks located below 1 GeV or those with steep γ -ray spectra (Lister et al. 2015).

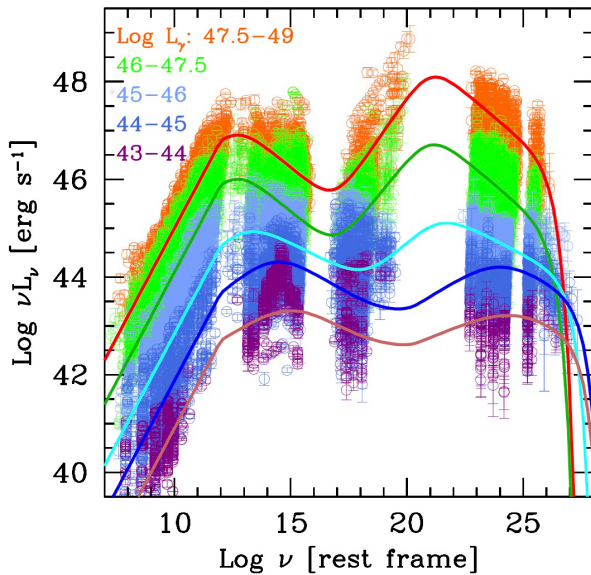


Figure 5.2.: The phenomenological blazar sequence for different γ -ray luminosities superimposed on all blazars from the sample of Ghisellini (2016). Image credit: Ghisellini (2016).

phenomenon has been explained in Sec. 2.2.2. Costamante et al. (2018) conducted a study of the population of γ -ray bright FSRQs, focusing on the absorption of γ -radiation in the BLR. Following the model that γ -rays are produced by external Compton scattering on the photons in the BLR poses the conundrum that these same external photons subsequently become targets for γ - γ collisions and pair productions. Combined with the densities used for EC modelling, this means that the BLR is opaque to γ -rays with energies above tens of GeV. The existence of the "blazar zone" (the region in which γ -rays are produced) inside the BLR should produce a cut-off in the γ -ray spectrum for energies above ~ 20 GeV. Two seemingly contradictory pieces of evidence were provided by the data collected by *Fermi*/LAT: some bright FSRQ spectra showed no indications of such

The peak frequencies of the synchrotron and Compton components of the SEDs of the complete sample of blazars included in the 3LAC catalogue are displayed in Fig. 5.3. For low γ -ray luminosity, the peak frequencies are doubly valued, corresponding to the catalogue classification of the blazar as a BL LAC or an FSRQ. As briefly mentioned in Sec. 2.2.1, at a synchrotron frequency $\nu_s \sim 10^{12}$ Hz, the most compact component of the jet will self-absorb, potentially obscuring the actual synchrotron peak. The Compton peak of such sources exists at $\nu_C \lesssim 1$ MeV, above which the spectrum is steep, implying weak emissions in the range of 0.1 – 100 GeV which remain undetected by *Fermi*/LAT (Ghisellini 2016).

The third possibility is γ - γ absorption and pair-production in the BLR of the AGN. The mechanism behind this phe-

a cut-off with SED extending up to ~ 100 GeV, while others displayed breaks around energies of 3 – 5 GeV which were interpreted as evidence of γ - γ absorption (Costamante et al. 2018). The initial contradiction can be explained by the existence of different blazar zones in different locations along the jet. Sometimes the observed γ -rays are produced inside the BLR; sometimes they are produced outside the BLR. The vast majority of *Fermi*/LAT detected blazars seem to have γ -ray emission which originates outside BLR, however, a small percentage of FSRQs display spectra consistent with strong BLR absorption. It is possible that the sample of four FSRQs in this work have been so scarcely detected by *Fermi*/LAT because of the lack of a blazar zone outside the BLR.

The fourth contributing factor to the lack of γ -ray detections of the four FSRQs in this sample is the consideration that the emissions are generally too weak to be detected by *Fermi*/LAT. In this case, it is also important to consider the activity state of the jet during the observation period (Lister et al. 2015). If the flux is weak across all energies, it is likely that the lower cut-off energy for a *Fermi*/LAT detection will not be reached. Due to the correlation in the peaks of SEDs as mentioned in Sec. 2.1.4, this scenario is also applicable to bright FSRQs which have synchrotron peaks below $10^{13.4}$ Hz. The high-energy Compton peaks of the SEDs will then be present at energies lower than the cut-off of *Fermi*/LAT, yielding low γ -ray flux.

Figure 5.4 shows the γ -ray energy flux plotted against the radio flux density at 1.4 GHz. There is a clear correlation between γ -ray energy flux and radio flux density, which becomes even stronger if the γ -ray photon flux is considered rather than the energy flux. The red points are of particular interest in the scope of this thesis. When comparing the sources which have been γ -ray detected by *Fermi*/LAT, the FSRQs included in the 3LAC catalog are brighter overall than the BL Lacs. These radio-bright FSRQs have higher detection thresholds due to their soft spectra in the LAT band (Ackermann et al. 2015). It is also important to consider the possibility that the γ -ray duty cycle of FSRQs is low, meaning that the undetected sources have not yet been active during the observational lifetime of *Fermi*/LAT and are likely to be detected in the future (Ackermann et al. 2011).

In the following sections, the individual results of each source presented in Sec. 4 will be reviewed. Combining current research and the scientific background material covered

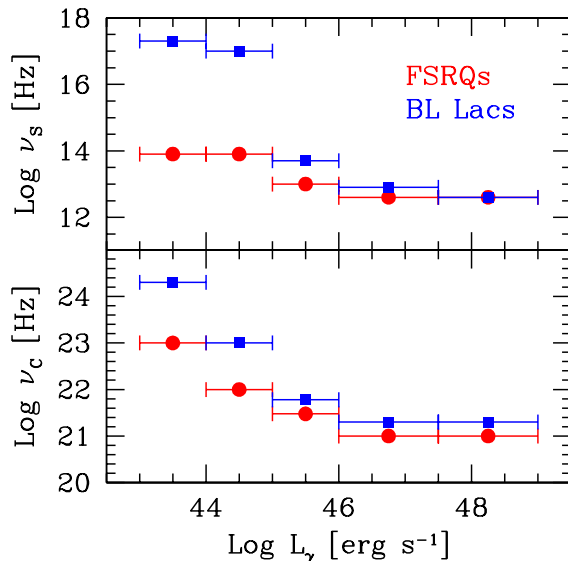


Figure 5.3.: The peak frequencies of the synchrotron (top) and Compton (bottom) peaks of the SEDs of FSRQs (red) and BL Lacs (blue) as a function of γ -ray luminosity. Image credit: Ghisellini (2016).

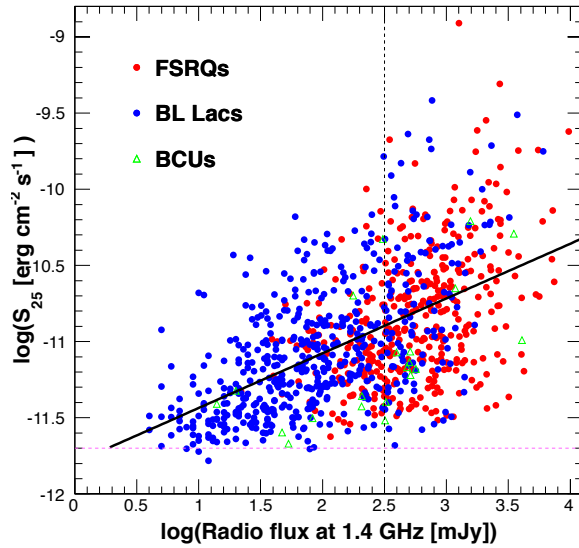


Figure 5.4.: γ -ray energy flux plotted against radio flux density at 1.4 GHz. The red circles are FSRQs, the blue circles are BL Lacs, and the green triangles are BCUs. The horizontal dashed line represents the approximate *Fermi*/LAT detection limit; the vertical dashed line is a sample separation limit used for further analysis. The solid diagonal line is the best-fit power law relation. Image credit: Ackermann et al. (2015).

in Sec. 2, the unusual behaviour of PKS 0438–436, PKS 1257–326, PKS 1915–458, and PKS 2106–413 respectively can be explained by varying combinations of the four aforementioned theories.

5.2. Individual Discussion of Sources

5.2.1. PKS 0438–436

Of the sample of the four FSRQs included in the scope of this thesis, PKS 0438–436 has displayed the strongest γ -ray flare, as published by Cheung (2016). The conclusions drawn based on this observation can be used as guidelines for interpreting the behaviour of the remaining three FSRQs in the sample. The preliminary detection by *Fermi*/LAT prompted a detailed analysis of PKS 0438–436 by Punsly et al. (2018), who executed a time-resolved spectral analysis for the 54-hour flaring period. During the full flare period, PKS 0438–436 was detected with a significance of $\gtrsim 10\sigma$. Above 10 GeV, no official detection has been made; only upper limits have been set. This is partially due to the large distance $z = 2.856$, which causes low number statistics for this flare, and partially due to the opacity of the EBL. As mentioned in the preamble to this section, γ -ray extinction is caused by pair-production with the background photon population.

Figure 5.5 shows the spectral energy distribution for PKS 0438–436 from radio to γ -ray energies. The red squares denote the synchrotron peak, the blue squares represent

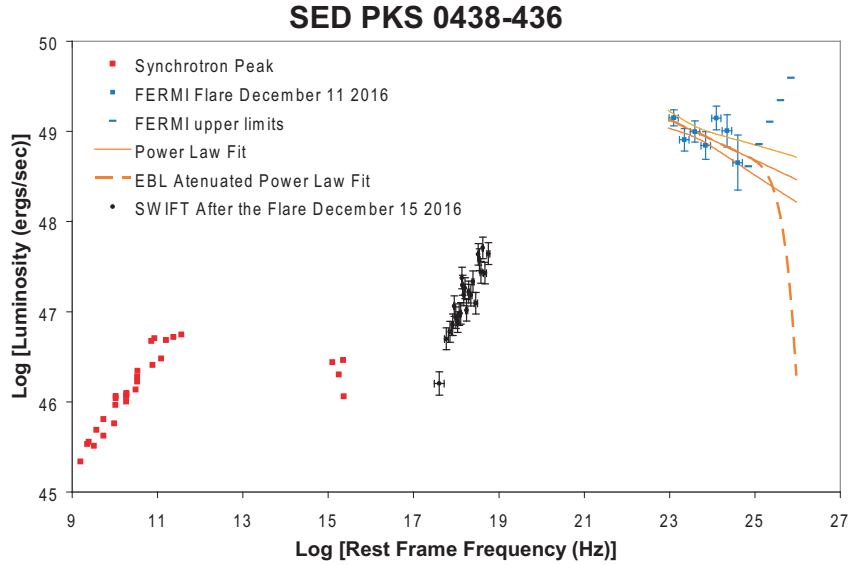


Figure 5.5.: Spectral energy distribution for PKS 0438–436 from radio to γ -ray energies. Image credit: Punsly et al. (2018).

the *Fermi*/LAT flare, and the blue dashes represent the *Fermi*/LAT upper limits. The black dots are the *Swift* observations taken two days after the flare obtained using the *Swift* XRT product generator. The γ - γ optical depths for a redshift $z = 2.85$ were used to calculate the EBL attenuation, which is shown as a dashed red line in Fig. 5.5. It was not possible to distinguish between the EBL extinction and the intrinsic high-energy cut-off because the opacity of the EBL becomes relevant above ≈ 70 GeV and the upper limits in the SED start at ≈ 10 GeV. The orange lines denote intrinsic power-law fits to the data. The radio data were obtained from the NASA Extragalactic Database and the optical data from the RGO Spectrograph on the 3.9 m Anglo Australian Telescope. Although the data were not taken contemporaneously, it is clear to see that the inverse Compton γ -ray peak $> 5 \cdot 10^{49}$ erg/s is substantially stronger than the synchrotron peak $\sim 2 \cdot 10^{47}$ erg/s (Punsly et al. 2018). According to Ghisellini et al. (2010), this dominance of the Compton peak in the SED is a typical characteristic of strong γ -ray FSRQs. Additionally, Punsly et al. (2018) stated that the luminosity of PKS 0438–436 during the flare is ~ 100 times that of the quiescent upper limit given by Böck et al. (2016) for 4 August 2008 - 4 July 2009, which indicates PKS 0438–436’s extreme variability. Despite a low averaged γ -ray luminosity due to the rarity of its detections (Böck et al. 2016), the luminosity of PKS 0438–436’s flare varies over a range of $\approx 55\% - 65\%$ of 3C 454.3’s astoundingly strong γ -ray flare (Abdo et al. 2011). This is particularly astonishing because due to the large distance of PKS 0438–436, the peak of the SED is redshifted outside the window of *Fermi*/LAT observations (Punsly et al. 2018). The shift of the SED peak could be a crucial component in understanding the scarcity of the γ -ray detections of PKS 0438–436 and the lack of such detections of the remaining

FSRQs in this sample.

As mentioned in Sec. 4.1, the flux of the innermost component C4 displays an increasing trend, as shown in Fig. 4.3. This is in contrast to the decrease in flux which would be expected over time for a jet component moving away from the core as shown by the relative distance of C4 from the core in Fig. 4.4. It is possible that the proximity of C4 to the core of PKS 0438–436 creates difficulties when applying Gaussian model fit components. As the component's distance from the core increases, it is more easily recognisable as an individual component, free from the "noise" from the signal of the core component. If this were the case, the flux of the core should decrease proportionally

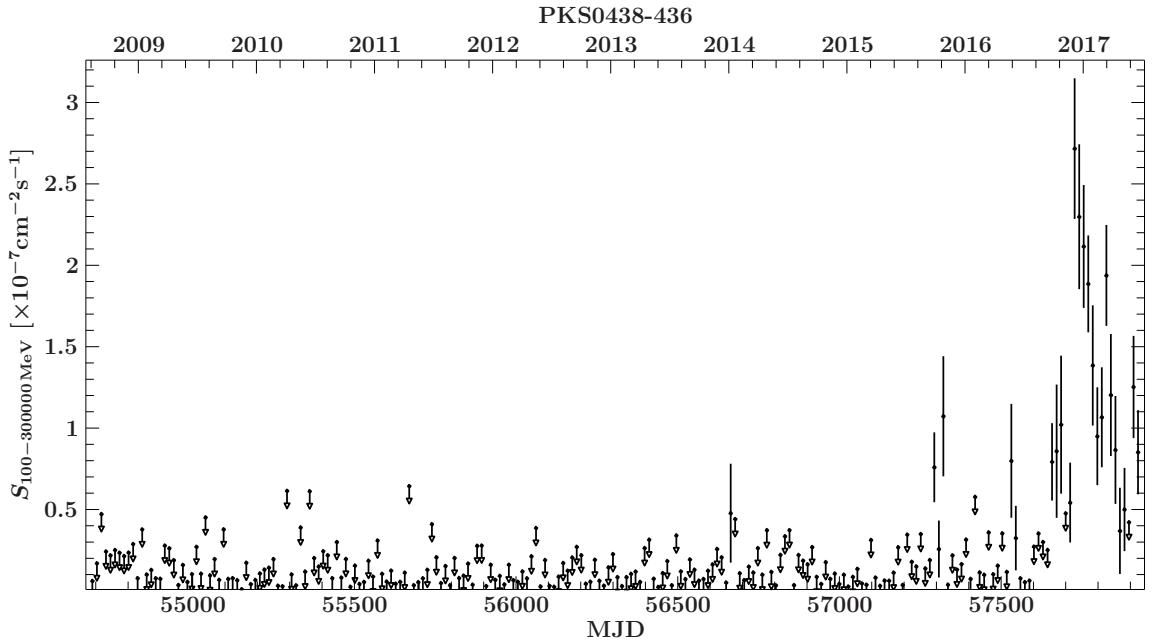


Figure 5.6.: *Fermi*/LAT Pass 8 γ -ray light curve of PKS 0438–436 over approximately nine years from 4 August 2008 to 1 July 2017 with 14-day binning. The light curve shows energies from 100 MeV to 300 GeV. Image credit: Michael Kreter.

to the increase of the flux of component C4. Since a correlation cannot be recognised solely by looking at the progression of the fluxes of the core and C4 in Fig. 4.3, further confirmation is necessary. The correlation between the two fluxes can be identified by manually increasing and "freezing" the value of the flux of the Gaussian component of the core such that it can no longer vary, leaving the flux of component C4 as a variable parameter and running `modelfit` in `DIFMAP`. For all epochs of PKS 0438–436, increasing and freezing the flux of the core component and executing twenty iterations of `modelfit` resulted in a decrease in flux of component C4, confirming the hypothesis.

Figure 5.6 shows the Pass 8 *Fermi*/LAT γ -ray light curve of PKS 0438–436 over approximately nine years. The data are from 4 August 2008 until 1 July 2017 for energies from 100 MeV to 300 GeV with 14-day binning. The strong γ -ray flare which

was detected by *Fermi*/LAT on 11 December 2016 (Cheung 2016) is clearly visible towards the right side of the light curve, with very little activity until then. Until the flare, PKS 0438–436 had not been included in any *Fermi* catalogue. By comparing the light curve of strongly flaring PKS 0438–436 with those of the remaining FSRQs in the sample, it may be possible to draw conclusions regarding the expected behaviour of PKS 1257–326, PKS 1915–458, and PKS 2106–413. By using 14-day binning, variability is visible on shorter timescales than for the remaining sources, the light curves of which have been produced using 30-day binning.

Located at a high redshift of $z = 2.863$, it is tempting to conclude that the large distance alone is what causes the rarity in γ -ray detections of PKS 0438–436. Previous to the γ -ray flare, Böck et al. (2016) analysed 75 AGN from the TANAMI sample and searched for γ -ray counterparts in the *Fermi*/LAT 1FGL catalogue. Figure 5.7 shows the redshift distribution of *Fermi*/LAT detected and undetected sources. The lines in the top panel indicate the redshift distributions of LAT detected sources in the 2LAC; the dotted line denotes AGN, the dashed line denotes BL Lacs, and the dotted line denotes quasars. The undetected source with the highest redshift is easily identifiable as PKS 0438–436, which at the time of publication, did not have an associated source in the 1FGL. Although the isolation of PKS 0438–436 in Fig. 5.7 appears to present data which supports the high redshift as a reason for lack of detection, no statistical differences were found between the redshift distributions for the population of detected sources compared to undetected sources (Böck et al. 2016). It is important to note that one of the two compared distributions only contained a small number of sources, so in spite of the lack of correlation found by Böck et al. (2016), it is possible that the high redshift of PKS 0438–436 contributed to its lack of detections at γ -ray energies.

It is evident from Fig. 5.6 that the γ -ray activity of PKS 0438–436 remained quiescent until the strong flare in 2016. The large redshift in combination with the inactivity at γ -ray energies are likely the main factors for the γ -ray history of PKS 0438–436. In addition, the high luminosity of the flare shifted the SED of PKS 0438–436 to the left, making detections by PKS 0438–436 more difficult. The possibilities to explain the behaviour of PKS 0438–436 prior to the flare remain open. Perhaps the γ -ray duty cycle had not reached an active phase until 2016, or perhaps the γ -ray emissions were either too weak or were absorbed in γ - γ interactions before reaching *Fermi*/LAT.

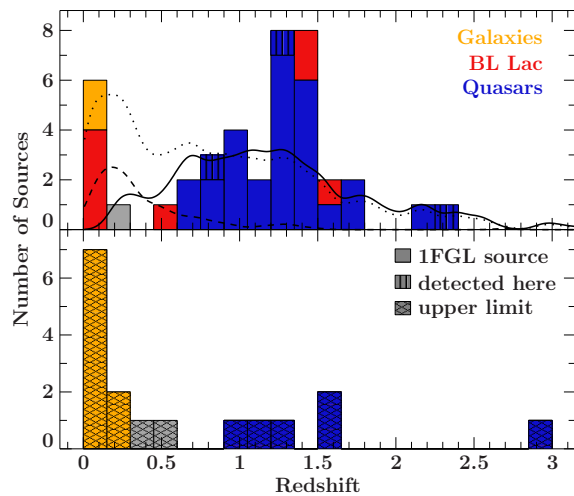


Figure 5.7.: Redshift distribution of LAT detected (top) and nondetected sources (bottom) in 2016. Image credit: Böck et al. (2016).

5.2.2. PKS 1257–326

PKS 1257–326 is one of the most rapid sources displaying radio intraday variability (Bignall et al. 2003). Figure 5.8 illustrates this variability in nine of the light curves which were produced for PKS 1257–326 over one year from 28 February 2001 until 4 January 2002 at intervals of approximately six weeks. Observations were made at 4.8 GHz, shown in black, and 8.6 GHz, shown in red. In addition to the fluctuations within each observation, it is clear that there is a drastic change in the timescale of the flux density over the course of the year.

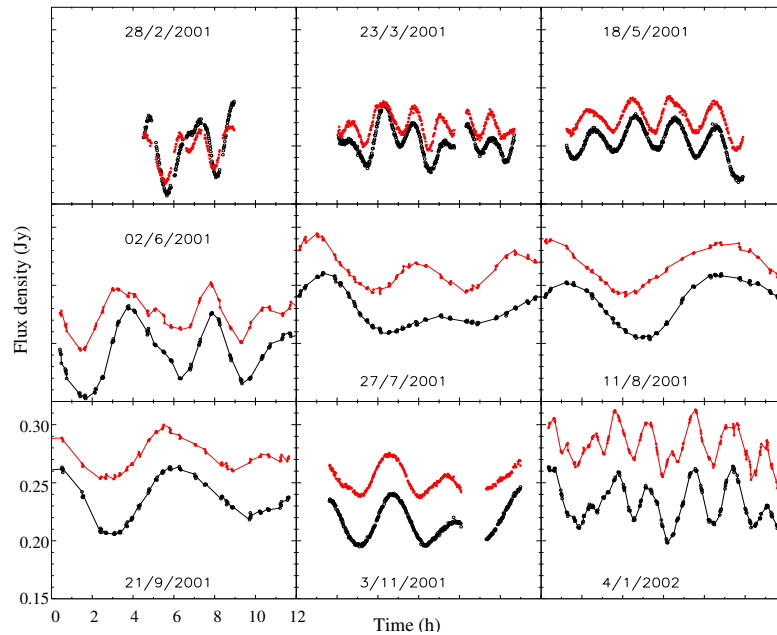


Figure 5.8.: Nine light curves produced for PKS 1257–326 over the course of one year. The scale shown on the bottom left plot applies to all light curves. Black data points represent 4.8 GHz observations and red data points represent 8.6 GHz observations. Image credit: Bignall et al. (2003).

The first few observations from February until May of 2001 display rapid variability on timescales of less than an hour. The variability slows down between June and September before accelerating again in November, eventually reaching the same rate of variability in January 2002 as was evident in February 2001. The presence of this annual cycle proves that the rapid intraday radio variability of PKS 1257–326 is caused by interstellar scintillation. As the Earth orbits the Sun, the velocity of the scattering medium relative to the observer changes, causing the changes in timescale of the flux variability of PKS 1257–326 (Bignall et al. 2003).

Furthermore, Bignall et al. (2003) identified slower flux density changes in the parsec-scale jet structures, which is typical of FSRQs (Kellermann & Pauliny-Toth 1968). These changes do not affect the microarcsecond component which is responsible for the intraday

variability. This rapid variability only applies to the brightest region of the source, not to the outer components of the jet (Bignall et al. 2003).

As shown in Fig. 4.7, the flux of the core remains fairly constant over all eight observations. Overall, the flux is fairly weak, with a maximum core flux of 0.15 Jy in epoch V252F. The total flux of the source (printed on the individual images in Appendix A) decreases minimally from 0.17 Jy to 0.14 Jy over the eight observations. The slight deviations in the flux of the core and the components C2 and C3 must not be over-interpreted; the error bars on the flux densities are set at a very optimistic 20% for calibration and imaging errors. Additionally, due to the enormous discrepancy in angular resolution of the images from different epochs, it is crucial to remain critical of any small apparent fluctuations. Epoch V252AE is an extreme example, but the angular resolution also varies dramatically between epochs V252I and V252N, making it difficult to draw conclusions regarding the minimal variations in flux or brightness temperature of PKS 1257–326.

Figure 5.9 shows the Pass 8 γ -ray light curve of PKS 1257–326 over ten years from 4 August 2008 to 4 August 2018. The light curve is constructed with time bins of 30 days for energies from 100 MeV to 300 GeV. With the exception of two outliers, one occurring just before MJD 57000 and the other just after MJD 58000, there is very little γ -ray activity to be seen. There is no clear detection of γ -ray emissions from PKS 1257–326. The analysis of this new light curve yielded a test statistic $TS = 9$, which corresponds

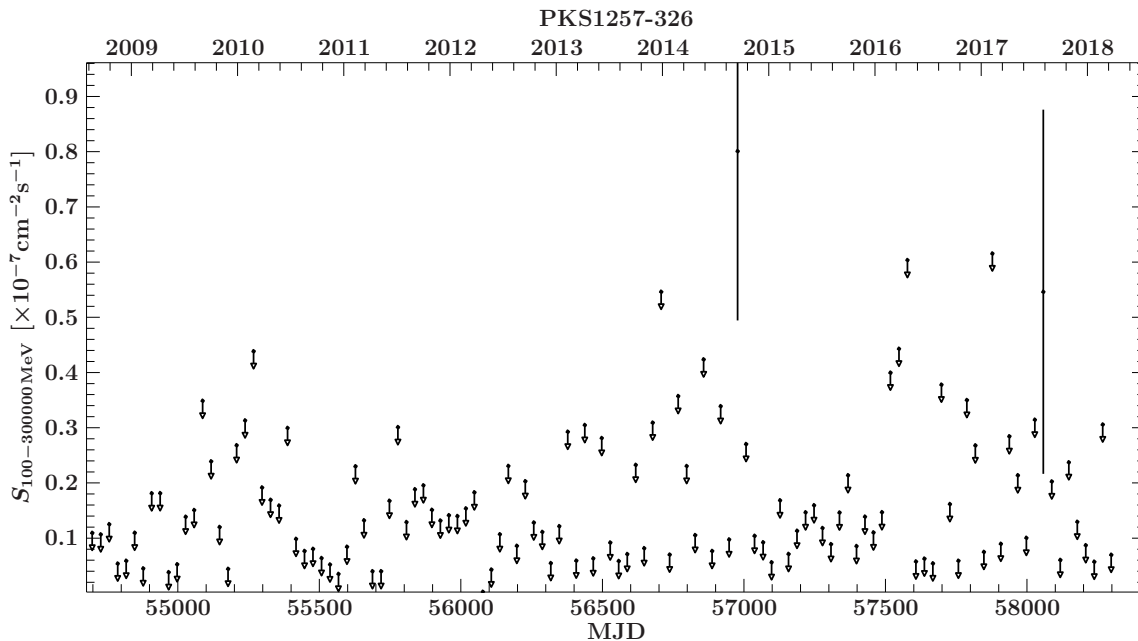


Figure 5.9.: *Fermi*/LAT Pass 8 γ -ray light curve of PKS 1257–326 over ten years from 4 August 2008 to 4 August 2018 with 30-day binning. The light curve shows energies from 100 MeV to 300 GeV. Image credit: Michael Kreter.

to approximately a 3σ level of significance. Levels of 3σ are not particularly meaningful, since signals of such significance can also be caused by random fluctuations in flux.

An initial comparison of PKS 1257–326’s light curve to that of PKS 0438–436 prior to the flare does not show any large differences; the flux of both tends to hover below $0.5 \cdot 10^{-7} \text{ cm}^{-2}\text{s}^{-1}$, with a couple of instances of higher flux. However, when comparing the total radio flux of PKS 1257–326 to that of PKS 0438–436, there is a difference of almost a factor of 10. PKS 0438–436’s maximum total flux is 1.4 Jy compared to 0.17 Jy for PKS 1257–326. Since the total radio flux of PKS 1257–326 is so weak in general, it is likely that this is this main reason for the lack of detections at γ -ray energies until now. It cannot be ruled out that the γ -ray duty cycle of PKS 1257–326 has not yet been active, and may still be detected in a period of high γ -ray activity.

5.2.3. PKS 1915–458

The most interesting feature of PKS 1915–458 is the extremely fast apparent speed of the jets. As stated in Sec. 4.3, the components C2 and C3 of PKS 1915–458 display apparent speeds in excess of $100c$. In general, at least five observations must be considered in order to reach a conclusion regarding the apparent superluminal motion of a jet. The calculated value of $\beta_{\text{app}} = (180.416 \pm 0.626)c$ for C2 must not be taken too earnestly; there are only three epochs in which this component can be identified and fitted with a Gaussian component. The value of $\beta_{\text{app}} = (101.265 \pm 3.811)$ for C3 has been calculated from four observation epochs. After the first clean images of PKS 1915–458 were produced according to Sec. 3.2.1, it was clear from the morphology that the apparent velocity of the jet were extremely fast. It is a well-known problem in differential mapping with DIFMAP that errors can easily be made during the imaging and model-fitting procedures, requiring a very critical eye when analysing jet kinematics. Since the erroneous imaging of imaginary features cannot be completely ruled out, several attempts were made to try to "force" a series of images and models which would yield a slower value for the apparent superluminal motion. These attempts were unsuccessful, producing convincing a time evolution plot for PKS 1915–458, supported by the development of the brightness temperature and flux of the components as shown in Figs. 4.10 and 4.11. Both parameters behave exactly as would be expected, decreasing rapidly as the components move away from the core. Evidence from the four available observations will be discussed, but further observations are vital in order to confirm or question the remarkable velocity of PKS 1915–458’s jet.

As mentioned in Sec. 4.3, the first piece of evidence supporting the initial kinematics analysis of PKS 1915–458 is the appearance of component C4 in epoch V252AL. Although it is possible that the component was already present in epoch V252AF but was located too close to the core to be identified, the flux of the core as plotted in Fig. 4.3 would also be affected in this scenario. Similar to the effect visible in the flux of the core component as discussed for PKS 0438–436, the flux of the core component of the jet would be expected to decrease from V252AF to V252AL. The unchanged flux

of the core component over the last two observation epochs indicates that the original inference is the most likely, yielding a minimum proper motion consistent with that of the other components of PKS 1915–458. It is also possible that C4 first appeared much closer to the observation of V252AL than to that of V252AF, which would correspond to an even faster apparent motion. This speculation is tenuous, since there is only one observation epoch in which C4 can be identified and fitted with a Gaussian component.

Another consideration as to what could exaggerate the apparent superluminal motion of PKS 1915–458 is the fact that the redshift $z = 2.47$ has not been confirmed. This redshift was obtained via personal communications with N. Tasker (Jackson et al. 2002). A change in the value of the redshift for PKS 1915–458 would also affect the apparent superluminal motion. Figure 5.10 shows the distribution of proper motion μ for the fastest component of the 110 highest quality sources included in the study of the parsec-scale structures of radio jets by Kellermann et al. (2004). The solid line represents μ_{\max} which is the fastest proper motion a source with $\gamma = 25$ can display and corresponds to a maximum apparent velocity of $\beta_{\text{app}} \sim 25c$. The uncertainty in redshift is most likely trivial in the case of PKS 1915–458, since the slope of the curve becomes relatively flat for redshifts above $z = 1.5$. However, referring to Fig. 5.10 presents another conundrum, since high values of μ are only seen in sources with small redshifts, and the proper motion $\mu = 1.106 \pm 0.042 \text{ mas/yr}$ of C2, the most conservative of the imaged components, is more than double the value of the proposed upper boundary for the given redshift of PKS 1915–458.

The apparent superluminal motion of PKS 1915–458 becomes more intriguing when the published findings regarding the relationship of the apparent jet speed to γ -ray detections of AGN are considered. Kellermann et al. (2004) established that for a representative sample of AGN, those detected at γ -ray energies by EGRET have faster jet speeds with a median apparent speed of $(8.0 \pm 1.6)c$ when compared to those not detected by EGRET, with a median apparent speed of $(3.9 \pm 1.1)c$. This strengthened the hypothesis that the radio emission produced by γ -ray detected sources is more strongly beamed than for the remaining radio quasar population. Lister et al. (2009) analysed this relationship more closely, studying the connection between the apparent speeds of VLBA jets and their γ -ray detections by *Fermi*/LAT. A significant difference was established between the speed distributions of *Fermi*/LAT detected and nondetected quasars

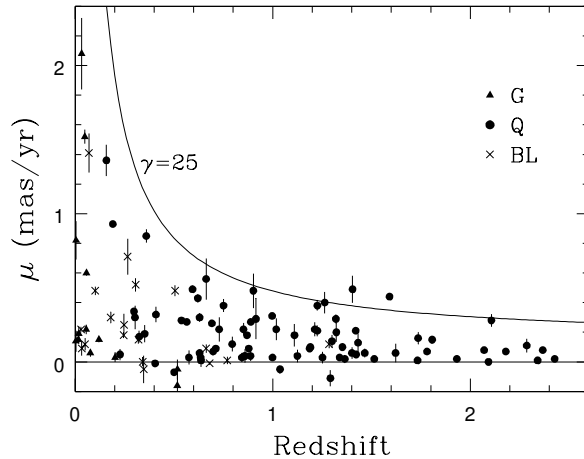


Figure 5.10.: The $\mu - z$ diagram displaying the distribution of the fastest component of 110 sources. The solid line marks the maximum value of β_{app} for $\gamma = 25$. Image credit: Kellermann et al. (2004).

from the MOJAVE sample. The nineteen *Fermi*/LAT detected quasars had a peak at $\beta_{\text{app}} \sim 10 - 15c$, while the nondetected quasars peaked below $5c$.

Lister et al. (2015) conducted a study of the γ -ray detections of AGN in the MOJAVE sample, the findings of which were consistent with those of the two previously mentioned papers. Figure 5.11 shows the apparent jet speed plotted against the peak frequency of the synchrotron component in the rest frame. The open red circles, representing the MOJAVE sources not detected by *Fermi*/LAT, are gathered in the lower left corner, corresponding to low apparent jet speeds and low synchrotron peak frequencies. The apparent superluminal motion of PKS 1915–458 appears to be an exception to the pattern which has been established over a series of papers, making its exclusion from *Fermi* catalogues even more fascinating.

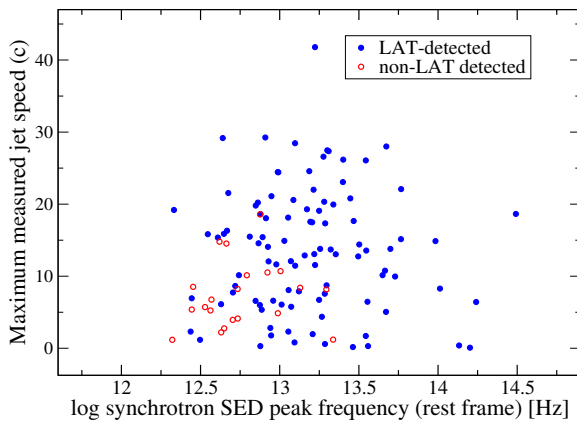


Figure 5.11.: The maximum jet speed is plotted against the rest frame synchrotron SED peak frequency. Sources which have been detected by *Fermi*/LAT are plotted with blue filled circles. Sources which remain undetected at γ -ray energies by *Fermi*/LAT are plotted with open red circles. Image credit: Lister et al. (2015).

PKS 0438–436, which measured a daily averaged flux for $E > 100$ MeV of $(1.1 \pm 0.2) \cdot 10^{-6}$ photons $\text{cm}^{-2}\text{s}^{-1}$, almost three times stronger (Cheung 2016).

However, the overall radio flux of PKS 1915–458 is also much weaker than that of PKS 0438–436, with a maximum total flux of 0.31 Jy, less than one third of the maximum total radio flux measured for PKS 0438–436. Since the period of higher activity in 2010, no further clear γ -ray detections have been made of PKS 1915–458. There are two noticeable instances of possible higher activity in 2014 and 2017, neither of which is as strong as the activity in 2010. The test statistic for this source is $\text{TS} = 9$, which corresponds to a significance level of 3σ , as for PKS 1257–326. The behaviour of PKS 1915–458 can most likely be described similar to that of PKS 1257–326 - the total emissions are not particularly strong, leading to a lack of further detections since the

Figure 5.12 shows the Pass 8 γ -ray light curve of PKS 1915–458 over ten years from 4 August 2008 to 4 August 2018. The light curve is constructed with time bins of 30 days for energies from 100 MeV to 300 GeV. A source positionally consistent with PKS 1915–458 was detected during a flare by *Fermi*/LAT in 2010 (Sokolovsky et al. 2010). Immediately after this detection, *Swift* performed a Target of Opportunity observation, detecting an X-ray source which was also positionally consistent with PKS 1915–458. The region of higher γ -ray activity can be seen on the left of Fig. 5.12, corresponding to the date of the *Fermi*/LAT and *Swift* detected flare. The strength of the flare was measured for $E > 100$ MeV as $(0.36 \pm 0.15) \cdot 10^{-6}$ photons $\text{cm}^{-2}\text{s}^{-1}$ (Sokolovsky et al. 2010), much weaker than the flare of

initial flare in 2010. Further research is necessary to determine the apparent velocity of PKS 1915–458’s jet and the influence of the apparent velocity on γ -ray detectability.

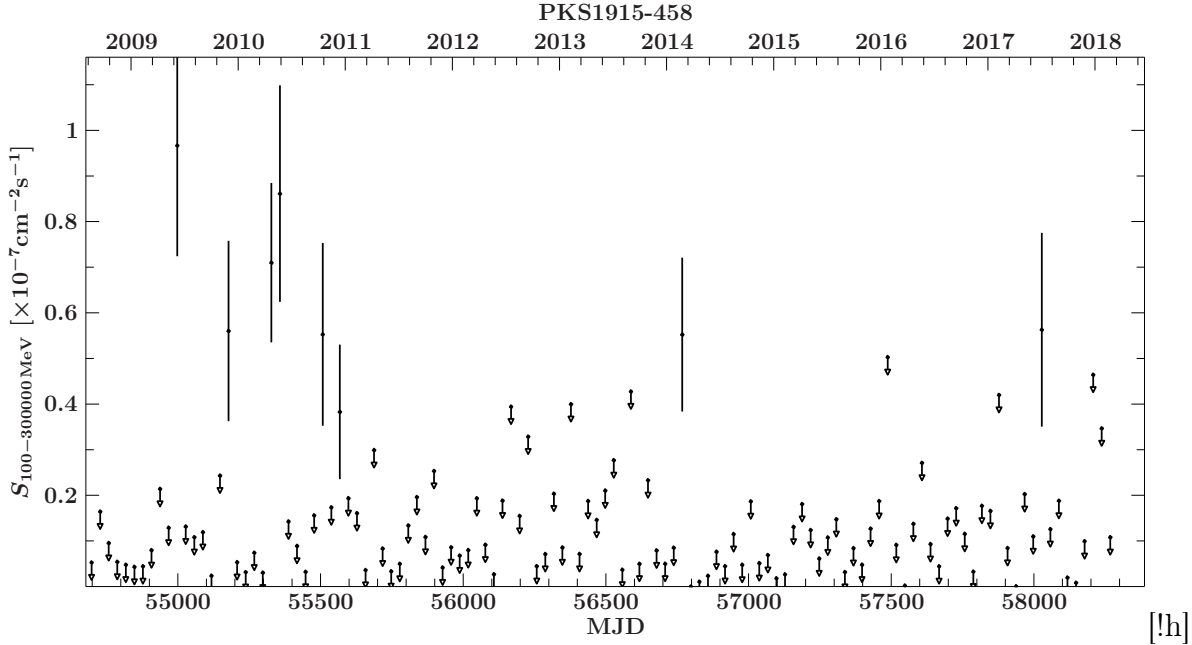


Figure 5.12.: *Fermi*/LAT Pass 8 γ -ray light curve of PKS 1915–458 over ten years from 4 August 2008 to 4 August 2018 with 30-day binning. The light curve shows energies from 100 MeV to 300 GeV. Image credit: Michael Kreter.

5.2.4. PKS 2106–413

The most interesting aspect of PKS 2106–413 is the complex inner structure of the jet. With Gaussian model fitting components present on two sides of the jet’s core, the jet of PKS 2106–413 appears to be emitted initially to the west with component C2 located consistently at an angle of $\sim -90^\circ$ before bending through the line of sight to the core with the next component C6 positioned at an angle of $\sim 100^\circ$. Both of these components remain fairly stationary, as shown in Fig. 4.16. von Montigny et al. (1995) presented findings regarding the influence of jet bending on γ -ray detections of FSRQs by EGRET, stating that jet bending on parsec- or kiloparsec-scales could be responsible for beaming γ -emission away from the light of sight. If the γ -rays are produced in an inner region of the jet in which the bulk Lorentz factor is larger than in the radio emission region, high-energy γ -ray emission could also be beamed more narrowly than emissions at radio energies. Tingay et al. (1998) quantitatively investigated the suggestion made by von Montigny et al. (1995), finding evidence that jet bending in parsec-scale radio jets is correlated to the γ -ray detection. The γ -ray-quiet AGN within the sample had larger

and more bends than those which had been detected by EGRET. Caution was advised, however, since observational biases could not be ruled out for the small samples.

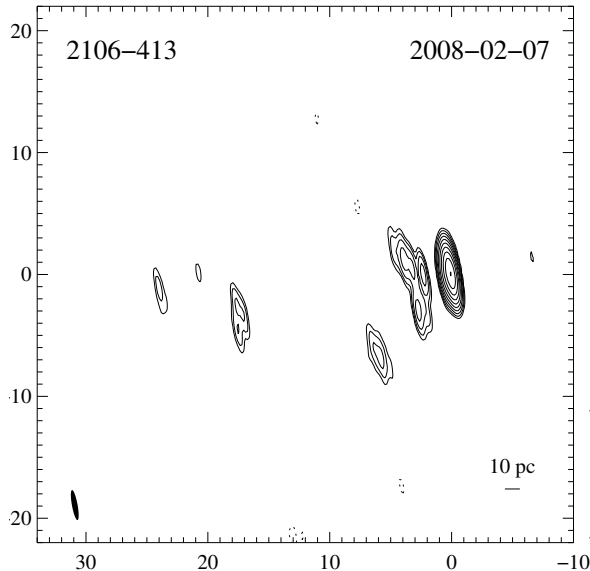


Figure 5.13.: Clean map of PKS 2106–413 at 8.4 GHz. The scale is in mas, with the size of the FWHM of the Gaussian restoring beam as a black ellipse in the bottom left corner. The contours are set as for all other images in this work. Image credit: Ojha et al. (2010).

Graham & Tingay (2014) further investigated this correlation with surprising results, including PKS 2106–413 in the sample to investigate the hypothesis that the jets of γ -ray-quiet AGN are more likely to display jet bending. Using a large sample of 351 radio-loud AGN with data from *Fermi*/LAT, no connection was found between jet bending and γ -ray detectability, in contrast to the results of the two previously mentioned papers. This discrepancy highlights the dependence of jet bending measurements on the quality and resolution of the VLBI images.

As mentioned in Sec. 4.4, Graham & Tingay (2014) identified PKS 2106–413 as having a total of $N = 0$ jet bends with a maximum bending angle of 0° . However, the morphology of PKS 2106–413 visible in the images produced in the scope of this thesis is not consistent with these findings. In order to understand this discrepancy, it was necessary to compare the pre-existing images with those produced for this thesis. Of the data used by Graham & Tingay (2014), the highest resolution and best image was from Ojha et al. (2010), as shown in Fig. 5.13. This clean map of PKS 2106–413 was presented as part of the first series of 8.4 GHz images produced with the data from the first epoch of observations by TANAMI. When compared to the individual images of PKS 2106–413 in Appendix A.4, it is clear that the more detailed inner structure of the images produced within the scope of this thesis is not present in Fig. 5.13. An older image from the VSOP 5 GHz survey by Fomalont et al. (2000) was included among the additional data used by Graham & Tingay (2014) to determine the jet bending parameters. Despite the milliarcsecond resolution, in this image, PKS 2106–413 presents as a featureless point source with little to no jet structure visible.

As for PKS 1915–458, critical imaging and re-imaging was carried out with DIFMAP for PKS 2106–413 to rule out the possibility of erroneously imaged features in the structure of PKS 2106–413’s jet. Attempts to produce clean maps without the presence of components to the west of the core were unsuccessful. The presence of a feature to the west of the core in every epoch, despite attempts to actively ignore it while imaging, leads to the conclusion that the jet of PKS 2106–413 does in fact bend. Although this

is an interesting characteristic of PKS 2106–413 it is not clear whether the jet bending influences the γ -ray detections.

As mentioned in Sec. 4.4, the brightness temperature of C2 displays interesting behaviour as shown in Fig. 4.14. The unusual fluctuations of C2’s brightness temperature are likely due to its proximity to the core of the jet, combined with dramatic differences in resolution between images from different epochs. The perplexing sudden jump in the flux of component C3 as seen in Fig. 4.15 should not be overinterpreted; the errors on the flux are a conservative 20% and the parameters of component C3 are not robust, meaning that no conclusions can be drawn based on the three epochs in which C3 can be identified and fitted with a Gaussian component.

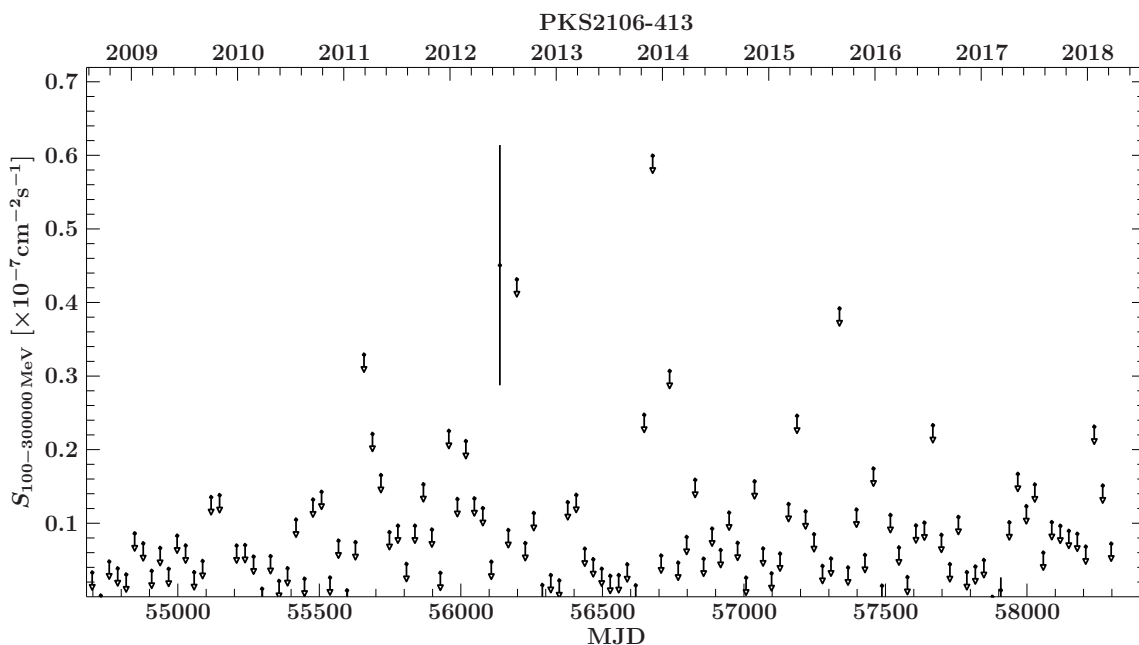


Figure 5.14.: *Fermi*/LAT Pass 8 γ -ray light curve of PKS 2106–413 over ten years from 4 August 2008 to 4 August 2018 with 30-day binning. The light curve shows energies from 100 MeV to 300 GeV. Image credit: Michael Kreter.

Figure 5.14 shows the Pass 8 γ -ray light curve of PKS 2106–413 over ten years from 4 August 2008 to 4 August 2018. The light curve is constructed with time bins of 30 days for energies from 100 MeV to 300 GeV. This light curve also yielded a test statistic $TS = 9$, corresponding to a 3σ significance. This significance, as previously mentioned for PKS 1257–326 and PKS 1915–458, is not conclusive, since such signal levels can also be produced by random fluctuations. PKS 2106–413 is neither noticeably weak in flux nor especially far away, located at $z = 1.058$, ruling out two of the possible reasons for the lack of detections at γ -ray energies. Perhaps the γ -ray duty cycle has not yet entered a period of activity, or perhaps there is indeed a correlation between the jet bending of an FSRQ and its detectability by *Fermi*/LAT.

5.3. Conclusions

After extensive analysis of the TANAMI radio data and detailed consideration of the characteristics of each source, the remarkable γ -ray quiescence of the four FSRQs included in the scope of this thesis can be explained by one or a combination of the possibilities listed above. PKS 0438–436, which exhibited a strong flare in 2016, has an otherwise unremarkable light curve. This leads to the inference that the γ -ray activity of PKS 0438–436 was not strong enough to be detected prior to the flare. This quiescence could be caused by a number of factors, including the high redshift, the γ -ray duty cycle, or γ - γ absorption either in the BLR or the EBL. Additionally, the high luminosity of PKS 0438–436 could cause the γ -ray peak of its SED to be shifted out of the window of observation for *Fermi*/LAT. PKS 1257–326, which displays fast intraday radio variability, is generally very weak in terms of the flux density of the radio emissions analysed in this work. This indicates that the emissions of this FSRQ, including γ -ray emissions, are overall too weak to have been detected by *Fermi*/LAT. The jet of PKS 1915–458 displays superluminal motion of the order of $100c$, which makes its γ -ray quiescence particularly interesting, since sources which exhibit faster jet speeds are more likely to be detected at γ -ray energies. However, PKS 1915–458's high redshift and relatively weak flux density at radio energies may help to explain the lack of detections. Since only four observations were available, further analysis of PKS 1915–458 is necessary to draw conclusions regarding the apparent jet speed and the connection to γ -ray quiescence. The morphology of PKS 2106–413 is surprisingly complex, clearly displaying a jet which bends through approximately 180° . Although the presence of bends in a jet has not yet been found to have an effect on the γ -ray detections, higher resolution images must be studied more extensively to investigate this possible connection.

6. Summary & Outlook

The sample of AGN targeted by TANAMI observations consists of bright, compact sources. In 2008, observations with *Fermi*/LAT made it apparent that many of the TANAMI sources are also detectable at γ -ray energies. However, not all of the sources in the TANAMI catalogue have been included in any *Fermi*/LAT catalogue. There are four main factors which, alone or in combination with each other, could be responsible for the lack of γ -ray detections from some of these sources.

The first consideration is that the lack of γ -ray detections is caused by a high redshift. The further away an object is from the Earth, the more time and space is available for the γ -rays to interact with and be absorbed by the EBL. The second possibility is that the entire spectral energy distribution of a source is redshifted due to high luminosity, shifting the Compton peak to the left. The γ -ray spectrum also becomes steeper because of this, which corresponds to weak emissions above a certain energy which remain as yet undetected by any γ -ray instruments. The next plausible factor in determining γ -ray detectability is γ - γ absorption and pair production with photons in the BLR. It is important to remember that γ -ray-quiet is not equivalent to γ -ray-silent; the fourth possibility is that the source is overall too weak and has not yet reached the detection threshold for *Fermi*/LAT or other γ -ray instruments, either because the flux is generally too weak, or perhaps because the γ -ray duty cycle has not yet undergone a phase of high activity.

In order to better understand what affects the γ -ray detectability of FSRQs, the VLBI data collected by TANAMI at 8.4 GHz of four sources were studied. Through an observational approach with careful consideration of the scientific background, each AGN was analysed and its behaviour could be explained by one or more of the aforementioned possibilities.

First, the AIPS calibrated VLBI data of each FSRQ were processed with DIFMAP, producing a "clean" image for each epoch. A self-consistent multi-epoch model of elliptical Gaussian components was developed to describe the kinematics of the jet and parameters of the components. Depending on the appearance of unusual or unexpected characteristics, this process was sometimes executed several times to test the validity and stability of the self-consistent model. Based on morphology, kinematics and characteristic parameters such as flux and brightness temperature, the following conclusions were drawn:

PKS 0438–436 is the FSRQ with the largest redshift of $z = 2.856$ and the strongest γ -ray emissions out of the sample included in the scope of this work. Although no

direct correlation has been found between redshift and γ -ray detectability, it is possible that this contributed to the lack of detections prior to the flare in 2016. Additionally, PKS 0438–436 displayed such high luminosity while flaring that the Compton peak of the SED was shifted outside the window of *Fermi*/LAT observations (Punsly et al. 2018). As for the γ -ray activity before the flare, more than one factor could have played a role in the ostensible quiescence of PKS 0438–436.

PKS 1257–326 displays radio intraday variability on timescales as short as 45 minutes (Bignall et al. 2003). The dramatic difference in resolution between images from different epochs made the imaging and subsequent analysis of PKS 1257–326 somewhat challenging. Morphologically, PKS 1257–326 does not display any unusual traits. Overall, the radio emissions of this source are quite weak. The low flux of radio emissions from PKS 1257–326 indicate that until now, the γ -ray emissions have probably remained below the detection threshold level and may be detected in the future.

PKS 1915–458 only has four observations available for analysis. The most intriguing feature is the apparent superluminal motion of PKS 1915–458’s jet at enormous speeds. Not only is this a fascinating characteristic on its own, it becomes even more compelling when combined with the lack of γ -ray detections, since it has been shown by Kellermann et al. (2004); Lister et al. (2009) and Lister et al. (2015) that FSRQs with fast superluminal jets are more likely to be detected at γ -ray energies than their slower counterparts. PKS 1915–458 was detected during one period of higher γ -ray activity in 2010, but has not been detected since then (Sokolovsky et al. 2010). Since the data from only four observation epochs were available at the time of this thesis, it is difficult to draw any conclusions regarding the accuracy of the kinematics analysis and its correlation to the γ -ray detectability.

PKS 2106–413 is unique in this sample of FSRQs because of the morphology of the inner structure of the jet. PKS 2106–413’s jet appears to be emitted to the west, curving back across the field of view to the jet core before continuing in a south-easterly direction. Although Graham & Tingay (2014) established that jet bending has no effect on γ -ray detectability, the inner structure of PKS 2106–413 with its dramatic bend over 180° was not recognised and as such, cannot possibly have been considered in connection with its lack of γ -ray detections. Further studies of high-resolution data are necessary to determine whether jet bending also plays a role in the γ -ray detectability of FSRQs.

Following meticulous analysis of the TANAMI radio data and comprehensive consideration of the characteristics of the four FSRQs considered in the scope of this thesis, the observed behaviour of each of these four sources can largely be explained by one or more of the hypotheses for γ -ray quiescence. The high luminosity, high redshift, and γ -ray duty cycle could all be factors in explaining the quiescence of PKS 0438–436 prior

to the detection of its flare. PKS 1257–326 exhibits weak radio emissions, leading to the inference that its emissions are generally too weak to have been detected. In the cases of PKS 1915–458 and PKS 2106–413, further research is crucial to further investigate the correlation between γ -ray emissions and superluminal motion and jet bending, respectively.

A. Individual Images of all sources

The following images have been produced using DIFMAP and ISIS . The observation date is printed in the top right corner of each image. The values of the peak flux S_{peak} , noise σ_{noise} and the total flux S_{tot} are also given within the plots. The contours are set such that the first contour represents a 3σ noise level with the following contours increasing logarithmically with by a factor of two. The size of the restoring beam is shown as a grey ellipse in the bottom left corner of each image. The images are ordered chronologically from left to right, top to bottom.

A.1. Individual Images of PKS 0438–436

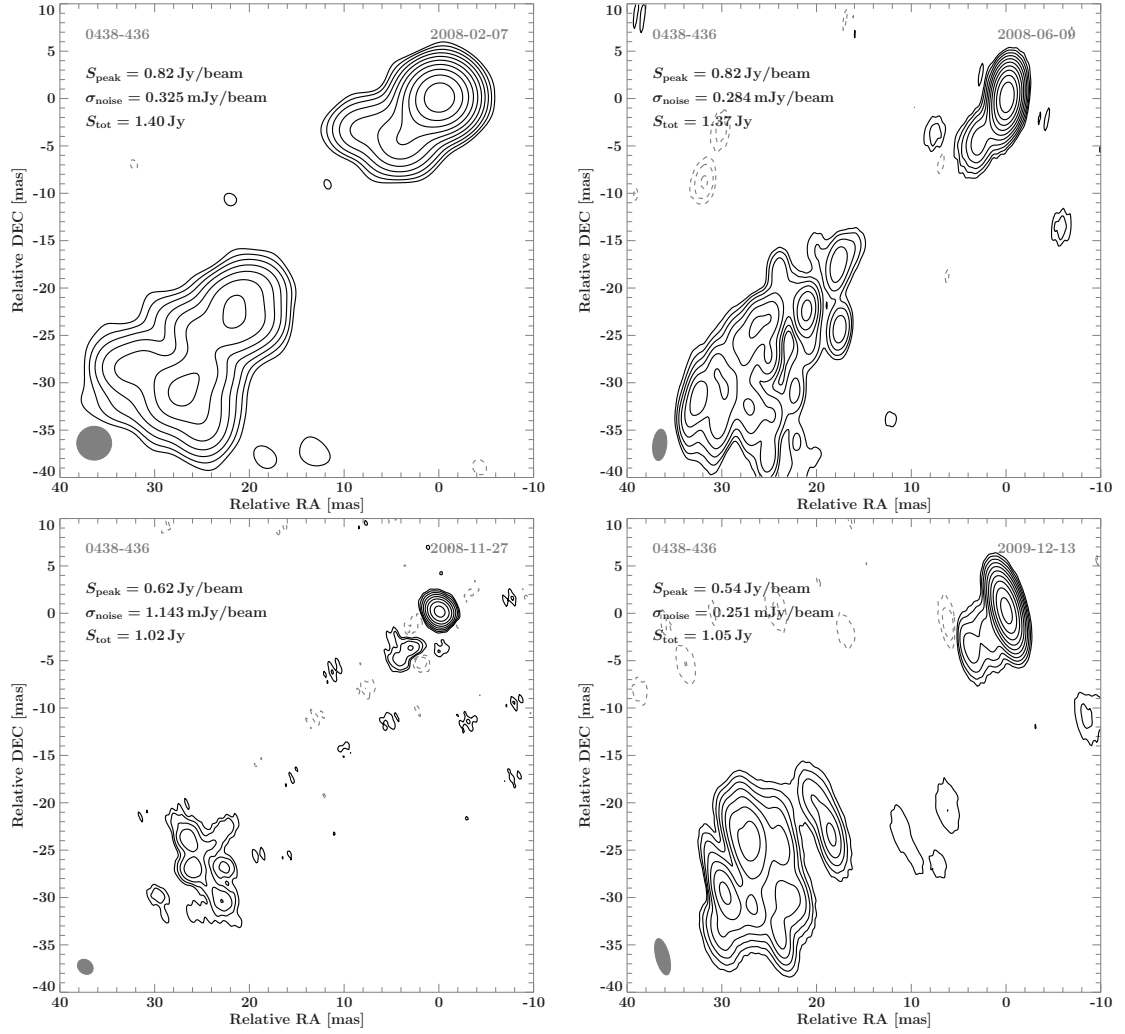
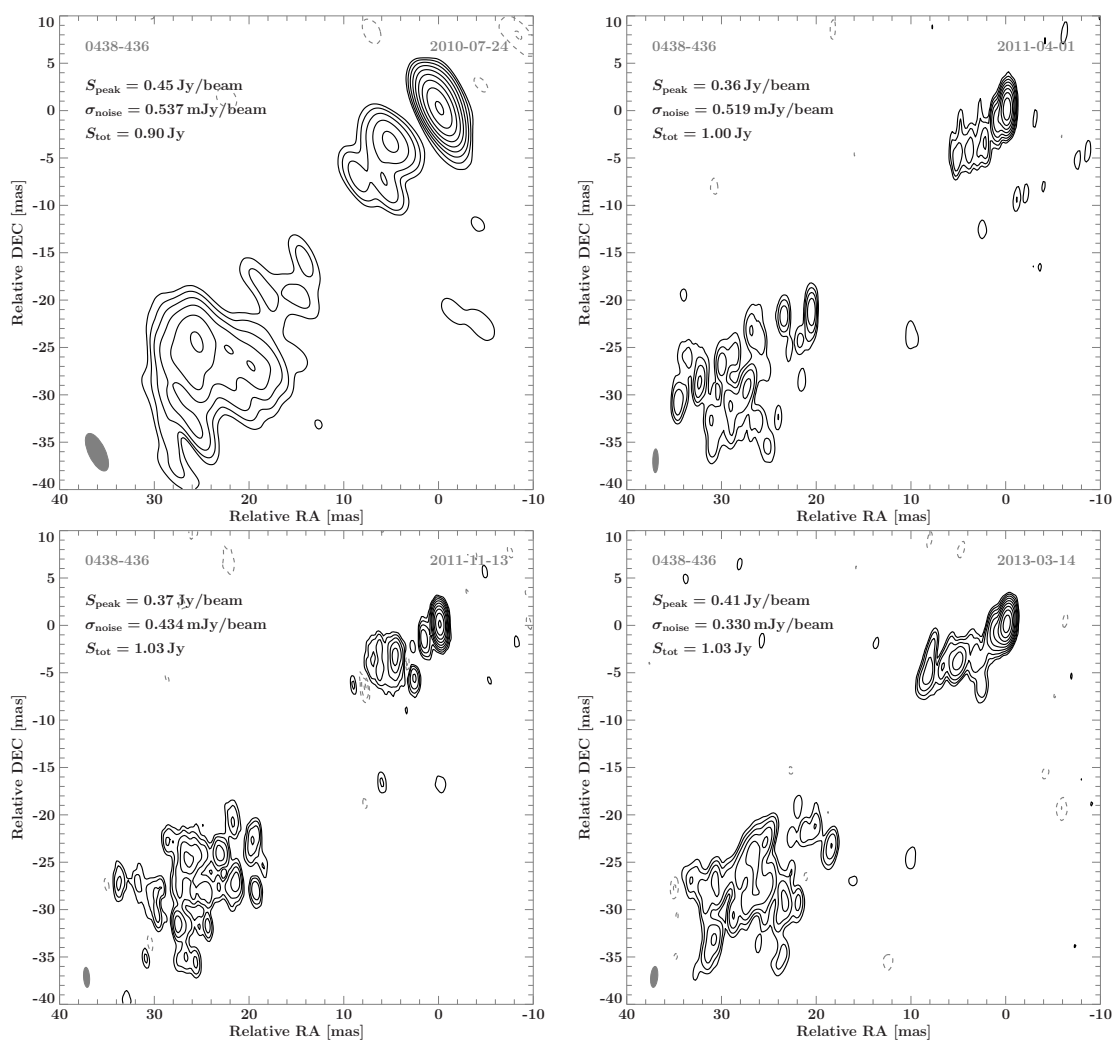


Figure A.1.: Clean maps of PKS 0438–436 (continued on next page).

A.1. Individual Images of PKS 0438–436



(Continued from previous page) Clean maps of PKS 0438–436.

A. Individual Images of all sources

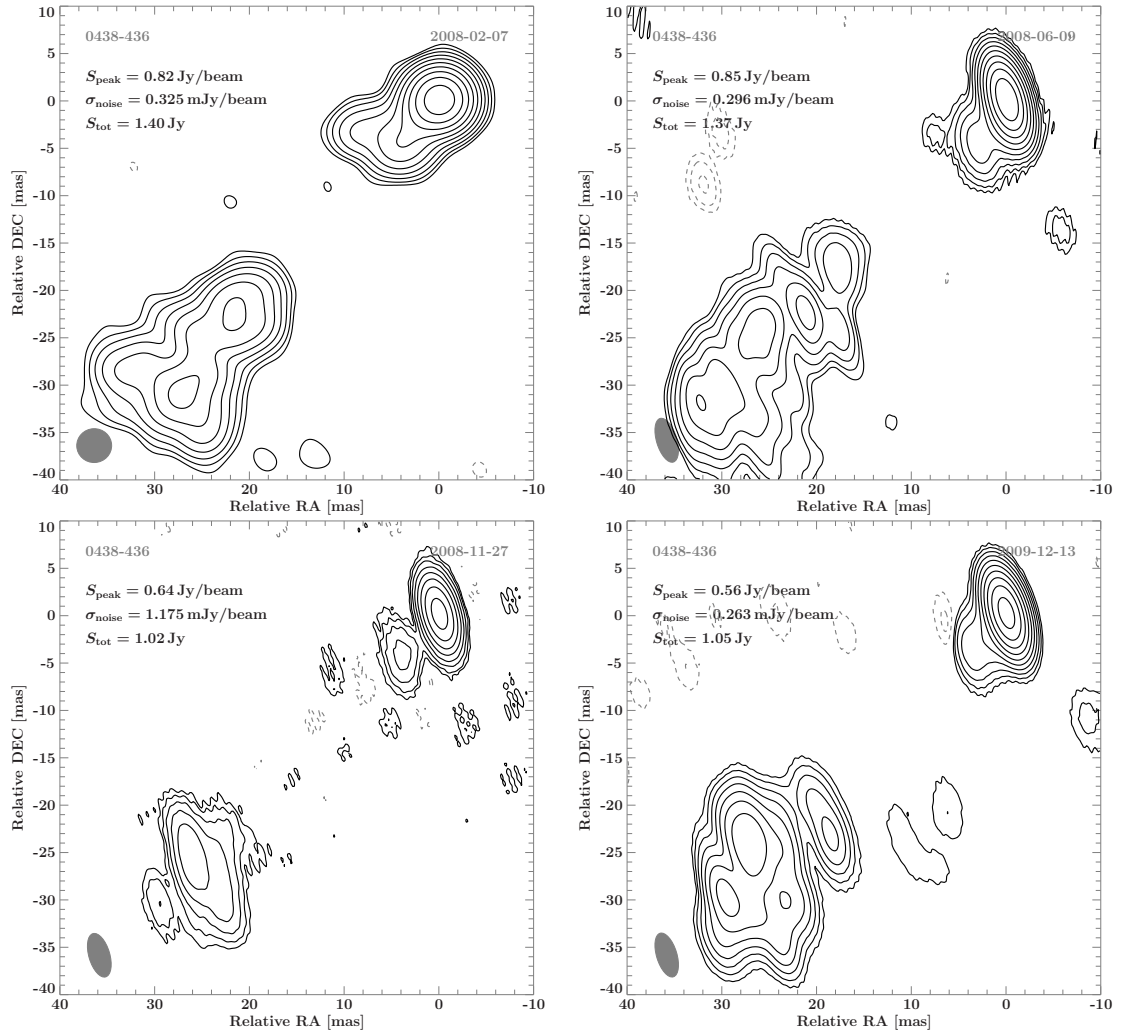
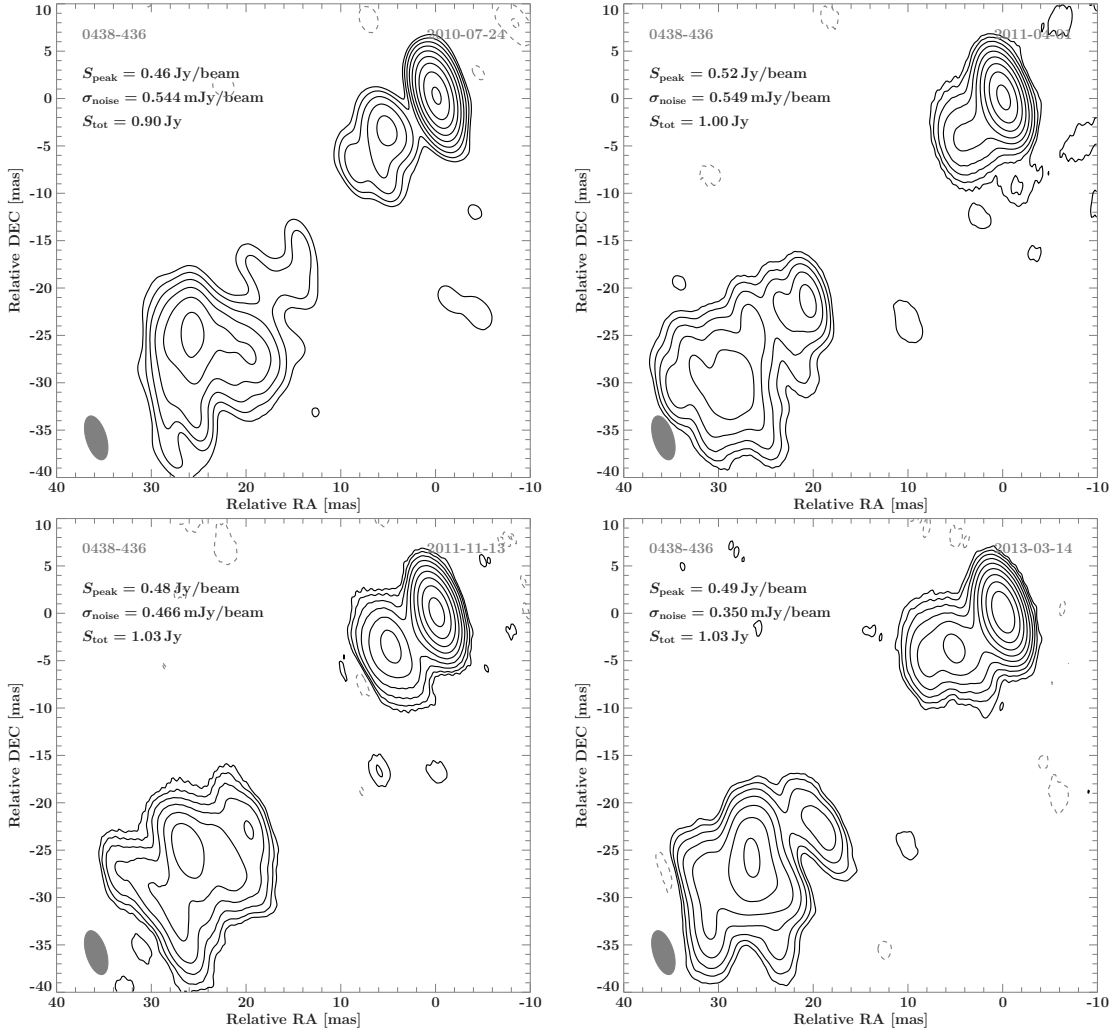


Figure A.2.: Clean maps of PKS 0438–436 restored using the beam size from epoch V252F, with the exception of epoch V252C (continued on next page).

A.1. Individual Images of PKS 0438–436



(Continued from previous page) Clean maps of PKS 0438–436 restored using the beam size from epoch V252F, with the exception of epoch V252C.

A.2. Individual Images of PKS 1257–326

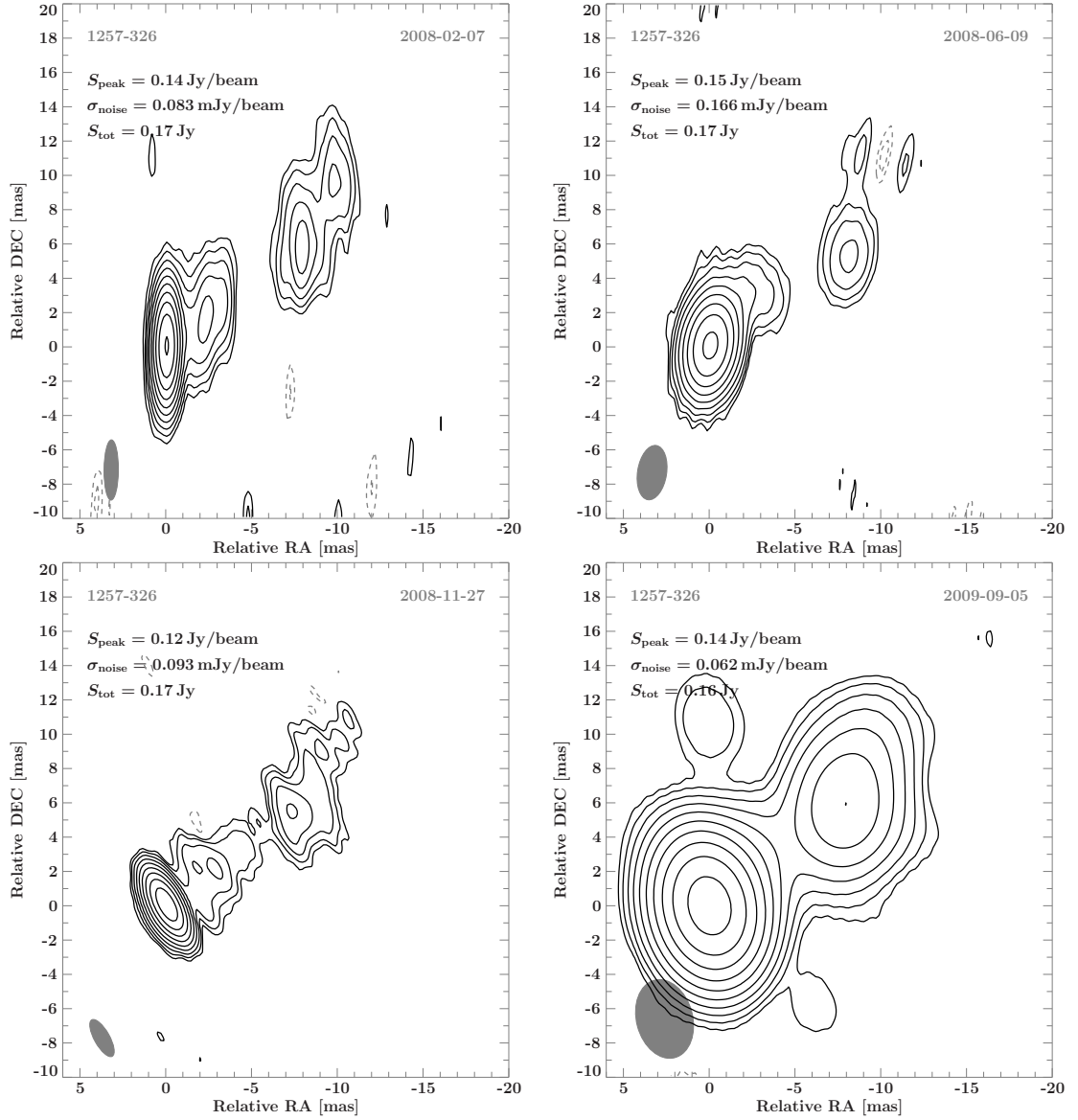
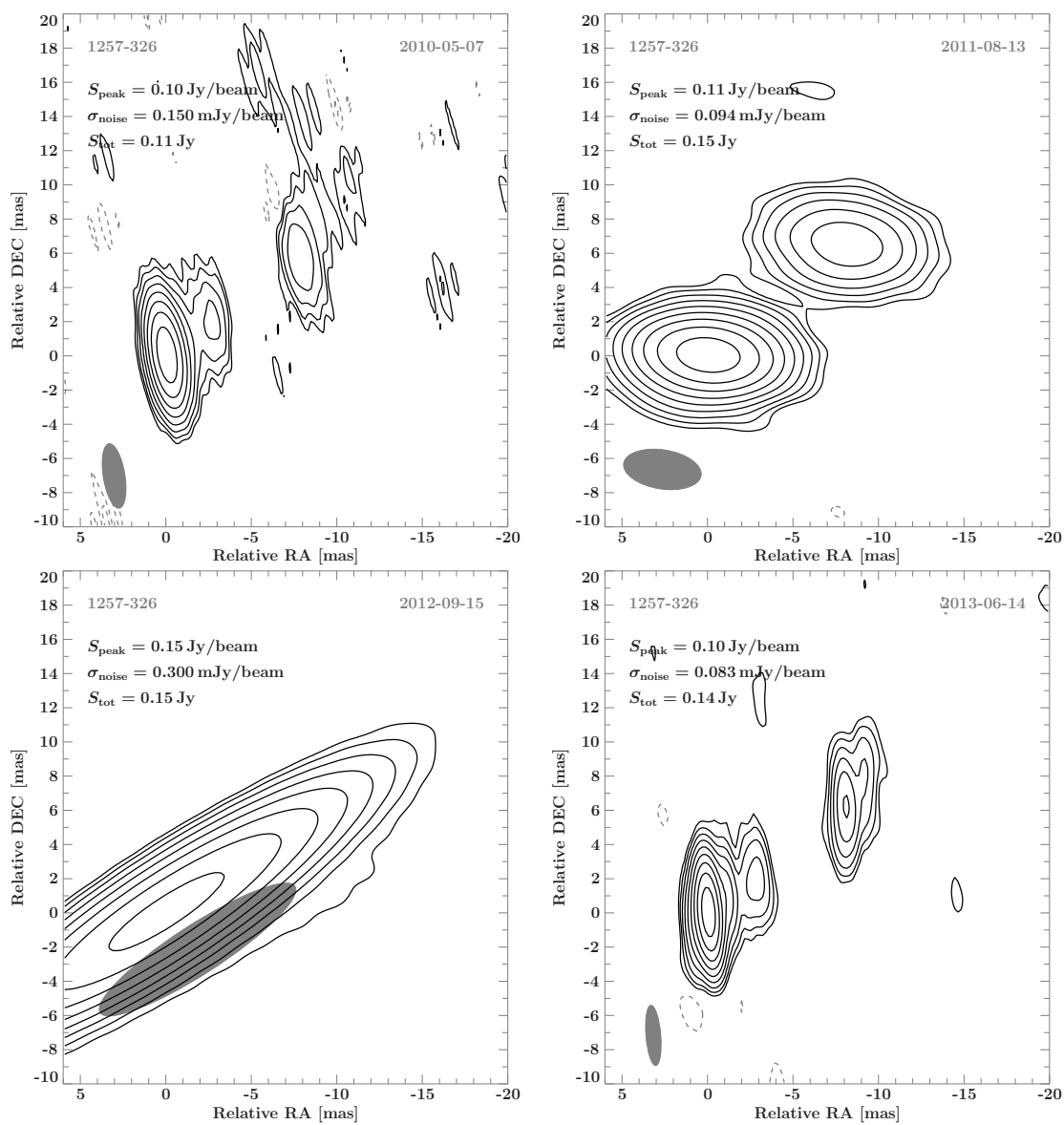


Figure A.3.: Clean maps of PKS 1257–326 (continued on next page).



(Continued from previous page) Clean maps of PKS 1257–326.

A.3. Individual Images of PKS 1915–458

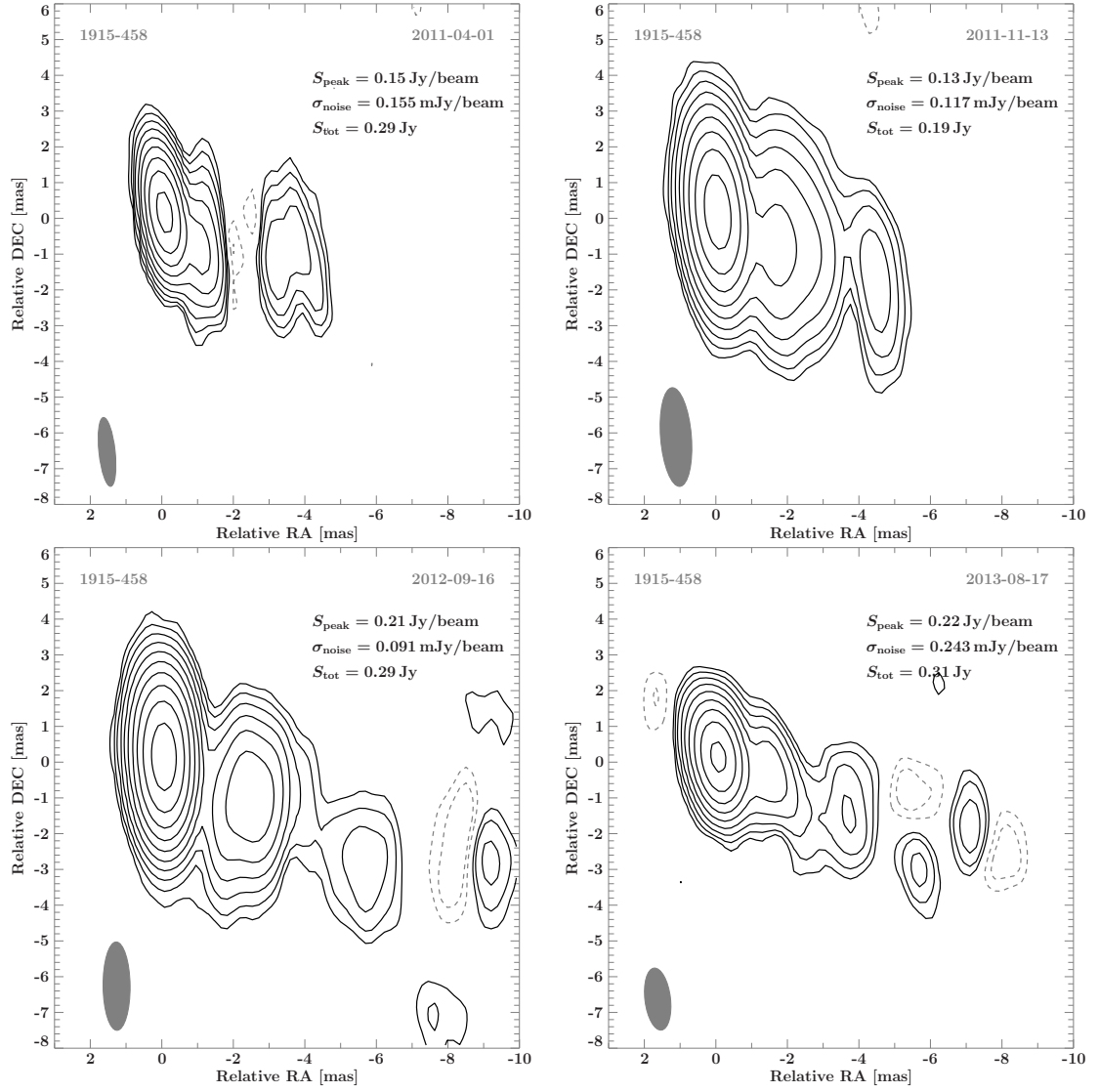


Figure A.4.: Clean maps of PKS 1915–458.

A.4. Individual Images of PKS 2106–413

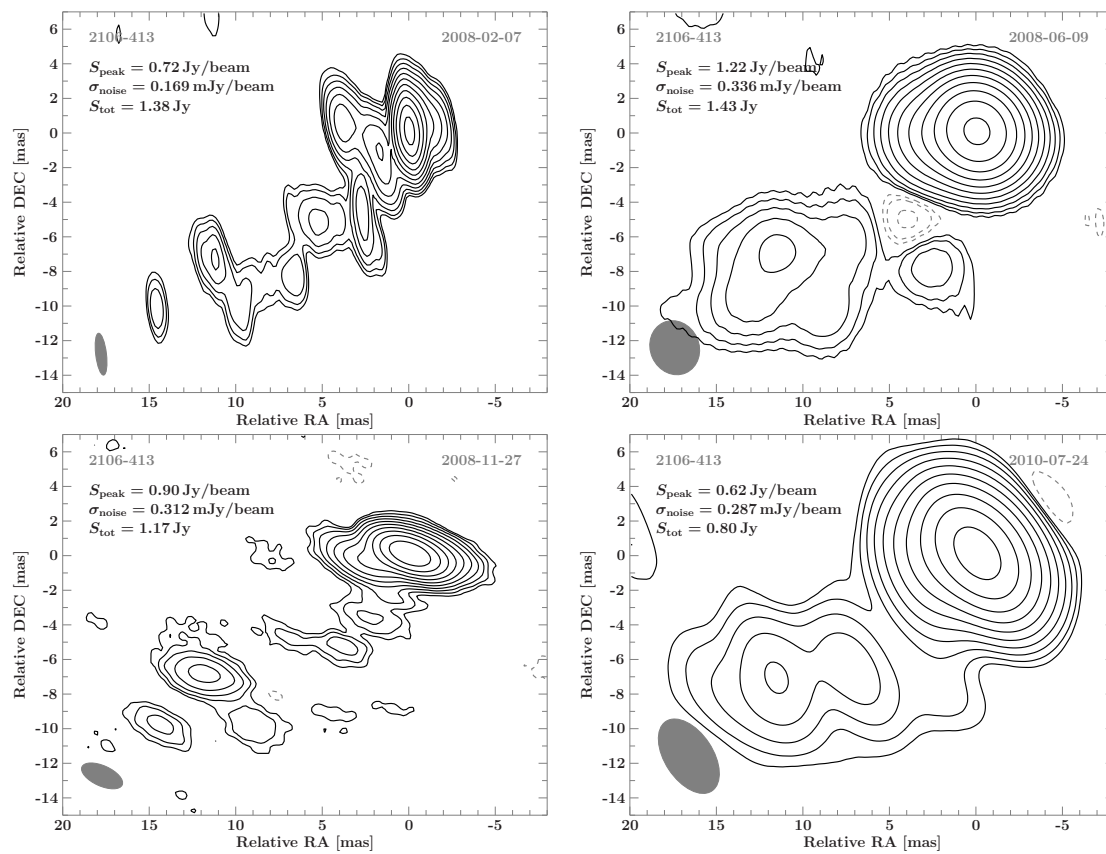
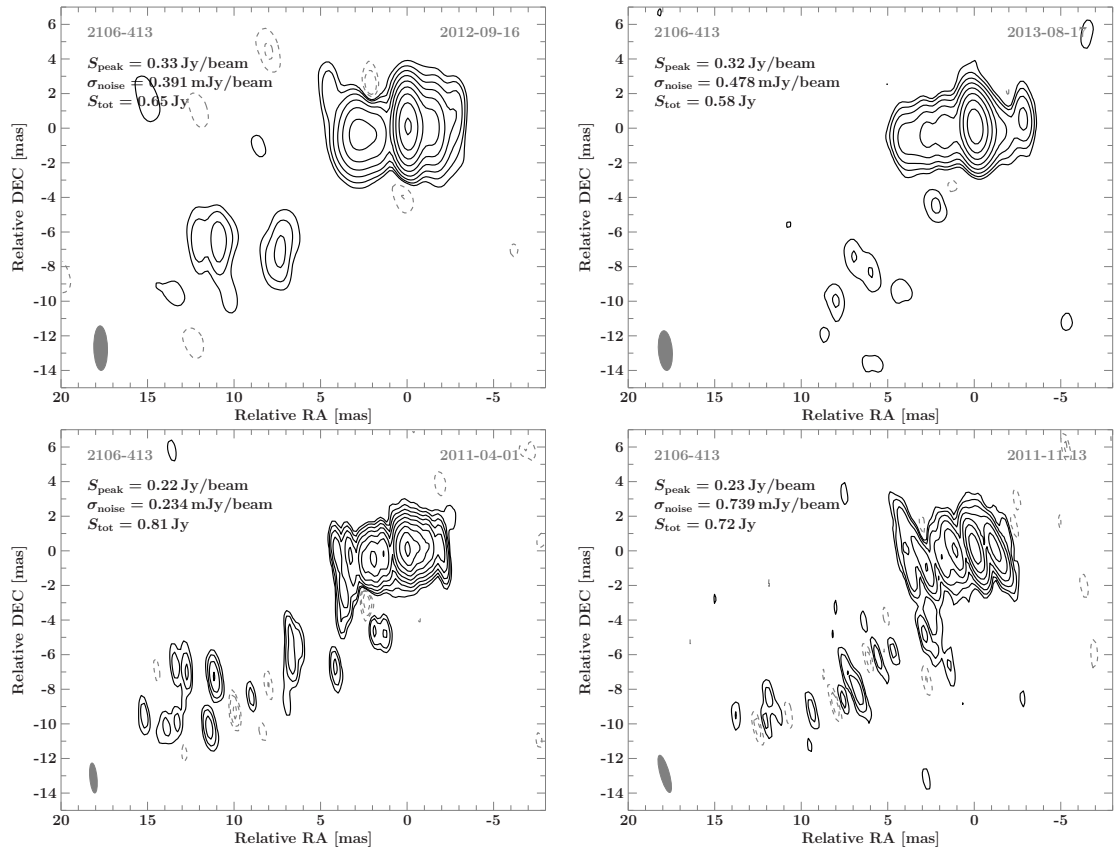


Figure A.5.: Clean maps of PKS 2106–413 (continued on next page).

A. Individual Images of all sources



(Continued from previous page) Clean maps of PKS 2106–413.

Bibliography

- Abdo, A. A., Ackermann, M., Ajello, M., et al., 2011, ApJ 733, L26
- Ackermann, M., Ajello, M., Allafort, A., et al., 2011, ApJ 743, 171
- Ackermann, M., Ajello, M., Atwood, W., et al., 2015, ApJ 810, 14
- Aharonian, F., Akhperjanian A. G., Bazer-Bachi, A. R., et al., 2006, Nature 440, 1018A
- Antonucci, R., 1993, ARA&A, 31, 473
- Bass, M., Stryland, E. W. V., Williams, D. R., Wolfe W. L., 1995, Handbook of Optics Volume II Devices, Measurements, and Properties 2nd Edition, NY: McGraw-Hill
- Beckmann, V., Shrader, C., Active Galactic Nuclei, 2012, Weinheim: Wiley
- Berstein, R. A., In: Encyclopedia of Astronomy & Astrophysics 2006, Bristol: IOP Publishing Ltd.
- Bevington, P. R., Robinson, D. K., 2003, Data Reduction and Error Analysis for the Physical Sciences (3rd ed.), New York: McGraw Hill
- Bignall, H. E., Jauncey, D. L., Lovell, J. E. J., et al., 2003, ApJ 585, 653
- Bignall, H. E., Macquart, J., Jauncey, D. L., et al., 2006, ApJ 652, 1050
- Blanchard, J. M., Lovell, J. E. J., Ojha, R., et al., 2012, A&A 538, A150
- Blandford, R. D., Königl, A., 1979, ApJ 232, 34
- Blandford, R. D., Znajek, R. L., 1977, MNRAS 179, 433
- Blumenthal, G. R., Gould, R. J., 1970, Rev. Mod. Phys. 42, 237
- Böck, M., Kadler, M., Müller, C., et al., 2016, A&A 590, A40
- Böttcher, M., 2010, In: Savolainen, T., Ros, E., Porcas, R. W., Zensus, J. A. (eds.), Fermi meets Jansky - AGN in Radio and Gamma-Rays, Bonn
- Böttcher, M., Harris, D. E., Krawczynski, H., 2012, Relativistic Jets from Active Galactic Nuclei, Weinheim: Wiley

- Böttcher, M., Reimer, A., Marscher, A. P., 2009, *ApJ* 703, 1168
- Burke, B., Graham-Smith, F., 2010, *An Introduction to Radio Astronomy*, Cambridge: Cambridge University Press
- Buson, S., 2013, PhD Thesis, Dipartimento di Fisica ed Astronomia, Università degli Studi di Padova
- Cheung, C., 2016, *ATel*, 9854
- Chodorowski, M. J., 2005, *Am. J. Phys.* 73, 639
- Cornwell, T. J., 1989, *Science* 245, 263
- Cornwell, T., Braun, R., Briggs, D.S., 1999, In: Taylor, G.B., Carilli, C.L., Perley, R. A. (eds.), *Synthesis Imaging in Radio Astronomy II*, ASP Conference Series 180, 151
- Cornwell, T., Fomalont, E. B., 1999, In: Taylor, G. B., Carilli, C. L., Perley, R. A. (eds.), *Synthesis Imaging in Radio Astronomy II*, ASP Conference Series 180, 187
- Costamante, L., Cutini, S., Tosti, G., Antolini, E., Tramacere, A., 2018, *MNRAS* 477, 4749
- Cotton, W. D., 1995, In: Zensus, J. A., Diamond, P. J., Napier, P. J. (eds.), *Very Long Baseline Interferometry and the VLBA*, ASP Conference Series 82, 189
- Curtis, H. D., 1918, *Publ. Lick Obs.* 13, 9
- Diamond, P. J., 1995, In: Zensus, J. A., Diamond, P. J., Napier, P. J. (eds.), *Very Long Baseline Interferometry and the VLBA*, ASP Conference Series 82, 227
- Edwards, P. G., Phillips, C., 2015, *Publications of the Korean Astronomical Society* 30, 659
- Fazio, G. G., Stecker, F. W., 1970, *Nature* 226, 135
- Finke, J. D., Razzaque, S., Dermer, C. D., 2010, *ApJ* 712, 238
- Fomalont, E. B., Frey, S., Paragi, Z., et al., 2000, *ApJ Supplement Series* 131, 95
- Fossati, G., Maraschi, L., Celotti, A., Comastri, A., Ghisellini, G., 1998, *MNRAS* 299, 433
- Franceschini, A., Rodighiero, G., Vaccari, M., 2008, *A&A* 487, 837
- Ghisellini, G., 2016, In: Gomez, J.L., Marscher, A. P., Jorstad, S. G. (eds.), *Blazars through sharp multi-wavelength eyes, Galaxies*, in press, arXiv:1609.08606

- Ghisellini G., Celotti A., Fossati G., Maraschi, L., Comastri, A., 1998, MNRAS 301, 451
- Ghisellini G., Tavecchio F., 2009, MNRAS 397, 985
- Ghisellini, G., Tavecchio, F., Foschini, L., et al., 2010, MNRAS 402, 497
- Ghisellini, G., Tavecchio, F., Foschini, L., Ghirlanda, G., 2011, MNRAS 414, 2674
- Graham, P. J., Tingay, S. J., 2014, ApJ 784, 159
- Greisen, E. W., 2003, In: Heck A. (ed.), *Information Handling in Astronomy - Historical Vistas*, Astrophysics and Space Science Library 285, Dordrecht: Springer
- Hada, K., Doi, A., Kino, M., et al., 2011, Nature 477, 185
- Högbom, J. A., A&AS 15, 417
- Houck, J. C., DeNicola, L. A., 2000, In: Manset, N., Veillet, C., Crabtree, D. (eds.), *Astronomical Data Analysis Software and Systems IX*, ASP Conference Series 216, 591
- Impey, C. D., Tapia, S., 1990, ApJ 354, 124
- Jackson, C. A., Wall, J. V., Shaver, P. A., et al., 2002, A&A 386, 97
- Jennison, R. C., 1958, MNRAS 118, 276
- Jorstad, S. G., Marscher, A. P., Lister, M. L., et al., 2005, AJ 130, 1418
- Kadler, M., Ojha, R., & TANAMI Collaboration, 2015, AN 336, 499
- Kellermann, K. I., Lister, M. L., Homan, D. C., et al., 2004, ApJ 609, 539
- Kellermann, K. I., Pauliny-Toth, I. I. K., 1968, ARA&A 6, 417
- Kellermann, K. I., Pauliny-Toth, I. I. K., 1969, ApJ 155, L71
- Kellermann, K. I., Sramek, R., Schmidt, M., Shaffer, D. B., Green, R., 1989, AJ 98, 1195
- Khachikian, E. Y., Weedman, D. W., 1974, ApJ 192, 581
- Kovalev, Y. Y., Kellermann, K. I., Lister, M. L., et al., 2005, AJ 130, 2473
- Krolik, J. H., 1999, *Active Galactic Nuclei, From the Central Black Hole to the Galactic Environment*, Princeton: Princeton University Press
- Lawrence, A., 1987, PASP 99, 309
- Lister, M. L., Homan, D. C., Kadler, M., et al., 2009, ApJ 696, L22

- Lister, M. L., Aller, M. F., Aller, H. D., et al., 2015, *ApJ* 810, L9
- Liu, H. T., Bai, J. M., 2006, *ApJ* 653, 1089
- Liu, H. T., Bai, J. M., Ma, L., 2008, *ApJ* 688, 148
- Mannheim, K., 1993, *A&A* 269, 67
- Marscher, A. P., 2005, *Mem. Soc. Astron. Italiana* 76, 168
- Marscher, A. P., 2009, In: Belloni, T. (ed.), *The Jet Paradigm - From Microquasars to Quasars*, *Lect. Notes Phys.* 794, in press, arXiv:0909.2576
- Morton, D. C., Savage, A., Bolton, J. G., 1978, *MNRAS* 185, 735
- Mücke, A., Protheroe, R. J., 2000, *AIP Conference Proceedings* 515, 149
- Mücke, A., Protheroe, R. J., 2001, *Astropart. Phys.* 15, 121
- Mücke, A., Protheroe, R. J., Engel, R., Rachen, J. P., Stanev, T., 2003, *Astropart. Phys.* 18, 593
- Müller C., 2014, PhD Thesis, Institut für Physik und Astronomie, Julius-Maximilians-Universität Würzburg
- Müller, C., Kadler, M., Ojha, R., et al., 2018, *A&A* 610, A1
- Nolan, P. L., Abdo, A. A., Ackermann, M., et al., 2012, *ApJ Supplement Series* 199, 31
- Ojha, R., Kadler, M., Böck, M., et al., 2010, *A&A* 519, 45
- Pearson, T. J., 1995, In: Zensus, J. A., Diamond, P. J., Napier P. J. (eds.), *Very Long Baseline Interferometry and the VLBA*, *ASP Conference Series* 82, 267
- Perlman, E. S., Padovani, P., Giommi, P., et al., 1998, *AJ* 115, 1253
- Peterson, B. M., 1997, *An Introduction to Active Galactic Nuclei*, Cambridge: Cambridge University Press
- Pian, E., Falomo, R., Treves, A., 2005, *MNRAS* 361, 919
- Punsly, B., 1995, *AJ* 109, 1555
- Punsly, B., Tramacere, A., Kharb, P., Marziani, P., 2018, *ApJ* 869, 174
- Readhead, A. C. S., 1994, *ApJ* 425, 51
- Readhead, A. C. S., Walker, R. C., Pearson, T. J., Cohen, M. H., 1980, *Nature* 285, 137

-
- Readhead, A. C. S., Wilkinson, P. N., 1978, *ApJ* 223, 25
- Rösch, F., 2016, Bachelor's Thesis, Institut für Physik und Astronomie, Julius-Maximilians-Universität Würzburg
- Rybicki, G. B., Lightman, A. P., 1979, *Radiative Processes in Astrophysics*, New York: Wiley
- Ryle, M., Neville, A. C., 1962, *MNRAS* 125, 39
- Schneider, P., 2015, *Extragalactic Astronomy and Cosmology, an Introduction*, Heidelberg: Springer
- Seyfert, C. K., 1943, *ApJ* 97, 28
- Shakura, N. I., Sunyaev, R. A., 1973, *A&A* 24, 337
- Shepherd, M. C., In: Hunt, G., and Payne, H. E. (eds.), *Astronomical Data Analysis Software and Systems VI*, ASP Conference Series 125, 77
- Siebert, J., Brinkmann, W., Drinkwater, M. J., et al., 1998, *MNRAS* 301, 261
- Sokolovsky, K. V., Kovalev, Y. Y., Pushkarev, A. B., Lobanov, A. P., 2011, *A&A* 532, A38
- Sokolovsky, K. V., Schinzel, F. K., Healey, S. E., et al., 2010, *ATel*, 2666
- Sokolovsky, K. V., D'Ammando, F., Schinzel, F. K., 2010, *ATel*, 2679
- Stecker, F. W., Baring, M. G., Summerlin, E. J., 2008, *ApJ* 667, L29
- Taylor, G., 1997, *The DIFMAP Cookbook*
- Taylor, G. B., Carilli, C. L., Perley, R. A. (eds.), 1999, *Synthesis Imaging in Radio Astronomy II*, ASP Conference Series 180
- Tingay, S. J., Murphy, D. W., Edwards, P. G., 1998, *ApJ* 500, 673
- Thompson, A. R., Moran, J. M., Swenson, G. W., 2004, *Interferometry and Synthesis in Radio Astronomy*, Weinheim: Wiley
- Trüstedt, J., 2013, Master's Thesis, Institut für Physik und Astronomie, Julius-Maximilians-Universität Würzburg
- Ulrich, M. H., Maraschi M., Urry, C. M., 1997, *ARA&A* 35, 445
- Urry, C. M., Padovani, P., 1995, *PASP* 107, 803

- Véron-Cetty, M.-P., Véron, P., 2010, A&A 518, A10
- von Montigny, C., Bertsch, D. L., Chiang, J., et al., 1995, A&A 299, 680
- Walker, M. A., Tuntsov, A. V., Bignall, H., et al., 2017, ApJ 843, 15
- Ward, M., Elvis, M., Fabbiano, G., et al., 1987, ApJ 315, 74
- Wilkes, B. J., Elvis, M., Fiore, F., et al., 1992, ApJ 393, L1
- White, G. L., Jauncey, D. L., Savage, A., et al., 1988, ApJ 327, 561
- Woods, P., 2017, Nature Astronomy 1, 0201

List of Figures

2.1. Spectral behaviour of a QSO.	6
2.2. Redshift distribution of blazars.	8
2.3. Illustration of the AGN unification model.	9
2.4. Jet structure of a radio-loud AGN.	12
2.5. Flux ratio of a jet to the counterjet.	13
2.6. Superluminal motion of jet components.	15
2.7. Apparent velocity β_{app} for different jet speeds as a function of θ	16
2.8. Average SEDs for a blazar sample.	17
2.9. Distributions of observed synchrotron peak frequency of blazars.	18
2.10. Helical motion of a particle in a uniform magnetic field.	19
2.11. Emission cones of a particle along its trajectory.	20
2.12. Synchrotron spectrum of single electrons.	21
2.13. Broken power law spectrum for synchrotron radiation.	22
2.14. Sketch of the radio coreshift of an jet	23
2.15. γ - γ opacity due to photons from the BLR	27
2.16. $\tau_{\gamma\gamma} = 1$ for several models of the EBL as a function of redshift.	28
2.17. Electromagnetic spectrum showing wavelength "windows".	29
2.18. Sketch of a two-element interferometer.	30
2.19. Sketch of a two-element interferometer and the u, v - and x, y -planes.	31
2.20. A loop of three radio antennae.	34
2.21. A typical algorithm for self-calibration.	36
2.22. Coverage of the u, v -plane by the MERLIN interferometer.	37
3.1. TANAMI telescope array.	39
4.1. Time evolution of PKS 0438–436.	47
4.2. T_{B} of the components of PKS 0438–436 as a function of time.	50
4.3. Flux densities of the components of PKS 0438–436 as a function of time.	50
4.4. Distance of the components of PKS 0438–436 as a function of time.	51
4.5. Time evolution of PKS 1257–326.	54
4.6. T_{B} of components of PKS 1257–326 as a function of time.	56
4.7. Flux densities of components of PKS 1257–326 as a function of time.	56
4.8. Distance of the components of PKS 1257–326 as a function of time.	57
4.9. Time evolution of PKS 1915–458.	60
4.10. T_{B} of the components of PKS 1915–458 as a function of time.	62

4.11. Flux densities of the components of PKS 1915–458 as a function of time.	62
4.12. Distance of components of PKS 1915–458 as a function of time.	63
4.13. Time evolution of PKS 2106–413.	65
4.14. T_B of the components of PKS 2106–413 as a function of time.	69
4.15. Flux densities of the components of PKS 2106–413 as a function of time.	69
4.16. Distance of the jet components of PKS 2106–413 as a function of time. .	70
5.1. Redshift distribution of 3LAC sources.	73
5.2. Phenomenological blazar sequence for different γ -ray luminosities	74
5.3. Peak frequencies of SEDs of blazars as a function of γ -ray luminosity . . .	75
5.4. γ -ray energy flux against radio flux density at 1.4 GHz.	76
5.5. Spectral energy distribution for PKS 0438–436.	77
5.6. <i>Fermi</i> /LAT γ -ray light curve of PKS 0438–436.	78
5.7. Redshift distribution of LAT sources.	79
5.8. Light curves over the course of a year for PKS 1257–326.	80
5.9. <i>Fermi</i> /LAT γ -ray light curve of PKS 1257–326.	81
5.10. Distribution of angular velocity for various redshifts.	83
5.11. Maximum measured jet speed vs. synchrotron SED peak frequency.	84
5.12. <i>Fermi</i> /LAT γ -ray light curve of PKS 1915–458.	85
5.13. Clean map of PKS 2106–413.	86
5.14. <i>Fermi</i> /LAT γ -ray light curve of PKS 2106–413.	87
A.1. Clean maps of PKS 0438–436.	94
A.2. Clean maps of PKS 0438–436, restored.	96
A.3. Clean maps of PKS 1257–326.	98
A.4. Clean maps of PKS 1915–458.	100
A.5. Clean maps of PKS 2106–413.	101

List of Tables

2.1. Classification Characteristics of Active Galactic Nuclei	7
3.1. The TANAMI Array	40
4.1. Observation Epochs for PKS 0438–436	46
4.2. Model fit parameters for PKS 0438–436	48
4.3. Apparent speed of the components of PKS 0438–436.	52
4.4. Observation Epochs for PKS 1257–326	53
4.5. Model fit parameters for PKS 1257–326	55
4.6. Apparent speed of the components of PKS 1257–326.	57
4.7. Observation Epochs for PKS 1915–458	59
4.8. Model fit parameters for PKS 1915–458	61
4.9. Apparent speed of the components of PKS 1915–458.	63
4.10. Observation Epochs for PKS 2106–413	64
4.11. Model fit parameters for PKS 2106–413	66
4.12. Apparent speed of the components of PKS 2106–413.	70

Acknowledgements

I would like to take this opportunity to thank all of the people who have offered me their support along the road of completing my Master's Degree. First and foremost, I would like to thank Prof. Dr. Matthias Kadler, not only for his steady supervision of this thesis, but also for creating an intellectually engaging and challenging environment in the research group. I have felt welcomed and supported to discover and fulfil my potential since my first day in the *Lehrstuhl für Astronomie*. Thank you for your motivation, patience, and encouragement. I would also like to thank Prof. Dr. Karl Mannheim, chair of the *Lehrstuhl für Astronomie* in Würzburg for the opportunity to complete my Master's Degree in this department.

I would like to thank Dr. Roopesh Ojha for his meticulous calibration of the TANAMI data and for his help in deciphering the telescope abbreviations. I would also like to thank Prof. Dr. Joern Wilms, Professor of Astronomy at the Dr. Karl Remeis Sternwarte in Bamberg, for the opportunity to work for and spend time at the observatory, and Prof. Dr. Wolfgang Dröge for the opportunity to work as a teaching assistant in Würzburg. I thank Dr. Robert Schulz, Dr. Cornelia Müller and Dr. Christoph Großberger for teaching me how to analyse TANAMI data with DIFMAP.

I am grateful to those who contributed their time to proofreading this thesis. Dr. Thomas Dauser, thank you for your steadfast support throughout this thesis and beyond. Dr. Eva Ziegerer, thank you for your constructive feedback and encouragement. Dr. Michael Kreter, thank you for sharing not only an office with me, but also your good mood. Florian Rösch, thank you for the many insightful discussions and for your willingness to help. Marcus Langejahn, thank you for the moral support you have provided and for your willingness to help me find answers to my questions. Christian Tietz, thank you for your help deciphering scripts, and for the past few years spent living together. Michi Wittmann, thank you for proofreading my German grammar and punctuation.

Additionally, I would like to thank all of the members of the Department of Astrophysics in Würzburg and the Dr. Karl Remeis Sternwarte in Bamberg with whom I have worked in the past and present. It was truly a pleasure to travel this road with each and every one of you. Katharina Leiter, thank you for your open heart and sound advice, both academic and otherwise; you are a pillar of this community, without whom much would crumble. To Annika Kreikenbohm, Dr. Tobias Beuchert, Andrea Gokus, Paul Ray Burd, Alex Kappes, Jonas Ringholz and many more, thank you for the contributions you have made to my time here.

I am grateful for the friends who have made my time in Würzburg as wonderful as it has been and who have provided me with the balance I need.

To Alexander Rohr, thank you for challenging me and motivating me to work hard in every aspect of my life.

I would like to thank my family for their unconditional support and belief in me. To my parents, Hyun and Richard, and my sister, Arabella, I am so appreciative of the guidance and encouragement you provide.

This research has made use of the NASA/IPAC Extragalactic Database (NED) which is operated by the Jet Propulsion Laboratory, California Institute of Technology, under contract with the National Aeronautics and Space Administration.

This research has made use of ISIS functions provided by ECAP/Dr. Karl Remeis Observatory and MIT.

This research has made use of data from the TANAMI database which is maintained by the TANAMI Collaboration (Ojha et al. 2010).

This research has made use of the SAO/NASA Astrophysics Data System which is hosted by the High Energy Astrophysics Division at the Harvard-Smithsonian Center for Astrophysics.

Declaration of Authorship

I, Rosamunde Pare, declare that this thesis and the work presented in it are my own. I confirm that:

- This work was done wholly or mainly while in candidature for a research degree at this university.
- If any part of this thesis has been previously submitted for a degree or any other qualification at this university or any other institution, this has been stated clearly.
- Instances in which the published work of others have been clearly attributed.
- Quotes from the work of others are always cited accordingly. Excepting such quotes, this thesis is entirely my own work.
- I have acknowledged all main sources of help.

Würzburg, 27 March 2019

Rosamunde Pare